Electronic Structure Method Development for Excited-State Chemistry

A THESIS

SUBMITTED TO THE FACULTY OF THE

GRADUATE SCHOOL

OF THE UNIVERSITY OF MINNESOTA

Chad Edward Hoyer

IN PARTIAL FULFILLMENT OF THE REQUIREMENTS

FOR THE DEGREE OF

DOCTOR OF PHILOSOPHY

Advisors: Laura Gagliardi and Donald G. Truhlar

September 2017

Acknowledgments

I would like to first acknowledge my advisers for their guidance and support. I would also like to acknowledge Dr. Dongxia Ma and Prof. Jeppe Olsen for productive collaborations and theoretical discussions. Numerous others have had constructive effects on my research: Dr. Rebecca K. Carlson, Dr. Andrew M. Sand, Dr. Remi Maurice, Dr. Yinan Shu, Dr. Xuefei Xu, Dr. Zoltan Varga, Kelsey Parker, and Dr. Shaohong L Li. Special thanks to the Newman and Lillian Bortnick Fellowship in Chemistry, Doctoral Dissertation Fellowship for funding, National Science Foundation, and Department of Energy for funding. Finally, I would like acknowledge Minnesota Supercomputing Institute for computing resources.

Dedication

I would like to first thank the two women who are such an important part of my life, Amanda and the momma. I would like to thank the many who have provided strong social support for the past few years and reminded me that I am more than a science robot: Jess, John, Chad, Brady, Maddison, Dan, Becky, Rob, Josh, Ben, and Katie. Finally, I would like to give a special dedication to the album "No Shouts, No Calls" by Electrelane for accompanying me on many a late night.

Abstract

The accurate modeling of photochemistry requires robust dynamics simulations on correct potential surfaces. A pragmatic approach is to first compute potential surfaces with an accurate electronic structure method, fit the surfaces to an analytic function, and then run dynamics using the fitted surfaces. This approach will be referred to as fitted dynamics. The focus of this work is on the electronic structure aspect of fitted dynamics. Specifically, I will discuss my work on benchmarking and method development of multiconfiguration pair-density functional theory (MC-PDFT) and diabatization method development.

MC-PDFT is very similar to Kohn-Sham Density Functional Theory (KS-DFT); however, MC-PDFT uses a multiconfigurational (MC) wave function (WF) instead of a single Slater determinant (SD), the MC-PDFT energy is a functional of the density and on-top pair density instead of only the density, and the MC-PDFT energy is computed via post-SCF instead of optimizing the molecular orbitals (MOs). Due to the MC nature of excited states, MC-PDFT is a promising alternative to KS-DFT for photochemistry. To check if MC-PDFT is useful for photochemistry, we first benchmarked it on vertical excitation energies of atoms and organic molecules. We found that MC-PDFT exhibits quantitative accuracy. We have also explored new theory developments, which may be of use for practical photochemistry applications.

With regards to diabatization, the dipole-quadrupole (DQ) and dipole-quadrupole-electrostatic-potential (DQΦ) diabatization schemes were developed. They diabatize using simple one-electron properties and the methods exhibit applicability to general systems.

Contents

List of Figures

List of Tables

Introduction

Excited states play a crucial role in a variety of applications, from photochemistry [1] to biological processes [2]. However, current tools for modeling excited-state chemistry are often inadequate; one quickly encounters the dilemma of choosing an accurate method with unfavorable scaling (to the point that a calculation is unfeasible) or a less expensive method with unreliable accuracy.

Photochemistry is a crucial field of study due to its wide applicability. From optics to the harnessing of solar energy, the interaction of light with molecules plays an important role. Despite its importance, mechanistic insight is still difficult to gain via computations. To understand why, let us consider a model photochemical process (see Figure 1). Electromagnetic radiation interacts with the ground-state reactant, resulting in an electronic excitation (red arrow). Relaxation can then occur via various pathways to the reactant or product. To model such a complicated process, one could use an electronic structure method that computes accurate potential energy surfaces (PESs) for ground and excited states. Then, one could run dynamical simulations using the accurate PESs. However, current tools to accomplish both steps are either not accurate enough or are computationally unfeasible for broad applicability.

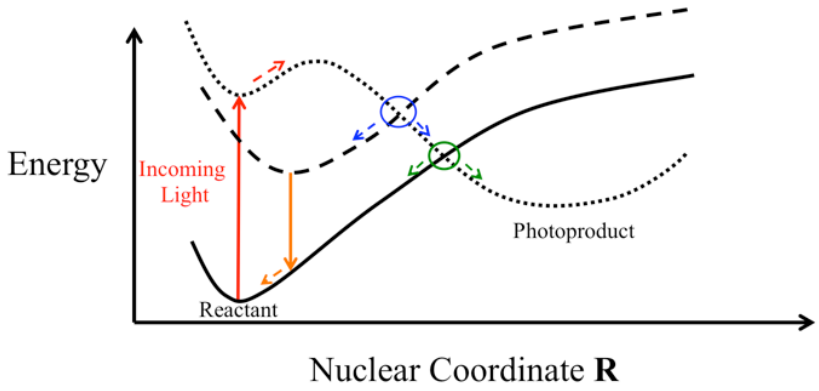

Figure 1: Simplified schematic of several of the possible paths of a photochemical reaction. The three black lines are potential energy curves, solid arrows correspond to electronic phenomena, circles are regions where two electronic states are strongly coupled, and dashed lines imply a nuclear motion in that direction.

Cheap and accurate computations of excitation energies are not trivial and developing new electronic structure methods is ongoing in the field (for a review of electronic structure methods, see Section 1.1). Kohn-Sham density functional theory (KS-DFT) has become one of the most useful electronic structure methods due to a good balance between cost and accuracy [3] In KS-DFT, one computes the electronic energy as a functional of the electron density, and the electron density is computed by considering a single electronic configuration (see Section 1.1.6 for more information). However, there are many systems where a single electronic configuration is a poor approximation (e.g., resonance structures, excited states, etc.), which can result in poor accuracy for standard functionals. A promising new electronic structure method was recently developed known as as multiconfiguration pair-density functional theory (MC-PDFT) [4]. In MC-PDFT, one uses multiple configurations to compute the energy as a functional of the electron density and on-top pair density (the probability of finding two electrons at the same point in space). The multiconfigurational treatment of systems (the use of multiple electronic configurations) is the key differentiating trait of MC-PDFT. Among similar energy functionals, a decrease in mean unsigned error for ground state properties was observed compared to KS-DFT [5]. To test if MC-PDFT could be useful for photochemistry, vertical excitation energies were benchmarked in Section 2. In addition, development of MC-PDFT methods that may be useful for excited-state chemistry is covered in Section 3.

Let us assume we have an electronic structure method that is accurate and computationally feasible for general ground- and excited-state potential surfaces. Rather than computing electronic structure energies on-the-fly during a dynamics simulation, let us also focus on fitted dynamics, where the potential surfaces are computed and fitted before the dynamics simulation, and the analytical function is used during the simulation. A non-trivial problem is the fitting of potential surfaces. The choice of representation is important. The set of wave functions that diagonalize the Born-

Oppenheimer Hamiltonian (Equation 3) are adiabatic. Adiabatic states are coupled through the nuclear momentum. Analytical representations of potential energy surfaces and couplings in the adiabatic representation are unfeasible in general due to the discontinuous first derivatives. This motivates transforming to another representation. One might hope to transform to a representation with smooth surfaces and zero nuclear-momentum couplings. However, this representation does not exist in general [6]. However, representations with smooth surfaces and negligible momentum couplings can be found, and we will refer to such a representation as diabatic [7]. Diabatic states do not diagonalize the electronic Hamiltonian, so the off-diagonal elements are non-zero. Many diabatization methods exist; however, they are often not general. A general feature of diabatic states though is that they should be smooth functions of nuclear coordinates since they are negligible if the state functions are smooth and slowly varying. In Sections 4 and 5, new diabatization methods were developed that make use of the dipole, quadrupole, and/or electrostatic potential.

1 Electronic Structure Review

In Section 1.1 some of the basic quantum mechanical theories and methods are covered.

1.1 Quantum Chemistry Background

In Section 1.1.1 a basic overview of elementary quantum mechanics will be given. In Section 1.1.2 many of the fundamental concepts for solving the electronic problem in quantum mechanics will be introduced. In Sections 1.1.3 and 1.1.4, the restricted closed-shell Hartree-Fock and Møller-Plesset perturbation theory truncated to second order methods will be respectively discussed. In Section 1.1.5 multiconfigurational wave function-based theories are covered. Finally, in Section 1.1.6 Kohn-Sham density functional theory will be introduced.

1.1.1 Quantum Mechanics

There are two important postulates in quantum mechanics. 1) All information for a system is contained in the wave function (WF) for that system. 2) For any physical property, there is a corresponding operator. An equation very important to quantum chemistry is the time-independent Schrödinger Equation

$$\hat{H}|\Psi\rangle = E|\Psi\rangle \tag{1}$$

where $|\Psi\rangle$ is a WF, $\hat{H}$ is the Hamiltonian operator, and E is the energy for the system [8].

The nonrelativistic form of the Hamiltonian for many electron molecular systems in first quantization in atomic units is

$$\hat{H}_{\mathrm{eN}} = -\sum_i \frac{1}{2}\nabla_i^2 - \sum_A \frac{1}{2m_A}\nabla_A^2 - \sum_{i,A} \frac{Z_A}{r_{iA}} + \sum_{i<j} \frac{1}{r_{ij}} + \sum_{A<B} \frac{Z_A Z_B}{r_{AB}} \tag{2}$$

where m_A is the mass of nucleus A, ∇^2 is the Laplacian operator, Z_A is the magnitude of the charge of nucleus A, indices i and j run over electrons, indices A and B run over nuclei, and r_{iA} is the distance between particles i and A [9]. The first two terms are the kinetic energy of electrons and nuclei, respectively. The third term is the potential energy of the nuclear-electron attraction, the fourth term the electron-electron repulsion, and the fifth term is the nuclear-nuclear repulsion [9].

The Born-Oppenheimer (BO) approximation is commonly invoked to decouple the motion of the nuclei and electrons. Under this approximation the nuclei are considered stationary compared to the motion of electrons, which changes the Hamiltonian in Equation (2) since the second term is now zero because stationary nuclei have zero kinetic energy, and the fifth term is now a constant, resulting in

$$\hat{H} = \underbrace{-\sum_i \frac{1}{2}\nabla_i^2 - \sum_{i,A} \frac{Z_A}{r_{iA}}}_{\hat{h}} + \underbrace{\sum_{i<j} \frac{1}{r_{ij}}}_{\hat{g}} + h_{\text{nuc}} \tag{3}$$

where $\hat{H}$ is the Hamiltonian for an N-electron system after applying the BO approximation, h_{nuc} is the constant nuclear-nuclear repulsion, $\hat{h}$ is the 1-electron part of $\hat{H}$, and $\hat{g}$ is the 2-electron part of $\hat{H}$ [9]. We will refer to the sum of the $\hat{h}$ and $\hat{g}$ terms in Equation (3) as the electronic Hamiltonian.

1.1.2 Foundation for Approximating Wave Functions of Molecular Systems

It is difficult to determine an eigenfunction of the electronic Hamiltonian for systems of more than one electron due to the two-electron part $\hat{g}$. Because of this, a convenient choice is to describe an N-electron WF in a basis of one-electron WFs referred to as molecular orbitals (MOs). This one-electron formalism will be used in all methods discussed.

As already described, determining an eigenfunction of the electronic Hamiltonian

$(\hat{h}+\hat{g})$ in Equation 3 is very difficult. Now for an N-electron system, an eigenfunction of just the one-electron part $(\hat{h})$ is a product of MOs (a Hartree product). However, this is not a sufficient N-electron WF. To satisfy the Pauli exclusion property, the WF must be antisymmetric upon exchange of any two electrons, which is not a property of Hartree products. One way to enforce this is to take an antisymmetrized linear combination of Hartree products. This is referred to as a Slater determinant (SD) and is represented by

$$|\Phi\rangle = \frac{1}{\sqrt{N!}} \begin{vmatrix} \phi_1(\mathbf{x}_1) & \phi_1(\mathbf{x}_2) & \cdots & \phi_1(\mathbf{x}_N) \\ \phi_2(\mathbf{x}_1) & \phi_2(\mathbf{x}_2) & \cdots & \phi_2(\mathbf{x}_N) \\ \vdots & \vdots & \ddots & \vdots \\ \phi_N(\mathbf{x}_1) & \phi_N(\mathbf{x}_2) & \cdots & \phi_N(\mathbf{x}_N) \end{vmatrix} \tag{4}$$

where the prefactor is a normalization constant that is dependent on the number of electrons (N), ϕ are real orthonormal spin MOs, and $\mathbf{x}_i$ is the spatial and spin coordinate of the electron i [9]. Why the determinant structure of Equation (4) is satisfactory is illustrated by the exchange of electrons 1 and 2. This is the equivalent of switching the first and second column, which introduces a prefactor of -1 due to the properties of determinants. Thus, the N-electron WF in Equation (4) satisfies the Pauli exclusion principle [9].

In a restricted formalism, the spatial part of the α and β spin functions of an MO are not allowed to differ; whereas, they are allowed to differ in an unrestricted formalism. A closed-shell determinant refers to a SD with all spatial orbitals doubly occupied. Similarly, a SD with at least one MO singly occupied is an open-shell determinant [9].

The SD is a sufficient form for an N-electron WF that is an eigenfunction of the 1-electron part of the electronic Hamiltonian. This is not a sufficient approximation for the WF that is the eigenfunction of the full electronic Hamiltonian since the two-

electron part in N-electron systems is not negligible. To arrive at the exact solution to the electronic Hamiltonian in WF theory, the WF is expanded in a complete basis of SDs

$$|\Psi\rangle = \sum_i C_i |\Phi_i\rangle \tag{5}$$

where the C are configuration interaction (CI) coefficients for the N-electron WF Ψ and the index i runs over SDs $|\Phi\rangle$ [10]. It is assumed that all WFs discussed are normalized.

In this work, we will expand MOs in a basis of atomic orbitals (AOs)

$$\phi_i = \sum_\mu \kappa_\mu \chi_\mu \tag{6}$$

where the κ_μ are MO coefficients for the MO i, $\chi_\mu$are AO basis functions, and the index μ runs over AO basis functions [10].

These definitions provide two well-defined metrics for specifying a given level of theory within a WF theory formalism that uses an MO basis: 1) the truncation of the sum in Equation (5) (the N-electron model) and 2) the truncation of the sum in Equation (6) (the basis set). Metric 1 will be the topic of discussion in this work. The N-electron model that makes no truncation in the number of configurations in Equation (5) is referred to as full CI (FCI). If there is no truncation in MO space of Equation (6), then it is referred to as a complete basis set [10].

1.1.3 Restricted Hartree-Fock Method

Let us now discuss a fundamental N-electron model, the restricted closed-shell Hartree-Fock (HF) method. In the HF method, the WF is modeled as a single SD (only one term in the summation in Equation (5)) with each spin orbital doubly occupied. Thus, the form of the HF WF is a SD, which is defined in Equation (4) in Section 1.1.2. The HF WF is an eigenfunction of

$$\hat{F} = \sum_n \hat{f}(n) = \sum_n \hat{h}(n) + \underbrace{\sum_i 2\hat{J}_i(n) - \hat{K}_i(n)}_{\hat{V}_{\mathrm{HF}}(n)} \tag{7}$$

where $\hat{V}_{\mathrm{HF}}$ is the HF potential, n is an electron index, i is an index over occupied MOs, $\hat{J}$ is the Coulomb operator, 2 is due to the restricted formalism, and $\hat{K}$ is the exchange operator. The Coulomb and exchange operators are

$$\hat{J}_i(1)\phi_i(1) = \left[\int \mathrm{d}\mathbf{x}_2 |\phi_j(2)|^2 r_{12}^{-1}\right]\phi_i(1) \tag{8}$$

$$\hat{K}_i(1)\phi_i(1) = \left[\int \mathrm{d}\mathbf{x}_2 \phi_j(2)^* \phi_i(2) r_{12}^{-1}\right]\phi_j(1) \tag{9}$$

where $j \neq i$ and r_{12} is the distance between electrons 1 and 2 [9]. The Fock operator is similar to the electronic Hamiltonian in Equation (3) of Section 1.1.2, except it is a sum of one-electron operators where the two-electron part, $\hat{g}$, is approximated by the Hartree-Fock potential. The HF WF corresponding to the N-electron system of interest is computed by variationally optimizing the MO coefficients of a SD to minimize

$$E_{\mathrm{HF}} = \langle \Phi_0 | \hat{H} | \Phi_0 \rangle \tag{10}$$

where E_{HF} is the electronic energy for the HF method and $|\Phi_0\rangle$ is a single SD [9]. In practice the Fock operator and SD are built from a trial set MO coefficients. The MO coefficients are optimized until self-consistent. The energy for the HF method is then computed as in Equation 10 [10].

The restricted HF method discussed in Section 1.1.3 is not accurate enough for relative electronic energies [10], which are important for many chemical phenomena. To further improve the accuracy, electron correlation needs to be included

$$E_{\mathrm{corr}} = E_{\mathrm{FCI}} - E_{\mathrm{HF}} \tag{11}$$

where E_{corr} is the correlation energy, E_{FCI} is the energy of a FCI calculation, and E_{HF}

is defined in Equation (10) of Section 1.1.3 [9].

1.1.4 Møller-Plesset Perturbation Theory at Second Order

One way to recover electron correlation with respect to the HF WF is perturbation theory. In perturbation theory one separates a challenging problem into an exactly-solvable part (H_0) and a perturbation (V), with the assumption that the perturbation is small. The specific perturbation theory method to be discussed in this section is Møller-Plesset perturbation theory truncated to second order (MP2). With respect to the Hamiltonian operator in Equation (3) in Section 1.1.1, the partitioning of the electronic problem for Møller-Plesset perturbation theory is

$$\hat{H} = \hat{h} + \left[\hat{H} - \hat{F}\right] = \hat{H}_0 + \hat{V} \tag{12}$$

where $\hat{h}$ is defined in Equation (3) of Section 1.1.1, and the difference in brackets is the perturbation $\hat{V}$ [11].

Let us examine the resulting energy for the MP2 method E_{MP2}

$$E_{\text{MP2}} = \left[\langle\Phi_0|\hat{H}_0|\Phi_0\rangle + \langle\Phi_0|\hat{V}|\Phi_0\rangle\right] + \sum_{j>0} \frac{\left|\langle\Phi_j|\hat{V}|\Phi_0\rangle\right|^2}{\langle\Phi_0|\hat{H}_0|\Phi_0\rangle - \langle\Phi_j|\hat{H}_0|\Phi_j\rangle} = E_{\text{HF}} + E_{\text{MP2corr}} \tag{13}$$

where E_{HF} is defined in Equation (10), E_{MP2corr} is the correlation energy recovered in the MP2 method, $|\Phi_0\rangle$ is the HF WF, and $|\Phi_j\rangle$ is a SD that is formed from a single or double excitation to unoccupied MOs out of the HF WF. This method is a practical way of recovering electron correlation in WF theory, but the method still may not model the system because it may not be qualitatively described by the reference HF WF [11].

1.1.5 Multiconfigurational Methods

One way to remedy the insufficiencies of using a single determinant in wave function (WF) theory is to model the WF for the system of interest as a linear combination of SDs. A WF of this form is referred to as multiconfigurational (MC). Directly analogous to HF discussed in Section 1.1.3 for a MC WF is multiconfigurational self-consistent field (MCSCF) theory. In MCSCF the MO coefficients, as in HF, and the CI coefficients are simultaneously variationally optimized to lower the electronic energy

$$E_{\mathrm{MC}} = \langle \Psi_0 | \hat{H} | \Psi_0 \rangle \tag{14}$$

where E_{MC} is MCSCF electronic energy and Ψ_0 is an MC WF. The choice of the number of SDs in Ψ_0 (i.e. the truncation of Equation (5)) is dependent upon the specific MCSCF method used. This problem will be discussed further below. With MCSCF in practice (when the number of SDs is not close to the FCI limit), a sufficient amount of correlation energy is not recovered; however, a WF that is a qualitatively correct description of the electronic system is often produced [10].

As a note on MCSCF in practice, SDs are not commonly used as a basis for the MCSCF WF because one cannot enforce a total spin symmetry with a SD. Instead, a linear combination of SDs are taken to form configuration state functions (CSFs) that enforce a specific spin symmetry, which are then used as a basis for the MCSCF WF. A theory is referred to as single-reference (SR) if a single CSF is used as a reference WF. If multiple CSFs are used, the theory is referred to as multireference (MR) [10].

A commonly used MCSCF method is the complete active space SCF (CASSCF) method [12]. In CASSCF the choice of which CSFs to include in the MCSCF WF is converted into the problem of choosing an active space of electrons and orbitals. Three spaces are defined in the CASSCF method: inactive, active, and virtual spaces. Orbitals in the inactive space are doubly occupied in all determinants, all possible occupations of the orbitals in the active space are allowed in all CSFs, and the virtual

orbitals are unoccupied in all CSFs. With a generated CASSCF WF, the CI and MO coefficients are variationally optimized to lower the energy of the expectation value of the Hamiltonian operator [10].

Due to the exponential scaling of the computational cost with respect to the size of the active space, there are many systems currently unable to be treated with CASSCF. The RASSCF method provides a way to truncate the CI expansion in Equation (5) such that fewer unimportant configurations are included [13]. The RASSCF method maintains the three orbital spaces defined for the CASSCF method but defines two additional spaces: RAS1 and RAS3. A user-specified number of electrons are excited out of the orbitals in the RAS1 space, and up to a user-specified number of electrons to be excited into the orbitals of the RAS3 space. With these spaces defined, a RASSCF trial WF is generated that is then optimized as in CASSCF.

The RASSCF and CASSCF methods as described so far are state specific in that the CI and MO coefficients are optimized for a single state. This is not convenient for modeling all phenomena, such as excited states and near-degenerate states. A practical alternative is a state-averaged (SA) MCSCF, which simultaneously optimizes several orthogonal, noninteracting electronic states [14]. In SA-MCSCF theory, the CI coefficients and a single set of MO coefficients are variationally optimized to lower the state-averaged electronic energy

$$E_{\mathrm{SA}} = \sum_{L} w_L \langle \Psi_L | \hat{H} | \Psi_L \rangle \tag{15}$$

where L is an index over orthogonal MCSCF (CASSCF or RASSCF) states $|\Psi_L\rangle$, and w_L is an arbitrary weight assigned to each state. The expression in Equation (15) is straightforwardly applied to the CASSCF and RASSCF methods to arrive at the SA-CASSCF and SA-RASSCF methods, respectively. One solution to the problem of recovering more electron correlation for an MC WF is multireference perturbation theory (MRPT). MRPT with a MC WF as a reference works in the same manner

as MP2 except there is the added complication of how to partition the Hamiltonian operator into $\hat{H}_0$ and $\hat{V}$ since an MC WF is not an eigenfunction of the Fock operator [10].

Let us focus her on the second-order complete active space perturbation theory with a CASSCF reference WF (CASPT2) method [15, 16]. The CASPT2 method is similar to the MP2 method discussed in Section 1.1.4, but a CASSCF WF is used as the reference WF, and the choice of H_0 is no longer as simple. The separation used in the CASPT2 method is

$$\hat{H}_0 = \hat{P}_0\hat{F}\hat{P}_0 + \hat{P}_K\hat{F}\hat{P}_K + \hat{P}_{SD}\hat{F}\hat{P}_{SD} \tag{16}$$

where $\hat{P} = |\Psi\rangle\langle\Psi|$ is a projection operator that projects the CASSCF WF onto various spaces in Fock space, $\hat{P}_0$ projects onto the subspace spanned by the CASSCF WF, $\hat{P}_K$ projects on the orthogonal complement space to the 0 space in the CASCI space, and $\hat{P}_{SD}$ projects the space spanned by WFs of single and double excitations out of $|\Psi_0\rangle$ that are not included in 0 or K space. The purpose of this zeroth-order Hamiltonian choice is to force the CASSCF WF to be an eigenfunction of $\hat{H}_0$. Since this method only uses a single multireference state, it is also referred to as the single state CASPT2 (SS-CASPT2) method. The CASPT2 method often includes an empirical energy shift based on the ionization energies (IEs) and electron affinities (EAs) of atoms [17].

The second-order restricted active space perturbation (RASPT2) method is analogous to to the CASPT2 method except a RASSCF WF is used as the reference [18]. The zeroth-order Hamiltonian takes on the same form as in Equation (16), but the Fock operator does not include any couplings between the active, RAS1, and RAS3 spaces.

The CASPT2 and RASPT2 methods can be used in conjunction with a SA-CASSCF or SA-RASSCF WF, respectively, as a reference. The SS-RASPT2 method

applied to a SA-RASSCF WF will result in the perturbation of each state, independent of the other states. There are cases where a SS treatment is no longer sufficient, such as avoided crossings along a potential energy surface [19]. The multi-state RASPT2 (MS-RASPT2) method is a method that can treat such systems better than SS-RASPT2 [20]. MS-RASPT2 is different than the SS-RASPT2 method because MS-RASPT2 couples states from a reference SA-RASSCF WF.

1.1.6 Kohn-Sham Density Functional Theory

In this section we will introduce a formalism separate from WF theory known as Kohn-Sham density functional theory (KS-DFT), one optimizes the electron density of the electronic system

$$\rho(\mathbf{r}) = \sum_{i}^{\text{occ}} |\phi_i|^2 \tag{17}$$

where ρ is an electron density, $\mathbf{r}$ is a spatial coordinate, and i is an index over occupied spin orbital ϕ_i [3, 21, 22].

In KS-DFT one does not try to reach the FCI limit with respect to Equation (5) in Section 1.1.2. Instead, one analyzes a fictitious system for which a single SD is the exact WF, an N-electron system with non-interacting electrons (the electrons still interact with the nuclei). A potential term known as the local potential is added to the non-interacting electronic kinetic energy. The local potential is an effective 1-electron potential that is chosen such that the electron density of the fictitious system equals that of the interacting system. [3, 21, 22] It can be shown that the local potential to reproduce the exact electronic density of the interacting system is

$$\hat{f}_{\text{KS}} = \hat{T}_{\text{S}} + \hat{V}_{\text{S}} = \hat{T}_{\text{S}} + \left[\hat{J} + \hat{V}_{\text{XC}} - \hat{V}_{\text{iA}}\right] \tag{18}$$

where $\hat{f}_{\text{KS}}$ is one-electron Fock operator in KS-DFT, $\hat{T}_{\text{S}}$ is the kinetic energy of the non-interacting system defined as the first term in Equation (3), $\hat{V}_{\text{S}}$ is the local potential, $\hat{J}$ is the coulomb operator defined in Equation (8), $\hat{V}_{\text{XC}}$ is the exchange-

correlation potential, and $\hat{V}_{\mathrm{iA}}$ is the nuclear-electron attraction defined as the second term in Equation (3) [21]. $\hat{V}_{\mathrm{XC}}$ is defined as

$$\hat{V}_{\mathrm{XC}} \equiv \frac{\partial E_{\mathrm{XC}}[\rho(\mathbf{r})]}{\partial \rho(\mathbf{r})} \tag{19}$$

where E_{XC} is the exchange-correlation energy. The exchange-correlation energy is the additional kinetic energy due to the interacting electrons and the quantum mechanical contribution to the electron-electron repulsion. It is important to note that this theory is exact if the universal exchange-correlation functional is known [21].

The electronic part of the Kohn-Sham density functional theory energy function is

$$\begin{aligned} E[\rho(\mathbf{r})] &= T_{\mathrm{S}}[\rho(\mathbf{r})] + J[\rho(\mathbf{r})] + E_{\mathrm{XC}}[\rho(\mathbf{r})] + E_{\mathrm{iA}}[\rho(\mathbf{r})] \\ &= -\frac{1}{2}\sum_{a}\langle\phi[\rho(\mathbf{r})]|\hat{T}_{\mathrm{S}}|\phi[\rho(\mathbf{r})]\rangle + \frac{1}{2}\iint \mathrm{d}\mathbf{r}_1\mathrm{d}\mathbf{r}_2\frac{\rho(\mathbf{r}_1)\rho(\mathbf{r}_2)}{r_{12}} + E_{\mathrm{XC}}[\rho(\mathbf{r})] \\ &+ \int V_{iA}\rho(\mathbf{r})\mathrm{d}\mathbf{r} \end{aligned} \tag{20}$$

where form of the universal exact E_{XC} is not presented because it is currently unknown [3, 21, 22]. The form used to approximate E_{XC} is dependent upon the method used and will not be discussed further.

2 Benchmarking Multiconfiguration Pair-Density Functional Theory on Vertical Excitation Energies

2.1 Review of Multiconfiguration Pair-Density Functional Theory

The kinetic energy, density, and on-top pair-density are taken from a converged MC-SCF calculation, and the other electronic energy contributions are computed post-SCF as functionals of the density and on-top pair-density

$$E\left[\rho,\Pi\right]=\sum_{pq}h_{pq}D_{pq}+\frac{1}{2}\sum_{pqrs}g_{pqrs}D_{pq}D_{rs}+E_{\mathrm{ot}}\left[\rho,\Pi\right]+V_{\mathrm{NN}} \tag{21}$$

where ρ is the density; Π is the on-top pair density; p, q, r, and s are generic orbital indices; h_{pq} are the one-electron integrals; D_{pq} is a one-electron density matrix element; g_{pqrs} are the two-electron integrals; E_{ot} is the on-top energy; and V_{NN} is the internuclear repulsion. The first term is the electronic kinetic energy and nuclear-electron attraction and the second term is the classical Coulombic repulsion of the electrons. The on-top energy is analogous to the exchange-correlation energy in Kohn-Sham density functional theory (KS-DFT), and it includes a correction to the MCSCF kinetic energy plus exchange and electron correlation.

An important aspect of the comparison of MC-PDFT to TD-KS-DFT is their treatment of symmetry. The TD-KS-DFT method represents the electron density of the ground state as a single Slater determinant and the excited states as the linear response of that determinant to a frequency-dependent field, and neither ground nor excited states necessarily have the correct spatial or spin symmetry. MC-PDFT represents the densities and on-top pair densities of all states by multiconfigurational

wave functions of the correct spatial and spin symmetry. However, MC-PDFT has the added cost of configuration interaction (CI) coefficient optimization during the MCSCF calculation, which dominates the cost in the limit of large configuration expansions.

2.2 Intermolecular Charge Transfer

2.2.1 Computational Details

MC-PDFT is designed to represent the state of any single-reference or multireference system with a well-defined wave function and then compute the energy, including a good description of dynamic correlation, by an inexpensive method. In previous work, we used single-state CASSCF wave functions for the first step; for the present work we have extended this for some of the excited-state calculations to the state-average [14] (SA) version, which we have incorporated into the Molcas 7.9 electronic structure package [23]. CASSCF variationally optimized for the energy averaged over N states will be called SA(N)-CASSCF.

All CASSCF, CASPT2, and MC-PDFT calculations are done nonrelativistically in a locally modified version of Molcas. Reasonable active spaces are chosen for calculations, and they are specified in footnotes to the tables, in which the active space for a particular calculation is labeled as (m,n) where m is the number of electrons in the active space, and n is number of active orbitals. In all cases the same active space is used for CASSCF, CASPT2, and MC-PDFT calculations on a given system. All CASPT2 calculations were performed with the standard imaginary shift [24] of 5.44 eV and the default IPEA shift [17] of 6.80 eV.

All KS-DFT calculations are done using the Gaussian 09 [25] software, and the equation-of-motion coupled cluster with singles and doubles (EOM-CCSD) [26–28] and δ-CR-EOMCC(2,3),A [29,30] calculations are done using the GAMESS [31] soft-

ware package with the 2013 patch.

2.2.2 Intermolecular Charge-Transfer Excitation for the H2NH$\cdots$HNO2 System

Excitation energies obtained in this section are compared with both with KS-DFT and with high-level wave function calculations (EOM-CCSD [26–28], SAC-CI [32,33], δ-CR-EOMCC(2,3),A [29,30], or MS-CASPT2 [20]) . At long range, a charge transfer excitation energy should follow the asymptotic equation

$$\omega_{\mathrm{CT}}(R) \quad \underset{R\to\infty}{\sim} \quad \mathrm{IP_D} + \mathrm{EA_A} - \frac{1}{R} \tag{22}$$

where $\mathrm{IP_D}$ is the ionization potential of the donor, $\mathrm{EA_A}$ is the electron affinity of the acceptor, and R is the distance between the donor and acceptor centers. Equation 22 is equally applicable to singlet and triplet charge-transfer excitation energies.

Table 1: Excitation Energies (in eV) of the $^1A_1$ Charge-Transfer Excited State of $NH_3\cdots HNO_2$[a] [34]

distance (Å)	EOM-CCSD	MS-CASPT2	δ-CR-EOMCC(2,3),A
3.6772	7.51	7.10	6.84
6.1133	8.58	8.22	8.04
8.5632	9.15	8.75	8.52
MUE[b]	0.61	0.22	

[a] All calculations are done with the jul-cc-pVTZ [35] basis set. All geometries are obtained from Reference [36]. The active space for MS-CASPT2 is (2,2). For MS-CASPT2, the ground- and excited-state energies are obtained by averaging over two states. [b] The mean unsigned error (MUE) is computed with respect to δ-CR-EOMCC(2,3),A.

First, we consider charge-transfer excitation energies and their behavior with increasing distance R between the donor N atom and acceptor N atom for the $H_2NH\cdots HNO_2$ system that was suggested [36] as a prototype singlet intermolecular charge-transfer system by Song and Hirao. For comparison, we calculated the excita-

tion energy by a very accurate method, δ-CR-EOMCC(2,3),A, at the three smallest distances and by EOM-CCSD and MS-CASPT2 at all distances. Table 1 shows that, at the three distances where δ-CR-EOMCC(2,3),A is available, it agrees better with the latter. Therefore, we use δ-CR-EOMCC(2,3),A as the reference at the distances where it is available and MS-CASPT2 as the reference at the other distances. The results are in Table 2 and Figure 2. Other than PBE, all the methods in Table 2 predict an increase of excitation energy with the intermolecular distance, as expected from Equation 22. Although PBE0 with 25% Hartree-Fock exchange predicts an excitation energy that increases with R, it severely underestimates excitation energies and the rate of increase of the excitation energy. We also note the large MUEs of the long-range-corrected exchange-correlation functionals. First, consider CAM-B3LYP; this exchange-correlation functional has 65% Hartree-Fock nonlocal exchange in the large-R limit. Although it does not have 100% Hartree-Fock nonlocal exchange at long range, it was developed specifically [37] to improve performance for charge-transfer excitations, and it performs reasonably well for some charge-transfer transitions with intermediate spatial overlap [38] (sometimes even out-performing functionals with 100% Hartree-Fock exchange at large interelectronic separation [39]) but it is not very accurate for this case of charge-transfer between systems whose electron density does not significantly overlap. Next, consider ωB97X; this exchange-correlation functional has 100% Hartree-Fock nonlocal exchange in the large-R limit.

Other than PBE, all the methods in Table 2 predict an increase of excitation energy with the inter-molecular distance, as expected from Equation 22. Although PBE0 with 25% Hartee-Fock exchange predicts an excitation energy that increases with R, it severely underestimates excitation energies and the rate of increase of the excitation energy. We also note the large MUEs of the long-range-corrected exchange-correlation functionals; CAM-B3LYP has 65% Hartree-Fock nonlocal exchange in the large-R limit, and ωB97X has 100% Hartree-Fock nonlocal exchange in the large-R

Table 2: Excitation Energies (in eV) of the $^1A_1$ Charge-Transfer Excited State of $NH_3 \cdots HNO_2$[a] [34]

distance (Å)	SA-CASSCF	PBE[b]	PBE0	ωB97X[b]	CAM-B3LYP[b]	EOM-CCSD	tPBE	MS-CASPT2
3.6772	6.05	2.21	3.94	6.24	5.23	7.51	7.49	7.10
6.1133	7.16	1.85	3.90	7.18	5.70	8.58	8.59	8.22
8.5632	7.69	1.78	3.97	7.71	6.01	9.15	9.16	8.75
11.0156	8.01	1.75	4.03	8.03	6.21	9.47	9.49	9.13
13.4708	8.22	1.74	4.07	8.24	6.34	9.68	9.71	9.35
15.9272	8.37	1.73	4.10	8.39	6.44	9.83	9.86	9.51
18.3868	8.48	1.73	4.13	8.51	6.51	9.95	9.97	9.62
23.3034	8.64	1.72	4.16	8.66	6.61	10.10	10.06	9.77
25.7630	8.70	1.72	4.18	8.72	6.65	10.16	10.11	9.83
MUE[c]	1.06	7.47	5.15	1.04	2.91	0.39	0.40	NA[d]

[a] All calculations are done with the jul-cc-pVTZ [35] basis set. All geometries are obtained from Reference [36]. The active space for SA-CASSCF, MS-CASPT2, and tPBE is (2,2). For SA-CASSCF, MS-CASPT2, and tPBE, the calculations of ground- and excited-state energies are obtained by averaging over two states.
[b] LR-TDDFT is used to calculate excitation energies for PBE,PBE0,ωB97X, and CAM-B3LYP.
[c] The mean unsigned error (MUE) is computed with respect to δ-CR-EOMCC(2,3),A at the three smallest distances (See Table 1) and with respect to MS-CASPT2 at other distances.
[d] NA denotes not applicable (see text).

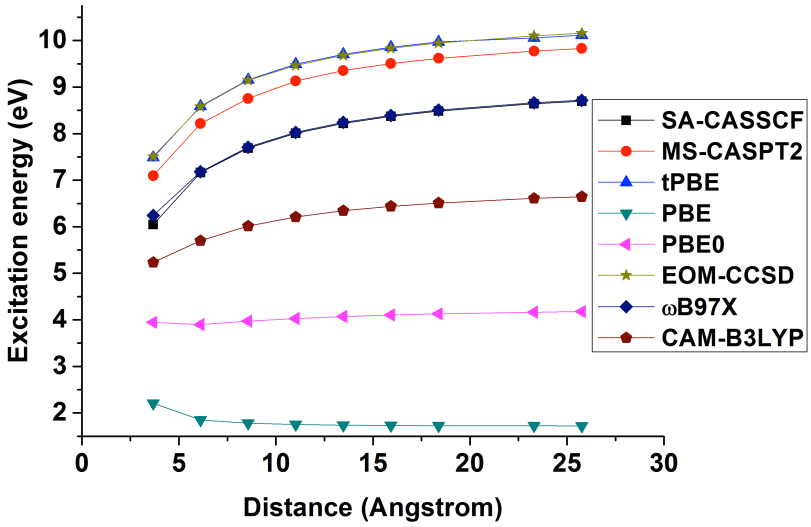

Figure 2: Distance dependence of the $^1A_1$ Charge-Transfer Excited State of $NH_3 \cdots HNO_2$[a]. Note that the tPBE curve is visually indistinguishable from EOM-CCSD. [34]

limit. The unsatisfactory performance of these methods illustrates the comment made in the introduction that even exchange-correlation functionals designed to have improved long-range behavior do not solve the long-range intermolecular charge transfer excitation energy problem. This issue has been studied before by comparing the performance of density functionals with different amount of Hartree-Fock exchange for charge transfer excitations at different overlap region. Even though CAM-B3LYP has only 65% Hartree-Fock exchange at long range, it performs better than many functional with higher Hartree-Fock exchange in many cases. Therefore, adding full Hartree-Fock exchange at long range is not a satisfactory solution of the problem. In this light, the outstanding performance of the MC-PDFT method with the gradient approximation tPBE for the on-top density functional is further validation because this energy is computed with no nonlocal exchange in the energy expression and has an MUE that is as good as EOM-CCSD. Furthermore, unlike MS-CASPT2, MC-PDFT does not require an empirical IPEA shift, and the cost, memory requirements,

and computational scaling are all much more affordable.

The EOM-CCSD calculation is even more expensive than MS-CASPT2. One interesting and somewhat unexpected result in Table 2 is the way that tPBE and EOM-CCSD track one another. In fact they have a mean unsigned deviation from one another of only 0.04 eV over the whole range of R.

2.2.3 Triplet charge-transfer excitation energy of ethylene-tetrafluoroethylene dimer

Next, we consider the lowest triplet charge transfer excitation energy ($^3B_2$) for the $C_2H_4 \cdots C_2F_4$ system, again as a function of increasing intermolecular distance. The absolute excitation energies at large R differ because the different methods predict different ionization energies for C_2F_4 and different electron affinities for C_2H_4, so we draw conclusions on the basis of the R dependence. According to Equation 22, the excitation energy should increase as $1/R$ in the long-range region where the subsystem charge clouds do not overlap. We define Δ as the rise in excitation energy over the region from R = 9 Å to R = 15 Å. Assuming that both of these distances are in the nonoverlapping region, Equation 22 leads to the expectation that $\Delta = 0.64$ eV. Table 3 gives our computed excitations in this case, and the last row of the table gives the Δ values.

In Table 3, CASSCF, CASPT2, and tPBE all have the correct long-range behavior, with Δ close to 0.64 eV. On the other hand both PBE and PBE0 seriously underestimate the excitation energies and show the wrong long-range dependence as functions of R. Although tPBE overestimates the excitation energy at $R \to \infty$, it is a huge improvement over PBE, PBE0, and CASSCF. The table shows that it is even better than CAM-B3LYP for the excitation energy in the large-R limit, although in this triplet case the ωB97X functional, with 100% Hartree-Fock nonlocal exchange at large R, is in much better agreement with MS-CASPT2 value of the large-R limit of

the excitation energy.

Table 3: Excitation Energies (in eV) of the $^3B_2$ Charge-Transfer Excited State of $C_2F_4 \cdots C_2H_4$[a] [34]

distance (Å)	SA-CASSCF	MS-CASPT2	tPBE	PBE[b]	PBE0[b]	ωB97X[b]	CAM-B3LYP[b]
5	12.68	9.85	10.71	5.04	6.72	9.05	7.20
6	13.23	10.35	11.25	5.10	6.91	9.90	8.45
7	13.59	10.68	11.61	5.13	7.15	10.18	8.63
8	13.93	10.91	11.88	5.15	7.20	10.42	9.05
9	14.13	11.10	12.08	5.16	7.26	10.61	9.19
10	14.29	11.26	12.24	5.16	7.30	10.76	9.28
11	14.43	11.39	12.38	5.17	7.34	10.89	9.34
12	14.54	11.50	12.49	5.17	7.37	11.00	9.42
13	14.63	11.59	12.58	5.17	7.39	11.09	9.48
14	14.72	11.67	12.66	5.17	7.42	11.17	9.53
15	14.78	11.74	12.73	5.17	7.42	11.24	9.57
Δ	0.65	0.64	0.65	0.01	0.26	0.63	0.38

[a] All calculations are done with the aug-cc-pVDZ [40] basis set. The geometry at 8 Åis obtained from Reference [41]. The rest of the geometries are obtained by changing the intermolecular distance between the two molecules while freezing the other internal degrees of freedom. The active space for SA-CASSCF, MS-CASPT2, and tPBE is (4,4). For SA-CASSCF, MS-CASPT2, and tPBE, the ground state calculation was state-specific, and the excited state was obtained by averaging over four triplet states. The active space includes the π and π^* orbitals of C_2H_4 and C_2F_4.
[b] LR-TDDFT is used to calculate excitation energies for PBE, PBE0, ωB97X, and CAM-B3LYP.
[c] Δ is the difference in excitation energies at R = 9 and 15 Å; the reference value of Δ is 0.64 eV (see text).

2.2.4 Triplet charge transfer excitation energy for $NH_3 \cdots F_2$ at 6 Å

Table 4 shows excitation energies for the lowest charge transfer excited state, the $^3A_1$ state, in $NH_3 \cdots F_2$ system at an intermolecular distance of 6 Å. The trends present in Table 4 are similar to those already discussed with regards to Table 2, our conclusions are qualitatively the same whether we use CASPT2 or SAC-CI as the reference value. In particular all the density functionals except tPBE underestimate the excitation

energy by more than 1 eV; tPBE is too low compared to SAC-CI and too high compared to CASPT2. In fact, tPBE, even outperforms the long-range-corrected functionals (ωB97X and CAM-B3LYP).

Table 4: Excitation Energies (in eV) of the $^3A_1$ Charge-Transfer Excited State of $NH_3 \cdots F_2$ at a separation distance of 6 Å.[a] [34]

	Excitation Energy
CASSCF	7.58
CASPT2	7.66
tPBE	8.32
PBE[b]	0.12
PBE0[b]	2.83
ωB97X[b]	6.20
CAM-B3LYP[b]	4.65
SAC-CI [41]	9.46

[a] All calculations are done with the 6-31+G** [42] basis set. The geometry was obtained from Reference [41]. A (2,5) active space was used. The ground- and excited-state energies are obtained by state-specific calculations for CASSCF, CASPT2, and tPBE. [b] The LR-TDDFT formalism was used.

2.3 Basis Set Dependence of Rydberg Excitations

2.3.1 Computational Details

The CASSCF, CASPT2, and tPBE calculations were performed in a locally modified developer version of Molcas 7.9 [23]. The CASSCF calculations in this work were state-averaged (SA) [14], where the number of states averaged is equal to the sum of the number of degenerate components for each state for atoms (e.g., an S to P excitation averages over 4 states), and equal weights were assigned to each of the states averaged. The formaldehyde calculation was averaged over three states that were equally weighted. Defining n as the number of valence electrons, we used an active space of n electrons in 4 orbitals (the s and p orbitals), for valence states of atoms and n electrons in 5 orbitals (s and p subshells plus an additional diffuse

s orbital) for Rydberg states of atoms. For formaldehyde we used an active space of 2 electrons in 3 orbitals (n orbital on oxygen, π^* orbital of the carbonyl, and a carbon Rydberg orbital). The resulting state-averaged wave function was the first step, providing the reference wave function for both the CASPT2 and the tPBE calculations. The CASPT2 calculations were done with multi-state CASPT2 (MS-CASPT2); they used a standard imaginary shift [24] of 5.44 eV to alleviate intruder-state problems, and they incorporated the standard empirical IPEA shift [17] of 6.80 eV.

The PBE and PBE0 calculations were performed with standard linear-response TD-KS-DFT using Gaussian 09 [25]. The reference Slater determinant used was unrestricted, and we used the lowest-energy excited state with the correct orbital character that has $M_S = S$ (where S is the total spin quantum number of the ground state) and with an $\langle S^2 \rangle$ that deviates by less than 1.5 from the desired value (since a state excluded by this criterion does not adequately model a same-spin excitation). For atoms with a degenerate ground state, we ignored the excitations that correspond to them. For example, consider an atom like boron with a P ground state; the TD-KS-DFT reference would be one component of the P state, and the first two excitations from that reference are the other two components of the P state. We ignored those excitations. After the ignored excited states are removed from consideration, we chose the lowest-energy solution that has the orbital character of the desired excited state.

2.3.2 Results

To test MC-PDFT, we applied the tPBE functional to the lowest-energy spin-conserving excitations of all 19 atoms from H to K. We chose not to go beyond potassium to avoid the added complication of d orbitals. In addition to the calculations on atoms, we computed the lowest spin-conserving Rydberg excitation of formaldehyde. To compare density functional theory to wave function theory (WFT), we calculate the excitation

energies with a robust but more expensive multireference method, namely complete active space second-order perturbation theory (CASPT2) [15]. We also present complete active space self-consistent field (CASSCF) [12] results since the CASSCF wave function is used in generating the CASPT2 and tPBE results. Finally we compare to TD-KS-DFT calculations with the PBE [43] and PBE0 [44] exchange-correlation functionals. This comparison is of interest since the PBE exchange-correlation functional is used to generate the tPBE [4] functional.

We report our first set of findings in Table 5, where we compare our calculations to experimental values taken from the NIST database [45]. Table 5 shows that tPBE is less accurate than CASPT2 (mean unsigned error MUE of 0.22 eV), which is, however, not a candidate for applications to large systems due its unaffordable cost. In comparing more affordable methods based on density functionals, we see that tPBE with an MUE of 0.42 eV outperforms PBE, which has an MUE of 0.74 eV, and performs in a comparable fashion to PBE0, which has an MUE of 0.45 eV. Curiously, the CASSCF method performs better than expected for these cases, with an MUE of 0.41 eV, which is surprising since CASSCF lacks dynamic correlation; we shall return to this finding below.

In Table 5 we also report also the standard deviation, SD, of the signed errors from their mean. This gives an indication of the width of the distribution of signed errors.

In addition to providing the above general test of MC-PDFT for excitation energies, we analyzed the basis set dependence for Rydberg excitations computed with MC-PDFT. Specifically, we analyzed the question of whether results for Rydberg excitations deteriorate in accuracy upon the addition of a set of diffuse basis functions, as is often the case for TD-KS-DFT. To test this question, we selected the Rydberg excitations of first-row and second-row atoms from Table 5 and computed excitation energies with the d-aug-cc-pVQZ [49] basis set, which has two sets of diffuse basis

Table 5: Excitation energies (in eV) of atoms. The def2-QZVP [46] basis set was used for the valence excitations (Li, Be, Na, Mg, K), and aug-cc-pVQZ [40, 47–49] was used for Rydberg excitations (the other atoms). [50]

	states	CASSCF	CASPT2	tPBE[a]	PBE[b]	PBE0[b]	exp [45]
H	^{2}S-^{2}S	10.22	10.22	9.88	8.05	8.67	10.20
He	^{1}S-^{1}S	20.15	20.72	20.42	17.61	18.75	20.62
Li	^{2}S-^{2}P	1.84	1.84	1.60	2.00	1.97	1.85
Be	^{1}S-^{1}P	5.59	5.42	3.82	4.99	4.99	5.28
B	^{2}P-^{2}S	4.51	4.93	5.01	4.14	4.56	4.96
C	^{3}P-^{3}P	6.88	7.52	7.50	6.29	6.90	7.48
N	^{4}S-^{4}P	9.31	10.49	9.84	8.76	9.57	10.33
O	^{3}P-^{3}S	10.07	9.79	10.93	8.97	9.62	9.51
F	^{2}P-^{2}P	12.74	13.66	13.67	12.66	13.68	12.98
Ne	^{1}S-^{1}P	15.38	18.05	16.28	15.85	17.02	16.71
Na	^{2}S-^{2}P	1.97	2.05	1.94	2.13	2.09	2.10
Mg	^{1}S-^{1}P	4.04	4.41	3.64	4.24	4.25	4.35
Al	^{2}P-^{2}S	2.71	3.08	3.03	2.73	2.96	3.14
Si	^{3}P-^{3}P	4.48	4.93	4.82	4.29	4.62	4.92
P	^{4}S-^{4}P	6.40	7.04	6.74	6.07	6.52	6.96
S	^{3}P-^{3}S	6.75	7.00	7.50	6.85	7.30	6.82
Cl	^{2}P-^{2}P	8.95	9.52	9.65	8.86	9.41	9.19
Ar	^{1}S-^{1}P	11.25	12.29	11.77	11.04	11.70	11.68
K	^{2}S-^{2}P	1.40	1.57	1.43	1.57	1.53	1.61
MSE[d]		-0.32	0.20	-0.06	-0.71	-0.24	
MUE[e]		0.41	0.22	0.42	0.74	0.45	
SD[f]		0.42	0.35	0.60	0.80	0.63	

[a]MC-PDFT [b]TD-KS-DFT [c] average value obtained from the different calculations [d] mean signed error with respect to experiment [e] mean unsigned error with respect to experiment [f] standard deviation of the signed errors from their mean

functions and with the aug-cc-pVQZ basis set, which is identical except for not having the second set of diffuse functions. The findings are reported in Table 6.

Table 6: Rydberg excitation energies (in eV) of first- and second-row atoms upon doubling the number of diffuse basis functions. [50]

	states	basis set	CASPT2	tPBE[a]	PBE[b]	PBE0[b]	exp [45]
H	^{2}S-^{2}S	aug-cc-pVQZ	10.22	9.88	8.05	8.67	10.20
		d-aug-cc-pVQZ	10.21	9.89	7.64	8.44	
He	^{1}S-^{1}S	aug-cc-pVQZ	20.72	20.42	17.61	18.75	20.62
		d-aug-cc-pVQZ	20.46	20.30	16.21	17.70	
B	^{2}P-^{2}S	aug-cc-pVQZ	4.93	5.01	4.14	4.56	4.96
		d-aug-cc-pVQZ	4.88	5.03	3.85	4.37	
C	^{3}P-^{3}P	aug-cc-pVQZ	7.52	7.50	6.29	6.90	7.48
		d-aug-cc-pVQZ	7.35	7.38	5.77	6.52	
N	^{4}S-^{4}P	aug-cc-pVQZ	10.49	9.84	8.76	9.57	10.33
		d-aug-cc-pVQZ	10.23	9.50	8.00	9.00	
O	^{3}P-^{3}S	aug-cc-pVQZ	9.79	10.93	8.97	9.62	9.51
		d-aug-cc-pVQZ	9.05	10.48	7.59	8.48	
F	^{2}P-^{2}P	aug-cc-pVQZ	13.66	13.67	12.66	13.68	12.98
		d-aug-cc-pVQZ	12.64	12.84	10.31	11.48	
Ne	^{1}S-^{1}P	aug-cc-pVQZ	18.05	16.28	15.85	17.02	16.71
		d-aug-cc-pVQZ	16.63	16.25	13.53	15.01	
MSE[c]		aug-cc-pVQZ	0.20	-0.06	-0.71	-0.24	
		d-aug-cc-pVQZ	-0.17	-0.14	-2.49	-1.47	
MUE[d]		aug-cc-pVQZ	0.22	0.45	0.79	0.50	
		d-aug-cc-pVQZ	0.17	0.40	2.49	1.47	

[a]MC-PDFT [b]TD-KS-DFT [c] mean signed error with respect to experiment [d] mean unsigned error with respect to experiment

The results in Table 6 show a dramatic effect on the TD-KS-DFT results in going from aug-cc-pVQZ to d-aug-cc-pVQZ. The PBE and PBE0 sets of excitation energies both worsen drastically and systematically when an extra set of diffuse basis functions is added. In particular, the PBE MUE increases from 0.79 eV to 2.49 eV, and the PBE0 MUE increases from 0.50 eV to 1.47 eV. The decrease in TD-KS-DFT accuracy as more diffuse functions is consistent with the previous experience summarized in the introductory remarks. This is confirmed by the large magnitude of the mean

signed errors, which are negative. However, tPBE does not have the same behavior as PBE and PBE0; the MUE goes from 0.45 eV with aug-cc-pVQZ to 0.40 eV with d-aug-cc-pVQZ. In fact, the behavior of tPBE with respect to adding more diffuse functions is quite similar to CASPT2 (MUE goes from 0.21 eV to 0.17 eV), which is very encouraging.

Finally, we show an example calculation on a molecule as evidence that the stability of MC-PDFT with respect to diffuse basis functions is present for molecules as well as atoms. In Table 7 the lowest-energy spin-conserving Rydberg state of formaldehyde is reported. The errors with the jul-cc-pVTZ basis set are similar to those with the aug basis sets in Table 6, except that CASSCF is less accurate, which is expected for molecules, and PBE0 is more accurate. When adding an extra set of diffuse functions to formaldehyde, CASPT2 and tPBE errors change by less than 0.10 eV; whereas, the PBE and PBE0 errors change by 0.33 eV and 0.28 eV, respectively. This finding indicates that MC-PDFT is stable upon adding an extra set of diffuse basis functions in the treatment of Rydberg states for molecules as well as for atoms

Table 7: The lowest-energy singlet-to-singlet Rydberg excitation energy (in eV) of formaldehyde upon doubling the number of diffuse basis functions. [50]

basis set	CASSCF	CASPT2	tPBE[a]	PBE[b]	PBE0[b]	Ref[c]
jul-cc-pVTZ [35]	6.32	7.03	6.66	6.11	6.99	7.08
d-jul-cc-pVTZ [35]	6.12	6.88	6.57	5.78	6.71	

[a]MC-PDFT [b]TD-KS-DFT [c] Experimental value from Reference [51].

2.4 General Molecular Excitation Energies

2.4.1 Computational Details

All CASSCF, CASPT2, and tPBE calculations were performed in a locally-modified version of Molcas 7.9 [23]. All CASPT2 calculations used an imaginary shift [24] of 5.44 eV to alleviate intruder states. All CASPT2 calculations in Tables 8 used

the standard empirical IPEA shift [17] value of 6.80 eV. All calculations are done nonrelativistically. All TD-KS-DFT calculations were performed with Gaussian 09 [25]. Benchmarking data has been taken either from experiment or from high-level electronic structure calculations. CCSD [52] geometry optimizations were performed using GaussianÂ 09. We used the jul-cc-pVTZ basis set for molecules with valence excitation, the aug-cc-pVTZ basis set for water, the 6-31+G** basis set for pNA and DMABN, and the aug-cc-pVDZ basis set for B-TCNE. All calculations were done using C_1 symmetry. The benzene, napthalene, furan, hexatriene, water, pNA, DMABN, and B-TCNE calculations were performed by Soumen Ghosh.

2.4.2 Results

Although CASSCF is not expected to yield accurate energetics, it is included in the comparisons since CASPT2 and tPBE both use the CASSCF reference wave function. Since the PBE exchange-correlation functional is used in tPBE, we also present results obtained by TD-KS-DFT using PBE and PBE0. For each molecule we used an active space that includes the main configurations needed to describe the excitations; these results are reported in Table 8 and the active space details can be found in [53], where the notation SA(k)-(m,n) denotes state averaging over k states with m electrons in n active orbitals.

First we consider the results for 18 valence excitations in Table 8. The tPBE functional gives an MUE of only 0.29 eV and does as well as PBE0 and better than PBE. Note that tPBE and PBE are local functionals whereas PBE0 has nonlocal exchange. CASPT2 performs the best among all the methods if consideration is limited to valence excitations.

Next we consider the results in Table 8 for the lowest singlet and triplet excitations of water, which are Rydberg in nature. (The reason why only Rydberg excited states are present may be understood by comparison to the united-atom limit of Ne,

which can only have excitations in which a principal quantum number increases.) Local KS-DFT functionals underestimate Rydberg excitations because of the wrong asymptotic behavior of the exchange-correlation potential, and consequently PBE performs poorly for these two excitations. PBE0 performs relatively better because of the 25% Hartree-Fock exchange. But, tPBE performs remarkably well (MUE of only 0.07 eV). In the charge transfer study (Section 2.2) we have also shown that MC-PDFT is stable to adding diffuse functions, which is important when one treats Rydberg states.

Charge-transfer (CT) excitations represent a great challenge for KS-DFT [36, 54–57]. Previously, we have shown that MC-PDFT performs well for long-range intermolecular charge transfer excitations that are in the small-spatial-overlap region. As reported in Table 8, we have tested tPBE and other methods for both intramolecular and intermolecular excitations. The tPBE functional performs very well, with an MUE of 0.24 eV. For the intermolecular excitations, the overlap is very small, but the overlap is much higher for the intramolecular excitations. The PBE and PBE0 methods perform relatively well for the excitations in large overlap region, but they fail completely for the small-spatial-overlap region. The tPBE method, on the other hand, performs well for all overlap regions, indicating that the performance of the on-top density functional for different excitations does not depend strongly on the extent of overlap between occupied and virtual orbitals.

In practical applications, general spectra contain a mix of valence, Rydberg, and charge transfer excitations or excitations with a mixture of these characters. Therefore, it is most reliable to use methods that treat all three types of excitation accurately. The last two rows of Table 8 give average mean errors in which we weighted valence, Rydberg, and charge transfer excitations each with a weight of one third. MC-PDFT with the simple tPBE functional actually has a slightly smaller average error, when the three categories of excitation are weighted equally, than does

CASPT2, but the small difference is not meaningful; what is more important is that the methods are approximately equally accurate. The MC-PDFT results are not overly sensitive to the choice of the on-top density functional. MC-PDFT is much more accurate than TD-KS-DFT with either the PBE or PBE0 exchange-correlation functional (MUE of 0.20 eV vs. either 0.82 eV or 0.40 eV).

Table 8: Excitation energies (in eV) of a variety of molecular excitations. [53]

	Excitation	CASPT2	tPBE[a]	PBE[b]	PBE0[b]	Ref
Acetaldehyde	$^1A''$	4.27	3.92	4.10	4.25	4.28 [51]
Acetone	$^1A_2$	4.44	4.35	4.20	4.40	4.43 [51]
Formaldehyde	$^1A_2$	3.92	3.55	3.77	3.90	4.00 [51]
Pyrazine	$^1B_{3u}$	4.04	3.86	3.52	3.96	3.97 [58, 59]
Pyridazine	$^1B_1$	3.67	3.24	3.11	3.63	3.60 [51]
Pyridine	$^1B_1$	5.06	4.80	4.32	4.83	4.74 [60, 61]
Pyrimidine	$^1B_1$	4.38	4.06	3.75	4.31	4.18 [62]
s-Tetrazine	$^1B_{3u}$	2.56	2.48	1.84	2.29	2.25 [51]
Ethylene	$^1B_{1u}$	8.16	6.77	7.35	7.46	8.02 [63]
Butadiene	^1B_u	6.51	6.03	5.41	5.63	6.21 [64]
Benzene	$^1B_{2u}$	4.83	5.09	5.14	5.37	4.90 [65]
	$^3B_{1u}$	3.98	4.27	3.91	3.49	4.12 [66]
Napthalene	$^1B_{3u}$	4.21	4.40	4.02	4.38	4.00 [67]
	$^3B_{2u}$	3.18	3.31	2.79	2.54	3.11 [66]
Furan	$^1B_2$	6.32	6.51	5.87	6.04	6.06 [68]
	$^3B_2$	4.08	4.20	3.88	3.57	4.17 [66]
Hexatriene	^1B_u	5.32	5.48	4.42	4.67	4.93 [69]
	^3B_u	2.67	2.74	2.27	1.91	2.69 [66]
Water	Singlet	7.61	7.46	6.36	7.13	7.40 [70]
	Triplet	7.19	7.09	6.01	6.69	7.00 [71]
pNA	$^1A_1$	4.62	3.92	3.55	4.16	4.30[f]
DMABN	$^1A_1$	4.87	4.28	4.36	4.77	4.57 [72]
B-TCNE	^1A	3.84	3.63	1.35	2.08	3.59 [73]
MSE[c] valence		0.11	-0.03	-0.33	-0.17	
MUE[d] valence		0.15	0.29	0.36	0.29	
MSE[c] Rydberg		0.20	0.07	-1.02	-0.29	
MUE[d] Rydberg		0.20	0.07	1.02	0.29	
MSE[c] CT		0.29	-0.21	-1.07	-0.48	
MUE[d] CT		0.29	0.24	1.07	0.62	
Average[e] MSE		0.20	-0.06	-0.81	-0.31	
Average[e] MUE		0.21	0.20	0.82	0.40	

[a]MC-PDFT [b]TD-KS-DFT [c] mean signed error [d] mean unsigned error [e] $\frac{1}{3}$ valence + $\frac{1}{3}$ Rydberg + $\frac{1}{3}$ charge transfer [f] δ-CR-EOMCC(2,3),D [29]/6-31+G**

3 Development of Variational Methods

3.1 First-Order Ground-State Optimization

In this section, a theory that minimizes the ground-state MC-PDFT energy with respect to CI coefficients is considered. In Section 3.1.1, the working equations are derived. In Section 3.1.2, an explicit form for the one- and two-electron on-top potentials for the tLSDA on-top potential are derived. In Section 3.1.3, results on ground-state N_2 are reported. Finally, in section 3.1.4, the theory derived in Section 3.1.1 is extended to excited states, and a major problem is explained.

3.1.1 Working Equations

Let us begin with the form of the energy for MC-PDFT in an MO basis using the MCSCF reference function (introduced in Section 2.1)

$$E_{\mathrm{PDFT}}\left[\rho,\Pi\right]=\sum_{pq}h_{pq}D_{pq}+\frac{1}{2}\sum_{pqrs}g_{pqrs}D_{pq}D_{rs}+E_{\mathrm{ot}}\left[\rho,\Pi\right]+V_{\mathrm{NN}} \tag{23}$$

where ρ is the density; Π is the on-top pair density; p, q, r, and s are generic orbital indices; h_{pq} are the one-electron integrals; D_{pq} is a one-electron density matrix element; g_{pqrs} are the two-electron integrals; E_{ot} is the on-top energy; and V_{NN} is the internuclear repulsion. The initial guess for the wave function is multireference

$$\left|0\right\rangle=\sum_{I}^{N^{\mathrm{conf}}}C_{I}\left|I\right\rangle \tag{24}$$

where I is an index over configurations, N^{conf} is the number of configurations, and C_I is a CI coefficient.

We want to minimize the MC-PDFT energy (Equation 23) with respect to the CI coefficients (C_I in Equation 24) while maintaining the orthonormality of the configurations. A practical way of proceeding is to consider a unitary transformation to a

new set of CI coefficients

$$\left|\tilde{0}\right\rangle = \sum_{I}^{N^{\text{conf}}} \tilde{C}_I \left|I\right\rangle = \exp\left(-\hat{P}\right)\left|0\right\rangle \tag{25}$$

$$\hat{P} = \sum_{n}^{N^{\text{conf}}} \left(\tilde{C}_n - C_n\right)\left[\left|n\right\rangle\left\langle 0\right| - \left|0\right\rangle\left\langle n\right|\right] \tag{26}$$

where n is a configuration index. Let us consider that the new set of CI coefficients ($\tilde{C}_I$) minimize the MC-PDFT energy

$$\frac{\partial \tilde{E}_{\text{PDFT}}}{\partial \tilde{C}_I} = 0 \tag{27}$$

$$\tilde{E}_{\text{PDFT}}\left[\tilde{\rho}, \tilde{\Pi}\right] = \sum_{pq} h_{pq}\tilde{D}_{pq} + \frac{1}{2}\sum_{pqrs} g_{pqrs}\tilde{D}_{pq}\tilde{D}_{rs} + E_{\text{ot}}\left[\tilde{\rho}, \tilde{\Pi}\right] + V_{\text{NN}} \tag{28}$$

where the tilde indicates that the new CI coefficients are used

$$\tilde{D}_{pq} = \sum_{I,J} \tilde{C}_I \tilde{C}_J \left\langle I\right| \hat{E}_{pq} \left|J\right\rangle \tag{29}$$

$$\tilde{d}_{pqrs} = \sum_{I,J} \tilde{C}_I \tilde{C}_J \left\langle I\right| \hat{e}_{pqrs} \left|J\right\rangle \tag{30}$$

$$\tilde{\rho} = \sum_{pq} \phi_p \phi_q \tilde{D}_{pq} \tag{31}$$

$$\tilde{\Pi} = \sum_{pqrs} \phi_p \phi_q \phi_r \phi_s \tilde{d}_{pqrs} \tag{32}$$

where I and J are configuration indices and ϕ are molecular orbitals.

To derive a set of equations that upon solution will give CI coefficients that minimize the MC-PDFT energy, Equation 28 is plugged into Equation 27. Derivatives of Equations 29-32 are needed since they are dependent on the CI coefficients. Before the derivatives can be evaluated, we need expressions for Equations 29-32 in terms of the initial-guess CI coefficients. A BCH expansion [10] can be used to accomplish

this

$$\exp(\mathbf{A})\mathbf{B}\exp(-\mathbf{A}) = \mathbf{B} + [\mathbf{B},\mathbf{A}] + \ldots \quad \overset{\rightarrow}{\text{1st-order}} \quad \mathbf{B} + [\mathbf{B},\mathbf{A}] \tag{33}$$

where $\mathbf{A}$ and $\mathbf{B}$ are real, square matrices, $\mathbf{B}$ is not a function of $\mathbf{A}$, and higher than first-order corrections are neglected. The first-order corrected density matrices can now be computed by applying Equation 33 in operator form to Equations 29 and 30

$$\tilde{D}_{pq} = \langle 0| \exp\left(\hat{P}\right) \hat{E}_{pq} \exp\left(-\hat{P}\right) |0\rangle = \langle 0| \hat{E}_{pq} + \left[\hat{E}_{pq}, \hat{P}\right] |0\rangle \tag{34}$$

$$\tilde{d}_{pqrs} = \langle 0| \exp\left(\hat{P}\right) \hat{e}_{pqrs} \exp\left(-\hat{P}\right) |0\rangle = \langle 0| \hat{e}_{pqrs} + \left[\hat{e}_{pqrs}, \hat{P}\right] |0\rangle \tag{35}$$

which leads to the following expressions

$$\tilde{D}_{pq} = D_{pq} + 2\sum_{n} \left[\left(\tilde{C}_n - C_n\right) \left(\langle n| \hat{E}_{pq} |0\rangle - \langle n|0\rangle D_{pq}\right)\right] \tag{36}$$

$$\tilde{d}_{pqrs} = d_{pqrs} + 2\sum_{n} \left[\left(\tilde{C}_n - C_n\right) \left(\langle n| \hat{e}_{pqrs} |0\rangle - \langle n|0\rangle d_{pqrs}\right)\right] \tag{37}$$

and straightforward gradient expressions

$$\frac{\partial \tilde{D}_{pq}}{\partial \tilde{C}_I} = 2\left(\langle I| \hat{E}_{pq} |0\rangle - \langle I|0\rangle D_{pq}\right) \tag{38}$$

$$\frac{\partial \tilde{d}_{pqrs}}{\partial \tilde{C}_I} = 2\left(\langle I| \hat{e}_{pqrs} |0\rangle - \langle I|0\rangle d_{pqrs}\right). \tag{39}$$

The derivatives in Equations 38 and 39 can be plugged into the following expression

$$\frac{\partial}{\partial \tilde{C}_I}\left(\sum_{pq} h_{pq}\tilde{D}_{pq} + \frac{1}{2}\sum_{pqrs} g_{pqrs}\tilde{D}_{pq}\tilde{D}_{rs} + E_{\text{ot}}\left[\tilde{\rho}, \tilde{\Pi}\right] + V_{\text{NN}}\right) = 0 \tag{40}$$

resulting in

$$
\begin{aligned}
&2\left[\sum_{pq} h_{pq}\left\langle I\left|\hat{E}_{pq}\right|0\right\rangle + \sum_{pqrs} g_{pqrs}D_{rs}\left\langle I\left|\hat{E}_{pq}\right|0\right\rangle\right] + \frac{\partial}{\partial\tilde{C}_I}E_{\mathrm{ot}}\left[\tilde{\rho},\tilde{\Pi}\right] \\
&= 2\left[\sum_{pq} h_{pq}\left\langle I\left|D_{pq}\right|0\right\rangle + \sum_{pqrs} g_{pqrs}D_{rs}\left\langle I\left|D_{pq}\right|0\right\rangle\right].
\end{aligned}
\tag{41}
$$

The derivative of the on-top energy in Equation 41 can be further simplified via the chain rule

$$
\frac{\partial E_{\mathrm{ot}}\left[\tilde{\rho},\tilde{\Pi}\right]}{\partial\tilde{C}_I} = \sum_{pq}\frac{\partial E_{\mathrm{ot}}\left[\tilde{\rho},\tilde{\Pi}\right]}{\partial\tilde{D}_{pq}}\frac{\partial\tilde{D}_{pq}}{\partial\tilde{C}_I} + \sum_{pqrs}\frac{\partial E_{\mathrm{ot}}\left[\tilde{\rho},\tilde{\Pi}\right]}{\partial\tilde{d}_{pqrs}}\frac{\partial\tilde{d}_{pqrs}}{\partial\tilde{C}_I} \tag{42}
$$

which can be further simplified by plugging Equations 38 and 39 into Equation 42

$$
\sum_{pq}\frac{\partial E_{\mathrm{ot}}\left[\tilde{\rho},\tilde{\Pi}\right]}{\partial\tilde{D}_{pq}}2\left(\left\langle I\right|\hat{E}_{pq}\left|0\right\rangle - \left\langle I|0\right\rangle D_{pq}\right) + \sum_{pqrs}\frac{\partial E_{\mathrm{ot}}\left[\tilde{\rho},\tilde{\Pi}\right]}{\partial\tilde{d}_{pqrs}}2\left(\left\langle I\right|\hat{e}_{pqrs}\left|0\right\rangle - \left\langle I|0\right\rangle d_{pqrs}\right). \tag{43}
$$

Now using the result in Equation 43, Equation 41 can be further simplified

$$
\begin{aligned}
&\sum_{pq} h_{pq}\left\langle I\left|\hat{E}_{pq}\right|0\right\rangle + \sum_{pqrs} g_{pqrs}D_{rs}\left\langle I\left|\hat{E}_{pq}\right|0\right\rangle + \sum_{pq}\nu_{pq}^{\mathrm{OE}}\left\langle I\right|\hat{E}_{pq}\left|0\right\rangle + \sum_{pqrs}\nu_{pqrs}^{\mathrm{TE}}\left\langle I\right|\hat{e}_{pqrs}\left|0\right\rangle \\
&= \sum_{pq} h_{pq}\left\langle I\left|D_{pq}\right|0\right\rangle + \sum_{pqrs} g_{pqrs}D_{rs}\left\langle I\left|D_{pq}\right|0\right\rangle + \sum_{pq}\nu_{pq}^{\mathrm{OE}}\left\langle I\left|D_{pq}\right|0\right\rangle + \sum_{pqrs}\nu_{pqrs}^{\mathrm{TE}}\left\langle I\left|d_{pqrs}\right|0\right\rangle
\end{aligned}
\tag{44}
$$

$$
\nu_{pq}^{\mathrm{OE}} = \frac{\partial E_{\mathrm{ot}}\left[\tilde{\rho},\tilde{\Pi}\right]}{\partial\tilde{D}_{pq}} \tag{45}
$$

$$
\nu_{pqrs}^{\mathrm{TE}} = \frac{\partial E_{\mathrm{ot}}\left[\tilde{\rho},\tilde{\Pi}\right]}{\partial\tilde{d}_{pqrs}} \tag{46}
$$

where the one-electron on-top potential (ν_{pq}^{OE}) and two- electron on-top potential (ν_{pqrs}^{TE}) are introduced. Equation 44 can be further simplified by collecting like terms

$$
\begin{aligned}
&\left\langle I\left|\sum_{pq}\left(h_{pq} + \sum_{rs} g_{pqrs}D_{rs} + \nu_{pq}^{\mathrm{OE}}\right)\hat{E}_{pq} + \sum_{pqrs}\nu_{pqrs}^{\mathrm{TE}}\hat{e}_{pqrs}\right|0\right\rangle \\
&= \left\langle I\left|\sum_{pq}\left(h_{pq} + \sum_{rs} g_{pqrs}D_{rs} + \nu_{pq}^{\mathrm{OE}}\right)D_{pq} + \sum_{pqrs}\nu_{pqrs}^{\mathrm{TE}}d_{pqrs}\right|0\right\rangle
\end{aligned}
\tag{47}
$$

which can be even further simplified by introducing the CI operator and the eigenvalue

and switching to matrix notation (in a CSF basis)

$$\mathbf{F}^{\mathrm{CI}}\mathbf{C} = E^{\mathrm{eig}}\mathbf{C} \tag{48}$$

where

$$\hat{F}^{\mathrm{CI}} = \sum_{pq}\left(h_{pq} + \sum_{rs} g_{pqrs}D_{rs} + \nu^{\mathrm{OE}}_{pq}\right)\hat{E}_{pq} + \sum_{pqrs}\nu^{\mathrm{TE}}_{pqrs}\hat{e}_{pqrs} \tag{49}$$

$$E^{\mathrm{eig}} = \sum_{pq}\left(h_{pq} + \sum_{rs} g_{pqrs}D_{rs} + \nu^{\mathrm{OE}}_{pq}\right)D_{pq} + \sum_{pqrs}\nu^{\mathrm{TE}}_{pqrs}d_{pqrs}. \tag{50}$$

Equation 48 is the fundamental working equation of the 1st-order CI optimization for ground states. Upon solving Equation 48, CI coefficients that minimize the MC-PDFT energy (Equation 23) will be obtained. Explicit forms of the tLSDA potentials (Equations 45 and 46) will be given in Section 3.1.2. There are three important properties to note:

1. The eigenvalue in Equation 50 is not equal to the MC-PDFT energy (Equation 23).

2. Since the CI operator (Equation 49) is dependent on the CI coefficients, Equation 48 needs to be solved iteratively, unlike in wave function theory (the Hamiltonian is independent of CI coefficients; see Equation 3).

3. This method is a first-order method due to the truncation in Equation 33

First-order CI optimization algorithm

1. Obtain MO coefficients and initial guess to the CI coefficients

2. Build the CI operator (Equation 49)

3. Solve eigenvalue problem (Equation 48) for new CI coefficients

4. Repeat steps 2 and 3 until convergence

5. Compute the MC-PDFT energy (Equation 23) with converged CI coefficients

3.1.2 Explicit On-Top Potential Expression for tLSDA

The solution of Equation 48 requires explicit forms of the one- and two-electron on-top potentials. In this section we will derive explicit expressions for the one- and two-electron on-top potentials (Equations 45 and 46) for the tLSDA on-top functional [4]. The tLSDA functional is shown in Equation 51

$$E_{\mathrm{ot}}^{\mathrm{tLSDA}}\left[\rho,\Pi\right]=E_{\mathrm{xc}}^{\mathrm{LSDA}}\left[\rho_{\alpha}^{\mathrm{t}},\rho_{\beta}^{\mathrm{t}}\right] \tag{51}$$

where

$$\rho_{\alpha}^{\mathrm{t}}=\begin{cases}\frac{\rho}{2}\left(1+\zeta\right)=\frac{\rho}{2}\left(1+\sqrt{1-\frac{4\Pi}{\rho^{2}}}\right) & \mathrm{when}\frac{4\Pi}{\rho^{2}}\leq1\\ \frac{\rho}{2} & \mathrm{when}\frac{4\Pi}{\rho^{2}}>1\end{cases} \tag{52}$$

$$\rho_{\beta}^{\mathrm{t}}=\begin{cases}\frac{\rho}{2}\left(1-\zeta\right)=\frac{\rho}{2}\left(1-\sqrt{1-\frac{4\Pi}{\rho^{2}}}\right) & \mathrm{when}\frac{4\Pi}{\rho^{2}}\leq1\\ \frac{\rho}{2} & \mathrm{when}\frac{4\Pi}{\rho^{2}}>1\end{cases} \tag{53}$$

where $\rho_{\alpha}^{\mathrm{t}}$ is the translated alpha density and $\rho_{\beta}^{\mathrm{t}}$ is the translated beta density.

Let us first evaluate the tLSDA one-electron on-top potential by plugging in the LSDA function expression [74]

$$\frac{\partial E_{\mathrm{xc}}^{\mathrm{LSDA}}\left[\rho_{\alpha}^{\mathrm{t}},\rho_{\beta}^{\mathrm{t}}\right]}{\partial D_{pq}}=\int d\mathbf{r}\left[\frac{\partial\epsilon_{\mathrm{xc}}^{\mathrm{LSDA}}\left[\rho_{\alpha}^{\mathrm{t}},\rho_{\beta}^{\mathrm{t}}\right]}{\partial\rho_{\alpha}^{\mathrm{t}}}\frac{\partial\rho_{\alpha}^{\mathrm{t}}}{\partial D_{pq}}+\frac{\partial\epsilon_{\mathrm{xc}}^{\mathrm{LSDA}}\left[\rho_{\alpha}^{\mathrm{t}},\rho_{\beta}^{\mathrm{t}}\right]}{\partial\rho_{\beta}^{\mathrm{t}}}\frac{\partial\rho_{\beta}^{\mathrm{t}}}{\partial D_{pq}}\right]. \tag{54}$$

The derivatives of the translated spin densities is straightforwardly evaluated by plugging Equations 52 and 53 into Equation 54 (only the alpha part is shown)

$$\nu_{pq}^{\mathrm{OE}}=\begin{cases}\int\left[\frac{\partial\epsilon_{\mathrm{xc}}^{\mathrm{LSDA}}\left[\rho_{\alpha}^{\mathrm{t}},\rho_{\beta}^{\mathrm{t}}\right]}{\partial\rho_{\alpha}^{\mathrm{t}}}\left(\frac{1}{2}\left(1+\zeta\right)+\frac{2\Pi}{\zeta\rho^{2}}\right)\right]\phi_{p}\phi_{q}d\mathbf{r} & \mathrm{when}\frac{4\Pi}{\rho^{2}}\leq1\\ \int\left[\frac{\partial\epsilon_{\mathrm{xc}}^{\mathrm{LSDA}}\left[\rho_{\alpha}^{\mathrm{t}},\rho_{\beta}^{\mathrm{t}}\right]}{\partial\rho_{\alpha}^{\mathrm{t}}}\right]\phi_{p}\phi_{q}d\mathbf{r} & \mathrm{when}\frac{4\Pi}{\rho^{2}}>1.\end{cases} \tag{55}$$

A brief comment regarding the evaluation of Equation 55 is needed. The derivatives of the exchange-correlation functional with respect to the translated spin densities can be evaluated numerically using standard techniques that are used for eval-

uating the Kohn-Sham exchange-correlation potential (Equation 18).

The tLSDA two-electron on-top potential is evaluated in the exact same way as the one-electron on-top potential, resulting in

$$\nu_{pqrs}^{\mathrm{TE}} = \begin{cases} \int \left[\frac{\partial \epsilon_{\mathrm{xc}}^{\mathrm{LSDA}}\left[\rho_\alpha^{\mathrm{t}}, \rho_\beta^{\mathrm{t}}\right]}{\partial \rho_\alpha^{\mathrm{t}}} \left(\frac{-1}{\rho\zeta}\right) + \frac{\partial \epsilon_{\mathrm{xc}}^{\mathrm{LSDA}}\left[\rho_\alpha^{\mathrm{t}}, \rho_\beta^{\mathrm{t}}\right]}{\partial \rho_\beta^{\mathrm{t}}} \left(\frac{1}{\rho\zeta}\right) \right] \phi_p \phi_q \phi_r \phi_s d\mathbf{r} & \text{when} \frac{4\Pi}{\rho^2} \leq 1 \\ 0 & \text{when} \frac{4\Pi}{\rho^2} > 1. \end{cases} \tag{56}$$

3.1.3 CI-tLSDA Application on N_2

3.1.3.1 Computational Details

The CASSCF, tLSDA, and CI-tLSDA calculations were performed in a locally modified developer version of Molcas 8.0 [75]. We used an active space of 6 electrons in 6 orbitals, and the cc-pVDZ basis set was used [47]. No spatial symmetry was applied. The CI-tLSDA convergence was determined by an MC-PDFT energy threshold of 10^{-8}.

3.1.3.2 Results

The N_2 dimer is a challenging test system for electronic structure methods. In Figure 3, one can find the tLSDA and CI-tLSDA potential curves for N_2.

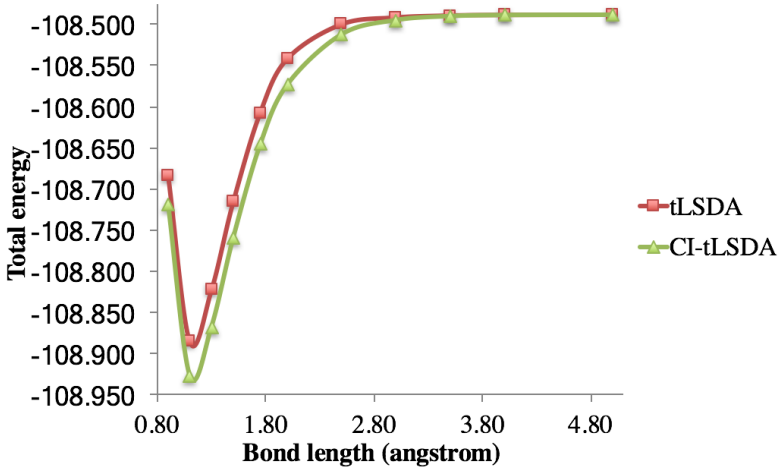

Figure 3: Potential curves of tLSDA and CI-tLSDA for N_2.

The potential curves of ground-state N_2 reveal a startling problem with CI-tLSDA. The total energy is substantially lowered at equilibrium (by about 1.3 eV), where the wave function goes from 97% dominated by the Hartree-Fock configuration to 99%. This finding is quite startling and indicates potential problems with CI optimizations that minimize the MC-PDFT energy (see Section 3.2).

3.1.4 Extension to Excited States

To extend the procedure derived in Section 3.1.1 to excited states, we consider an average energy minimization

$$\frac{\partial}{\partial \tilde{C}_{IA}} \sum_{A}^{N^{\mathrm{sp}}} W_A \left(\sum_{pq} h_{pq} \tilde{D}^A_{pq} + \frac{1}{2} \sum_{pqrs} g_{pqrs} \tilde{D}^A_{pq} \tilde{D}^A_{rs} + E_{\mathrm{ot}} \left[\tilde{\rho}^A, \tilde{\Pi}^A \right] + V_{\mathrm{NN}} \right) = 0 \tag{57}$$

where A is an electronic state index, W_A is a weight, and N^{sp} is the number of states included in the energy averaging. Since we are performing a unitary transformation of a set of states, $\hat{P}$ in Equation 26 needs to include other states then the reference ($|0\rangle$)

$$\hat{P} = \sum_{B}^{N^{\mathrm{sp}}} \sum_{n}^{N^{\mathrm{conf}}} \left(\tilde{C}_{nB} - C_{nB} \right) \left[|n\rangle \langle B| - |B\rangle \langle n| \right]. \tag{58}$$

where B is an index over electronic states. Using the same techniques as in Section 3.1.1 leads to the following eigenvalue problems

$$\mathbf{F}^{\mathrm{CI}}_A \mathbf{C}_A = E^{\mathrm{eig}}_A \mathbf{C}_A \text{ where } A = 1, 2, \ldots, N^{\mathrm{sp}}. \tag{59}$$

The solution of Equation 59 would lead to CI coefficients of several electronic states that minimize the average MC-PDFT energy. However, since the eigenvalue problem for each state is solved separately, the resulting states will not be orthogonal to each other, which is a highly undesirable quality. Two methods were developed that will optimize CI coefficients and lead to orthogonal states. They are covered in Sections 3.2 and 3.3.

3.2 Average Energy Minimization

In Section 3.2.1, a method for minimizing the average MC-PDFT energy, while maintaining orthogonality, is introduced. In Sections 3.2.2 and 3.2.3, results with the new theory are covered.

3.2.1 Theory

As shown in Section 3.1.4 when CI coefficients are variationally optimized to minimize the average energy (Equation 60) for multiple electronic states, the orthogonality of the states will be destroyed

$$E_{\mathrm{PDFT}}^{\mathrm{AVE}} = \sum_{A}^{N^{\mathrm{sp}}} W_A \left(\sum_{pq} h_{pq} D_{pq}^{A} + \frac{1}{2} \sum_{pqrs} g_{pqrs} D_{pq}^{A} D_{rs}^{A} + E_{\mathrm{ot}} \left[\rho^{A}, \Pi^{A} \right] + V_{\mathrm{NN}} \right) \tag{60}$$

where A is an index on electronic states, N^{sp} is the number of electronic states included in the energy averaging, and W_A are user-defined weights. Rather than the CI parameterization used in Equation 58, we introduce a new parameterization that will maintain orthogonality of the electronic states

$$\left|\tilde{0}\right\rangle = \exp\left(-\hat{S}\right)|0\rangle \tag{61}$$

$$\hat{S} = \sum_{I}^{N^{\mathrm{par}}} \sum_{A}^{N^{\mathrm{sp}}} S_{IA} \left(|I\rangle \langle A| - |A\rangle \langle I| \right). \tag{62}$$

where S_{IA} will be referred to as state mixing coefficients and N^{par} is the number of variational parameters in $|0\rangle$. Note that this parameterization is directly applicable to CI coefficient optimizations ($N^{\mathrm{par}} = N^{\mathrm{conf}}$) and state interaction (SI) coefficient optimizations ($N^{\mathrm{par}} = N^{\mathrm{sc}}$ where N^{sc} is the number of CASSCF states).

With the energy function to be minimized defined and the variational parameters determined, now we will derive a method for minimizing the average MC-PDFT energy. We begin by performing a second-order Taylor expansion of the average

MC-PDFT energy functional

$$E^{\mathrm{AVE(SO)}}\left(\boldsymbol{S}\right) = E^{\mathrm{AVE(0)}} + \boldsymbol{\Delta S}^{T}\boldsymbol{E}^{\mathrm{AVE(1)}} + \frac{1}{2}\boldsymbol{\Delta S}^{T}\boldsymbol{E}^{\mathrm{AVE(2)}}\boldsymbol{\Delta S} \tag{63}$$

where $E^{\mathrm{AVE(SO)}}$ is the second-order energy, $\boldsymbol{E}^{\mathrm{AVE(1)}}$ is the gradient of the average MC-PDFT energy, and $\boldsymbol{E}^{\mathrm{AVE(2)}}$ is the Hessian of the average MC-PDFT energy. To minimize the energy functional in Equation 63, we use Newton's Method [10]

$$\boldsymbol{E}_{n}^{\mathrm{AVE(2)}}\boldsymbol{\Delta S}_{n} = -\boldsymbol{E}_{n}^{\mathrm{AVE(1)}} \tag{64}$$

where n denotes an iteration. Each iteration, solution of Equation 64 will result in a new set of state mixing coefficients. Upon convergence, second-order-corrected state mixing coefficients will be obtained. This is referred to as the average-energy formalism.

3.2.2 Computational Details

The two lowest-energy singlet CAS(2,2) wave functions in C_1 spatial symmetry for HeH^+ are $1\sigma^2$ for the ground state (the 1σ is localized on the He atom) and $1\sigma 2\sigma$ for the excited state (the 2σ is localized on the H atom) at all geometries (both are $^1\Sigma^+$ states). The ground state dissociates to $He\ldots H^+$, and the excited state dissociates to $He^+\ldots H$. Thus, a SA(2)-CASSCF/cc-pVTZ calculation in C_1 spatial symmetry was used to generate the reference wave function.

The two lowest-energy singlet CAS(6,6) wave functions in A_1 irrep of C_{2v} spatial symmetry for LiF are $1\sigma^2$ for the ground state (LiF $\sigma(s)$ bond) and $1\sigma 1\sigma^*$ for the excited state at equilibrium (both are $^1\Sigma^+$ states). At 9 Å, the ground state is $Li\ldots F$, and the excited state is the ionic state $Li^+\ldots F^-$. Due to the presence of F^-, aug-cc-pVTZ on F and cc-pVTZ on Li was used. A SA(2)-CASSCF(6,6) calculation in A_1 irrep of C_{2v} spatial symmetry was used to generate the reference wave function. MS-CASPT2 calculations were also performed with the standard imaginary shift [24]

of 5.44 eV and the default IPEA shift [17] of 6.80 eV.

For both HeH^+ and LiF, the SI coefficients of the two CASSCF states were optimized via the theory outlined in Section 3.2.1, where the average MC-PDFT functional used equal weights on two states. The method was implemented in a locally-modified version of Molcas 8.1 [75] and numerical gradients and Hessians were used. The new theory will be referred to as SI-tLSDA in Section 3.2.3.

3.2.3 Results

The 2-state potential energy curve of HeH^+ with CASSCF, tLSDA, and SI-tLSDA are reported in Figures 4, 5, and 6, respectively. The HeH^+ adiabatic potential curves are labeled by their electronic character at dissociation (5 Å).

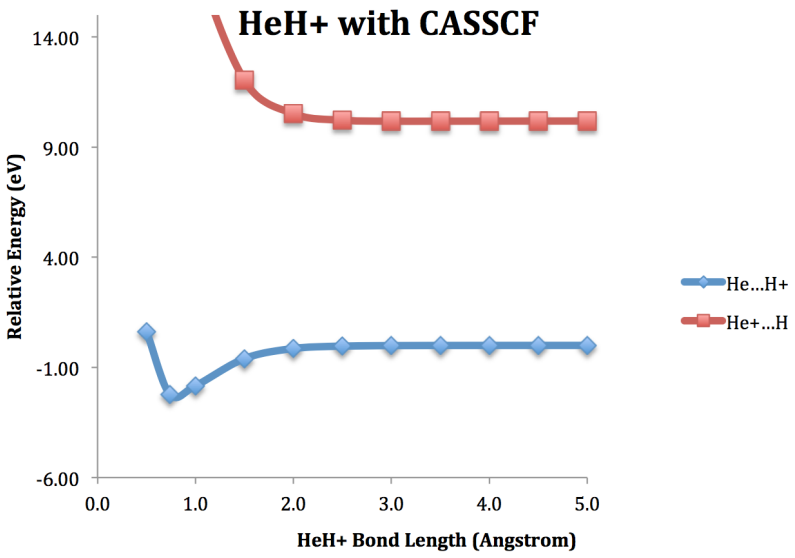

Figure 4: HeH^+ potential curves with CASSCF.

The total energies of CASSCF, tLSDA, and SI-tLSDA and the SI coefficients of SI-tLSDA at equilibrium are reported in Tables 9 and 10, respectively. The total energies of CASSCF, tLSDA, and SI-tLSDA and the SI coefficients of SI-tLSDA at dissociation (5 Å) are reported in Tables 11 and 12, respectively.

The tLSDA results match CASSCF for the ground state, but the excited state energy is significantly different (see Tables 9 and 11). The SI-tLSDA energies dras-

Table 9: Total energies of HeH^+ at equilibrium

state	CASSCF	tLSDA	SI-tLSDA
$1^1\Sigma^+$	-2.931	-2.936	-2.866
$2^1\Sigma^+$	-1.937	-1.999	-2.100
average energy	-2.434	-2.467	-2.483

Table 10: SI coefficients for SI-tLSDA results reported in Table 9.

SI-tLSDA state	CASSCF state	SI-tLSDA SI coeff.
$1^1\Sigma^+$	$1^1\Sigma^+$	0.961
	$2^1\Sigma^+$	-0.278
$2^1\Sigma^+$	$1^1\Sigma^+$	0.278
	$2^1\Sigma^+$	0.961

Table 11: Total energies of HeH^+ at 5 Å

state	CASSCF	tLSDA	SI-tLSDA
$1^1\Sigma^+$	-2.849	-2.849	-2.764
$2^1\Sigma^+$	-2.474	-2.440	-2.763
average energy	-2.662	-2.645	-2.764

Table 12: SI coefficients for SI-tLSDA results reported in Table 11.

SI-tLSDA state	CASSCF state	SI-tLSDA SI coeff.
$1^1\Sigma^+$	$1^1\Sigma^+$	0.708
	$2^1\Sigma^+$	-0.707
$2^1\Sigma^+$	$1^1\Sigma^+$	0.707
	$2^1\Sigma^+$	0.707

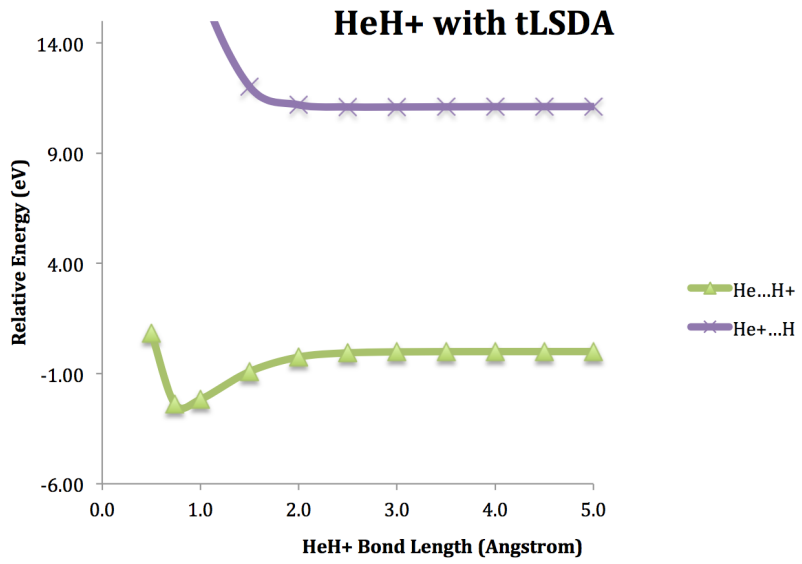

Figure 5: HeH^+ potential curves with tLSDA.

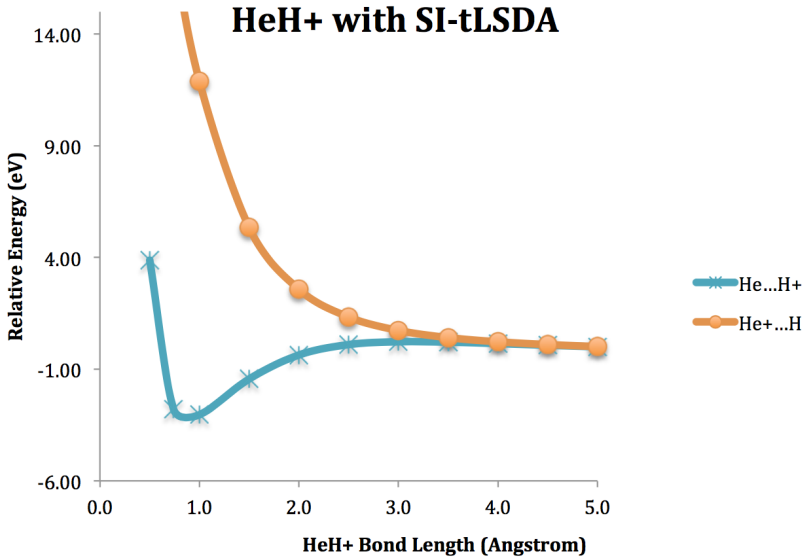

Figure 6: HeH^+ potential curves with SI-tLSDA (average energy formalism).

tically differ from the tLSDA results (compare Figures 5 and 6 or look at Tables 9 and 11). Both states converge to a 50-50 mixture of $He \ldots H^+$ and $He^+ \ldots H$ (the phase in Table 12 does not matter since each MO is localized, and the molecule is at dissociation). This preference of charge-delocalized states is a serious problem of the theory.

The 2-state potential energy curves of LiF with SA(2)-CASSCF, MS-CASPT2,

tLSDA, and SI-tLSDA are reported in Figures 7, 8, 9, and 10, respectively. The adiabatic curves are labeled by their electronic character at 9 Å.

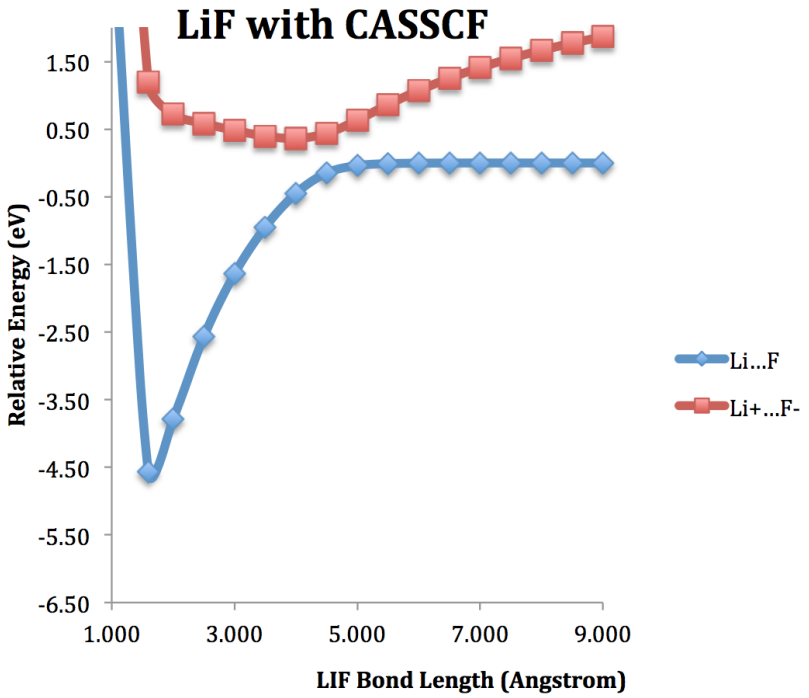

Figure 7: LiF potential curves with CASSCF.

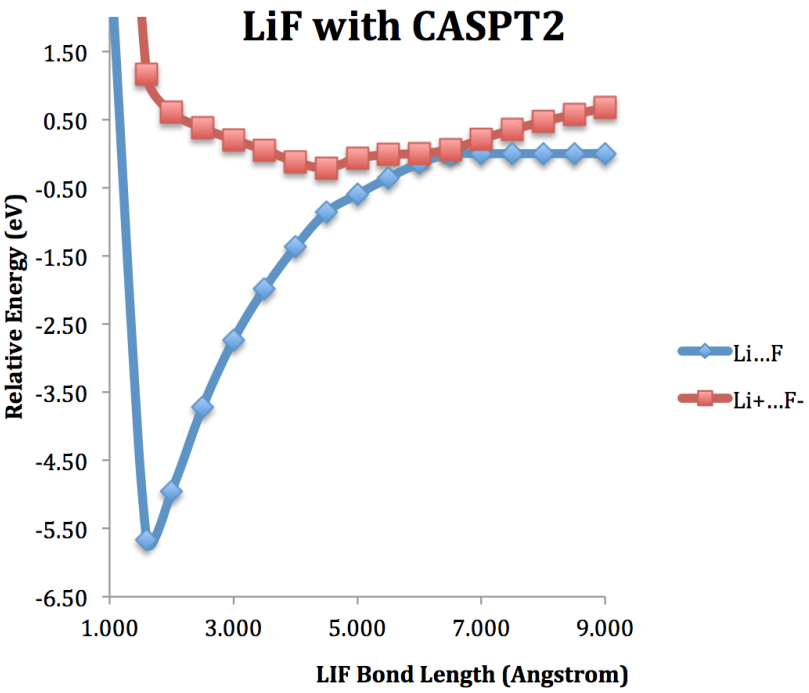

Figure 8: LiF potential curves with MS-CASPT2.

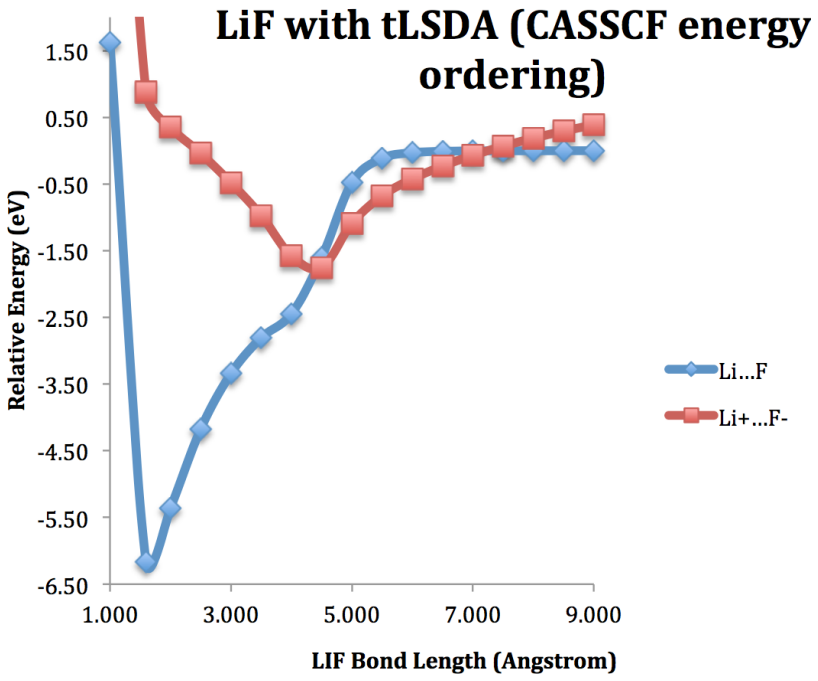

Figure 9: LiF potential curves with tLSDA.

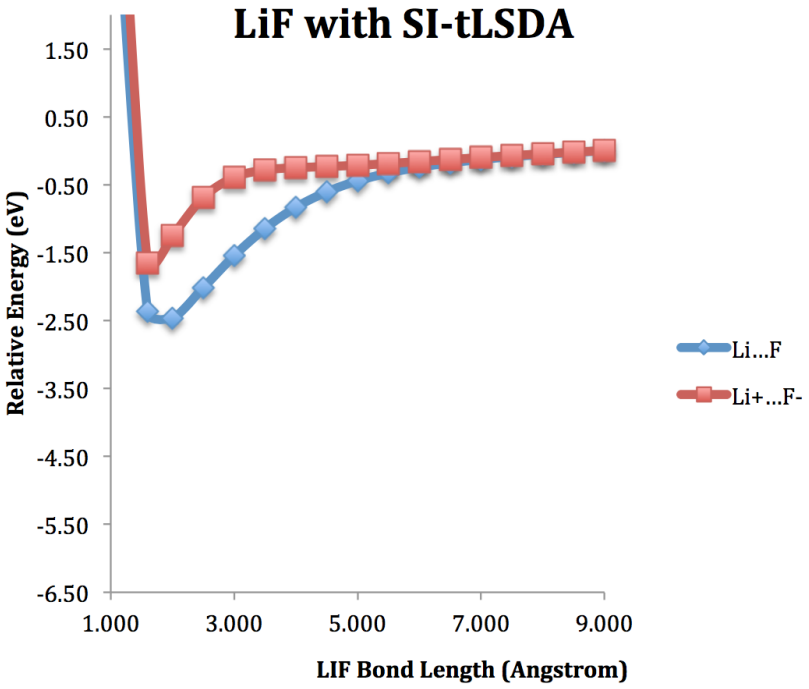

Figure 10: LiF potential curves with SI-tLSDA (average energy formalism).

The total energies of CASSCF, MS-CASPT2, tLSDA, and SI-tLSDA and the SI coefficients of SI-tLSDA at equilibrium are reported in Tables 13 and 14, respectively.

The total energies of CASSCF, MS-CASPT2, tLSDA, and SI-tLSDA and the SI coefficients of SI-tLSDA at dissociation (9 Å) are reported in Tables 15 and 16, respectively. The CSFs are labeled by their character at 9 Å.

Table 13: Total energies of LiF at equilibrium

state	CASSCF	MS-CASPT2	tLSDA	SI-tLSDA
$1^1\Sigma^+$	-107.025	-107.253	-106.878	-106.794
$2^1\Sigma^+$	-106.814	-107.002	-106.619	-106.768
average energy	-106.920	-107.128	-106.748	-106.781

Table 14: SI coefficients for SI-tLSDA results reported in Table 13.

SI-tLSDA state	CASSCF state	SI-tLSDA SI coeff.
$1^1\Sigma^+$	$1^1\Sigma^+$	0.764
	$2^1\Sigma^+$	-0.645
$2^1\Sigma^+$	$1^1\Sigma^+$	0.645
	$2^1\Sigma^+$	0.764

Table 15: Total energies of LiF at 9 Å

state	CASSCF	MS-CASPT2	tLSDA	SI-tLSDA
$1^1\Sigma^+$	-106.858	-107.045	-106.651	-106.707
$2^1\Sigma^+$	-106.789	-107.020	-106.637	-106.707
average energy	-106.823	-107.033	-106.644	-106.707

The CASSCF and CASPT2 results agree qualitatively (compare Figures 7 and 8). The tLSDA curves are qualitatively correct except in the avoided crossing region (see Figure 9). In the avoided crossing region, tLSDA curves have an unphysical double crossing. The SI-tLSDA results exhibit too much mixing of the ionic and covalent states (see Figure 10). At dissociation, the SI-tLSDA results dissociate to a 50-50 mixture of the ionic and covalent states (see Tables 15 and 16). This 50-50 mixing is similar to the SI-tLSDA results for HeH+ at dissociation.

Table 16: SI coefficients for SI-tLSDA results reported in Table 15.

SI-tLSDA state	CASSCF state	SI-tLSDA SI coeff.
$1^1\Sigma^+$	$1^1\Sigma^+$	0.708
	$2^1\Sigma^+$	-0.706
$2^1\Sigma^+$	$1^1\Sigma^+$	0.706
	$2^1\Sigma^+$	0.708

3.3 Average Operator Formulation

In Section 3.3.1, a method for optimizing CI coefficients for a set of states, while maintaining orthogonality, is introduced, referred to as the average CI operator formalism. In Sections 3.3.2 and 3.3.3, results with the new are covered.

3.3.1 Theory

In Section 3.1.4, it was shown that an extension of the 1st-order CI-MC-PDFT to excited states will lead to non-orthogonal states that minimize the average MC-PDFT energy. A way to to maintain orthogonality is to introduce an average CI operator

$$\hat{F}^{\text{Ave}} = \sum_{A}^{N^{\text{sp}}} W_A \hat{F}_A^{\text{CI}} \tag{65}$$

where A is an electronic state, W_A is a user-defined weight, N^{sp} is the number of states included in the averaging, and $\hat{F}^{\text{CI}}$ is the CI operator originally defined in Equation 49. Now a single eigenvalue problem can be solved to obtain new CI coefficients, which will maintain orthogonality

$$\mathbf{F}^{\text{Ave}}\mathbf{C} = E^{\text{Ave}}\mathbf{C} \tag{66}$$

where $\mathbf{F}^{\text{Ave}}$ is the matrix representation of the operator in Equation 66 in a configuration basis and E^{Ave} is an eigenvalue.

Upon iterative solution of Equation 66, new CI coefficients will be obtained for the N^{sp} states, and the states will be orthogonal to each other. However, the new CI coefficients will not minimize the average MC-PDFT energy or the MC-PDFT energy

of each state. The current hypothesis is that the CI coefficients will minimize the averaged sum of the configuration energies (similar to how the eigenvalue in Hartree-Fock and KS-DFT MO optimizations are the sum of orbital energies), but further study is needed. Once the new CI coefficients are obtained, the MC-PDFT energy for each state is computed via the standard MC-PDFT energy functional (Equation 23).

3.3.2 Computational Details

The two lowest-energy singlet CAS(2,2) wave functions in C_1 spatial symmetry for HeH^+ are $1\sigma^2$ for the ground state (the 1σ is localized on the He atom) and $1\sigma 2\sigma$ for the excited state (the 2σ is localized on the H atom) at all geometries (both are $^1\Sigma^+$ states). The ground state dissociates to $He \ldots H^+$, and the excited state dissociates to $He^+ \ldots H$. A SA(2)-CASSCF/cc-pVTZ calculation in C_1 spatial symmetry to study the potential energy curve of HeH^+.

The two lowest-energy singlet CAS(6,6) wave functions in A_1 irrep of C_{2v} spatial symmetry for LiF are $1\sigma^2$ for the ground state (LiF $\sigma(s)$ bond) and $1\sigma 1\sigma^*$ for the excited state at equilibrium (both are $^1\Sigma^+$ states). At 9 Å, the ground state is $Li \ldots F$, and the excited state is the ionic state $Li^+ \ldots F^-$. Due to the presence of F^-, aug-cc-pVTZ on F and cc-pVTZ on Li. The current calculations are done in C_1, but only the two $^1\Sigma^+$ states were studied. A SA(4)-CASSCF(6,6) was used to generate the reference wave function.

For both HeH^+ and LiF, the CI coefficients of the two states were optimized via the theory outlined in Section 3.3.1, where the average CI operator used equal weights on two states. The method was implemented in a locally-modified version of Molcas 8.1 [75] and the one- and two-electron on-top potentials were computed using the form introduced in Section 3.1.2. In Section 3.3.3, we will refer to this new theory as CI-tLSDA.

3.3.3 Results

The 2-state potential energy curve of HeH^+ with CI-tLSDA is reported in Figure 11. The CASSCF, tLSDA, and SI-tLSDA (computed via average energy formalism) potential curves can be found in Figures 4, 5, and 6, respectively.

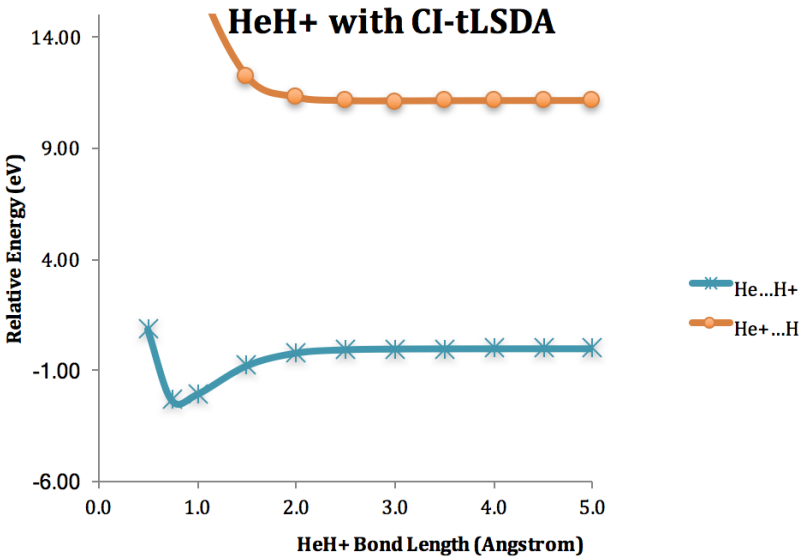

Figure 11: HeH^+ potential curves with CI-tLSDA (average operator formalism).

The total energies of CASSCF, tLSDA, and CI-tLSDA and CI coefficients of CASSCF and CI-tLSDA at equilibrium are reported in Tables 17 and 18, respectively. The total energies of CASSCF, tLSDA, and CI-tLSDA and CI coefficients of CASSCF and CI-tLSDA at dissociation (5 Å) are reported in Tables 19 and 20, respectively.

Table 17: Total energies of HeH^+ at equilibrium

state	CASSCF	tLSDA	CI-tLSDA
$1^1\Sigma^+$	-2.931	-2.936	-2.934
$2^1\Sigma^+$	-1.937	-1.999	-1.999

Unlike the results with the average energy formalism (Figure 6), the average operator formalism yields results of similar quality to CASSCF and tLSDA (Figures 4 and 5).

Table 18: CI coefficients for CI-tLSDA results reported in Table 17.

CI-tLSDA state	CSF	CASSCF CI coeff.	CI-tLSDA CI coeff.
$1^1\Sigma^+$	$1\sigma^2$	0.979	0.985
	$1\sigma 2\sigma$	-0.204	0.173
$2^1\Sigma^+$	$1\sigma^2$	0.204	0.172
	$1\sigma 2\sigma$	0.979	-0.982

Table 19: Total energies of HeH^+ at 5 Å

state	CASSCF	tLSDA	CI-tLSDA
$1^1\Sigma^+$	-2.849	-2.849	-2.849
$2^1\Sigma^+$	-2.474	-2.440	-2.440

The ionic-covalent curve crossings of LiF with the average operator formalism are reported in Figure 12. The adiabatic curves are labeled by their electronic character at 9 Å. The CASSCF, tLSDA, and SI-tLSDA (with the average energy formalism) results are in Figures 7, 9, and 10, respectively.

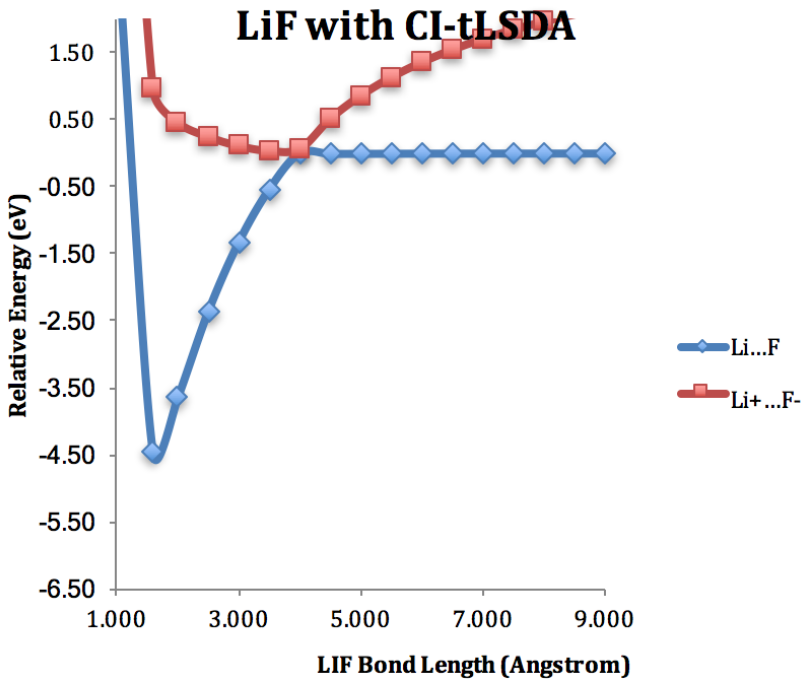

Figure 12: LiF potential curves with CI-tLSDA (average operator formalism).

The total energies of CASSCF, tLSDA, and CI-tLSDA and CI coefficients of CASSCF and CI-tLSDA at equilibrium are reported in Tables 21 and 22, respectively.

Table 20: CI coefficients for CI-tLSDA results reported in Table 19.

CI-tLSDA state	CSF	CASSCF CI coeff.	CI-tLSDA CI coeff.
$1^1\Sigma^+$	$1\sigma^2$	1.000	1.000
	$1\sigma 2\sigma$	0.000	0.000
$2^1\Sigma^+$	$1\sigma^2$	0.000	0.000
	$1\sigma 2\sigma$	1.000	1.000

The total energies of CASSCF, tLSDA, and CI-tLSDA and CI coefficients of CASSCF and CI-tLSDA at dissociation (9 Å) are reported in Tables 23 and 24 , respectively. The CSFs are labeled by their character at 9 Å.

Table 21: Total energies of LiF at equilibrium

state	CASSCF	tLSDA	CI-tLSDA
$1^1\Sigma^+$	-107.006	-106.854	-106.832
$2^1\Sigma^+$	-106.806	-106.628	-106.633

Table 22: CI coefficients for CI-tLSDA results reported in Table 21.

CI-tLSDA state	CSF	CASSCF CI coeff.	CI-tLSDA CI coeff.
$1^1\Sigma^+$	$2p^2_{\mathrm{F}(x)}2p^2_{\mathrm{F}(y)}2p^2_{\mathrm{F}(z)}$	-0.977	0.999
	$2s^1_{\mathrm{Li}}2p^2_{\mathrm{F}(x)}2p^2_{\mathrm{F}(y)}2p^1_{\mathrm{F}(z)}$	0.072	$<$0.05
$2^1\Sigma^+$	$2p^2_{\mathrm{F}(x)}2p^2_{\mathrm{F}(y)}2p^2_{\mathrm{F}(z)}$	0.069	$<$0.05
	$2s^1_{\mathrm{Li}}2p^2_{\mathrm{F}(x)}2p^2_{\mathrm{F}(y)}2p^1_{\mathrm{F}(z)}$	0.992	-0.999

The tLSDA curves are qualitatively correct except in the avoided crossing region (see Figure 9). In the avoided crossing region, tLSDA curves have an unphysical double crossing. The CI-tLSDA results (with the average energy formalism) better match the CASSCF results and do not exhibit the 50-50 mixture observed in the average energy minimization (Figure 10).

Table 23: Total energies of LiF at 9 Å

state	CASSCF	tLSDA	CI-tLSDA
$1^1\Sigma^+$	-106.851	-106.655	-106.668
$2^1\Sigma^+$	-106.773	-106.614	-106.589

Table 24: CI coefficients for CI-tLSDA results reported in Table 23.

CI-tLSDA state	CSF	CASSCF CI coeff.	CI-tLSDA CI coeff.
$1^1\Sigma^+$	$2p^2_{\mathrm{F}(x)}2p^2_{\mathrm{F}(y)}2p^2_{\mathrm{F}(z)}$	-0.001	<0.05
	$2s^1_{\mathrm{Li}}2p^2_{\mathrm{F}(x)}2p^2_{\mathrm{F}(y)}2p^1_{\mathrm{F}(z)}$	0.994	0.999
$2^1\Sigma^+$	$2p^2_{\mathrm{F}(x)}2p^2_{\mathrm{F}(y)}2p^2_{\mathrm{F}(z)}$	-0.977	0.999
	$2s^1_{\mathrm{Li}}2p^2_{\mathrm{F}(x)}2p^2_{\mathrm{F}(y)}2p^1_{\mathrm{F}(z)}$	-0.001	<0.05

4 Dipole-Quadrupole Diabatization

A review of property-based diabatization is shown in Section 4.1. Boys localized diabatization is covered in Sections 4.2, and the fourfold way is covered in Section 4.3. Dipole-Quadrupole diabatization is introduced in Section 4.4, and results are given in Sections 4.5.

4.1 Property-Based Diabatization Review

Many approaches to diabatization exist. In this section we review property-based diabatization. The following methods represent diabatic states as a linear combination of adiabatic states

$$\Phi_A = \sum_I^{N^{\text{st}}} \Psi_I T_{IA} \tag{67}$$

where Φ_A is a diabatic state, Ψ_I is an adiabatic state, T_{IA} is an element of the adiabatic-to-diabatic transformation matrix, and N^{st} is the number of adiabatic states, which is always assumed to be equivalent to the number of diabatic states.

We first discuss an older method by Werner and Meyer [76]. In this method, diabatic states (Φ) are defined as those that satisfy $\langle \Phi_A | \boldsymbol{\mu} | \Phi_B \rangle = 0$, which are interpreted as charge-localized states. Diagonalizing $\boldsymbol{\mu}$ fulfills this criterion, and the resulting transformation matrix is used to compute new diabatic states as in Equation 67. This method is straightforward and works for more than two states: an N^{st}xN^{st} dipole matrix needs to be diagonalized. When more than one component of the dipole is non-zero, one cannot diagonalize all components of the dipole vector with the same transformation. In such cases the Werner-Meyer method will not work or at least becomes ambiguous (as to which component is to be diagonalized), and this is a serious shortcoming for application to arbitrary geometries of polyatomic molecules, which prevents the method from being useful for calculating diabatic potential energy

surfaces in most cases.

Another method that may be considered to be a generalization of the Werner-Meyer method is the generalized Mulliken-Hush (GMH) method [77]. This method is similar to the Werner-Meyer method, but instead of diagonalizing the dipole operator along an axis, one diagonalizes $\boldsymbol{\mu} \cdot \boldsymbol{\nu}$, where

$$\boldsymbol{\nu} = \frac{\boldsymbol{\mu}_{II} - \boldsymbol{\mu}_{JJ}}{|\boldsymbol{\mu}_{II} - \boldsymbol{\mu}_{JJ}|} \tag{68}$$

for two states. This method reduces to Werner-Meyer when the direction of $\boldsymbol{\nu}$ is determined by symmetry but is an improvement over Werner-Meyer because one can now treat states that have more than one non-zero component for $\boldsymbol{\mu}$. The GMH method was developed for electron transfer, so rediagonalizing any sub-block of the Hamiltonian that corresponded to multiple diabatic states on the same charge center is recommended.

4.2 Review of Boys localized diabatization

Boys localization was originally developed for localizing orbitals [78, 79], and it was extended to the localization of many-electron states by Subotnik and coworkers [80]. This scheme defines the rotation matrix $\boldsymbol{T}$ of Equation 67 such that it maximizes the magnitude of the dipole moment difference between diabatic states

$$f_{\text{Boys}} = \sum_{A,B} \left| \langle \Phi_A \left| \boldsymbol{\mu} \right| \Phi_A \rangle - \langle \Phi_B \left| \boldsymbol{\mu} \right| \Phi_B \rangle \right|^2 . \tag{69}$$

This scheme is also equivalent to maximizing the dipole moment magnitude [81].

$$f_{\text{Boys}} = \sum_{A} \left| \langle \Phi_A \left| \boldsymbol{\mu} \right| \Phi_A \rangle \right|^2 . \tag{70}$$

Boys localized diabatization may be motivated by its appropriateness for treating electron transfer, for which it maximizes charge on the left in one state and charge on the right in the other state. However, Subotnik and coworkers showed that it is also applicable to more general problems [82–84]. The Boys localization scheme is only able to differentiate between electronic states of differing dipole moment. Thus, this method can have difficulty when there are more diabatic states than charge centers. For this reason, it was recommended to rediagonalize any sub-block of the Hamiltonian that corresponds to the same charge center [77, 80]. This is a complicating feature ; however, the method is still very convenient because it can be used with any electronic structure method and only uses the adiabatic dipole matrix without requiring orbital transformations.

4.3 Review of Fourfold Way

The fourfold way [85–88] is a general diabatization scheme (not a property-based scheme) based on configurational uniformity [89] and is currently available for transforming complete-active-space self-consistent field (CASSCF) [12] adiabatic states or multiconfiguration quasidegenerate perturbation theory (MC-QDPT) adiabatic states obtained with a CASSCF reference wave function [90]. This method will be used for benchmarking due to its previous success [91, 92].

To enforce configurational uniformity in the fourfold way, the adiabatic states need to be written as a linear combination of CSFs expressed in terms of diabatic molecular orbitals (DMOs), and one must choose diabatic prototype states; then the electronic states are transformed to have maximum resemblance to the diabatic prototype states. Thus there are two transformations involved, in particular an orbital transformation to yield DMOs and a CSF transformation to yield diabatic states.

The generation of DMOs is the key feature of the fourfold way method. The DMOs of the inactive and virtual orbitals are equivalent to the canonical MOs, and active

DMOs are obtained by rotating the active MOs to satisfy the threefold-density-matrix criterion and, if needed, the maximum-overlap-reference-MOs (MORMO) criterion, which is the fourth element.

The threefold-density-matrix criterion is satisfied by maximizing a three-term functional

$$D_3 = w_N D^{\mathrm{NO}} + w_R D^{\mathrm{ON}} + w_T D^{\mathrm{TD}} \tag{71}$$

which is a weighted sum of three functionals, where each w is a weight. The three terms are the state-averaged natural orbital term (D^{NO}), the sum of the squares of the orbital occupation numbers for all states (D^{ON}), and a term based on the transition density matrix (D^{TD}). If one generates DMOs from only the threefold-density criterion, the method is referred to as the threefold way.

The MORMO criterion in the fourfold way is also referred to as the reference-orbital overlap term, D^{RO}, and is it usually needed to resolve degeneracies, for example, in cases involving nonbonding p orbitals on the same center. If reference orbitals are needed, one must first choose λ reference DMOs as linear combinations of active orbitals at a reference geometry ($\boldsymbol{R}^{\mathrm{ref}}$), then determine the λ DMOs at any other geometry $\boldsymbol{R}$ by maximizing the reference-overlap term

$$D^{\mathrm{RO}} = \left| \sum_i \sum_j k_i \left(\boldsymbol{R}^{\mathrm{ref}}\right) k_j \left(\boldsymbol{R}\right) \left\langle \xi_i \left(\boldsymbol{R}\right) | \xi_j \left(\boldsymbol{R}\right) \right\rangle \right|^2 \tag{72}$$

where ξ is an atomic (contracted) basis function at the geometry $\boldsymbol{R}$, and k is an MO coefficient. The remaining DMOs are generated through the threefold-density-matrix criterion.

The main drawback of the fourfold way is that the proper choice of reference orbitals and the determination of prototype CSFs for the configurational uniformity step require system-dependent decisions that can be time-consuming and may require preliminary knowledge of the system.

4.4 Dipole-Quadrupole Diabatization Theory

In dipole-quadrupole diabatization (DQ) [81], the function to be maximized is

$$f_{\mathrm{DQ}} = \sum_{A} \left(\left| \langle \Phi_A \left| \boldsymbol{\mu} \right| \Phi_A \rangle \right|^2 + \sum_{j}^{N^Q} \alpha_j \left| \left\langle \Phi_A \left| Q^j \right| \Phi_A \right\rangle \right|^2 \right) \tag{73}$$

where α is a parameter (in atomic units, a_0^{-2}), Q is the primitive quadrupole (as opposed to the traceless quadrupole), N^Q is the number of quadrupole origins, and j denotes a choice of origin for the quadrupole integrals. The results of DQ are origin dependent if the dipole moment or charge is nonzero. This method maintains many of the desirable features of Boys localization and requires only the dipole-moment and quadrupole-moment matrices as input. Note that when all values of α are zero DQ reduces down to Boys localized diabatization (compare Equation 70 with Equation 73). The derivation can be found in Reference [81].

4.5 Applications of DQ Diabatization

4.5.1 Computational Details

The first three $^1\Sigma^+$ states and four $^1\Sigma^+$ states of LiH (3-state LiH and 4-state LiH,respectively) were investigated. The three adiabatic potential energy curves (V_j, for j = 1-3) were computed by state-averaged CASSCF [14] averaging over three states (SA(3)-CASSCF) for 3-state LiH and averaging over four states (SA(4)-CASSCF) for 4-state LiH with equal weights for each state and with the aug-cc-pVTZ [40] basis set. The wave function was constrained to have C_{2v} spatial symmetry, and calculations were done in the A_1 irreducible representation. The first two $^1\Sigma^+$ states of HCl were also investigated. We carried out SA(2)-CASSCF calculations for HCl with equal weights The wave function was constrained to have C_{2v} spatial symmetry, and calculations were done in the A_1 irreducible representation.

We applied the DQ diabatization method to a typical path for phenol photodissociation, and we compare the results to those obtained by the fourfold way. The planar ground-state minimum-energy structure of phenol was optimized with C_s symmetry by the CASSCF method using the aug-cc-pVTZ basis set as was done in a previous study [92]. The active space includes 12 active electrons and 11 active orbitals and is denoted as CAS(12,11); the active space consists of three π, three π^*, and one of each σ^*_{CO}, σ^*_{OH} and p_z orbitals (where the p_z orbital is a lone pair orbital on oxygen with the C-1, C-2, and C-3 atoms of the phenyl ring placed in the xy plane). The adiabatic PESs of the three states ($^1\pi\pi$, $^1\pi\pi^*$, and $^1\pi\sigma^*$) were calculated by using the state-averaged CASSCF method with the same weight for each of the three states; this is denoted as SA(3)-CASSCF(12,11). These calculations employed the jul-cc-pVDZ [35] basis set. Dr. Xuefei Xu performed all phenol calculations.

The active space for 3-state LiH consists of two electrons in five orbitals, which nominally correspond to $1s_{\mathrm{H}}$, $2s_{\mathrm{Li}}$ and $2p_{\mathrm{Li}}$; this active space is denoted as CAS(2,5). The active space of HCl has eight electrons in five orbitals, which nominally correspond to $1s_{\mathrm{H}}$, $3s_{\mathrm{Cl}}$, and $3p_{\mathrm{Cl}}$, and it is denoted as CAS(8,5). The active space of 4-state LiH has two electrons in nine orbitals, which nominally correspond to $1s_{\mathrm{H}}$, $2s_{\mathrm{Li}}$, $2p_{\mathrm{Li}}$, $3s_{\mathrm{Li}}$, $3p_{\mathrm{Li}}$; this active space is denoted as CAS(2,9). We carried out diabatization by the Boys method, by the DQ method with more than one choice of the parameter α, and by the fourfold way. The origin for the quadrupole moment of 3-state and 4-state LiH was taken as the Li atom because an origin on or close to the Li atom is needed upon dissociation since all electronic changes occur on the Li atom. The origin for the quadrupole moment of HCl was taken as the Cl atom for the same reason as LiH. The origin of the quadrupole moment for phenol is the center of nuclear mass of the phenoxyl subsystem of phenol. The choice of origin was made due to the delocalized nature of the orbitals on the phenoxyl subsystem.

In the fourfold way calculations of 3-state LiH, 4-state LiH, and HCl, the three-

fold density matrix criterion does not need the reference-orbital overlap term, so the threefold way for this system. The threefold-way diabatization was performed in the GAMESS [31] software package with the 2013 patch. There were only three dominant CSFs, and each constitutes its own diabatic prototype group for the configurational uniformity step. The fourfold way diabatization results of phenol were taken from [92].

The dipole matrices needed for Boys localization and the DQ method and the quadrupole matrices needed for the DQ method were computed with the RASSI module [93, 94] in a locally-modified version of Molcas 8.1 [75] was used.

4.5.2 Results

The first four $^1\Sigma^+$ states of LiH consist of two covalent states, one ionic state, and one Rydberg state. In 3-state LiH, the third state is a mixture of the covalent $2p_{\mathrm{Li}}$ and the Rydberg state. The ionic diabatic state has a $1s_{\mathrm{H}}^2$ valence configuration and will be denoted state I. The covalent states have the valence configurations $1s_{\mathrm{H}}2s_{\mathrm{Li}}$ (diabatic state S) and $1s_{\mathrm{H}}2p_{\mathrm{Li}}$ (diabatic state P), respectively. The Rydberg state has a configuration of $1s_{\mathrm{H}}3s_{\mathrm{Li}}$ (diabatic state R). Diabatic energies (U_i) of the threefold way can be found in Figure 13, of Boys localized diabatization can be found in Figure 14, and of DQ with $\alpha = 0.3\ a_0^{-2}$ can be found in Figure 15 (U_1 corresponds to the I state, U_2 to the S state, and U_3 to a mix of R and P state) [81]. The threefold way results in smooth diabats that nicely agree with the adiabats away from crossings as seen in Figure 13. Because of the excellent performance of the threefold way in this case, we use it as the reference for comparison. The Boys localized diabatization results in Figure 14 unacceptably mixes the S and P states at large Li-H distances and shows nonsmooth behavior at small Li-H distances. The DQ method with $\alpha = 10.0$ (assumed to be the limit of quadrupole only) dissociates LiH correctly but the curves are not smooth [81]. Figure 15 shows the best result for a fixed alpha ($\alpha = 0.3\ a_0^{-2}$), and the dissociation of 3-state LiH can be fixed for $R_{\mathrm{LiH}} > 4$ Å but at the

cost of making the curves less smooth at small Li-H distances.

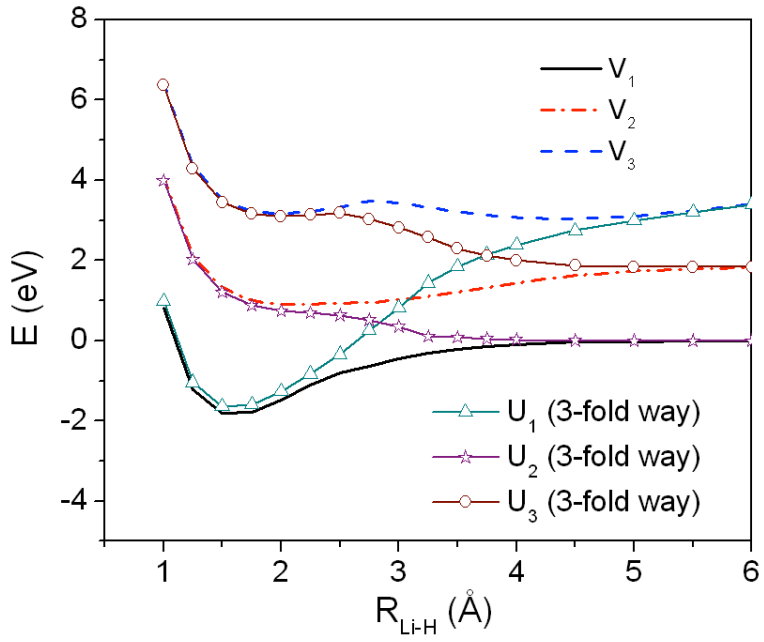

Figure 13: 3-state LiH potential curves with 3-fold way diabatization [81].

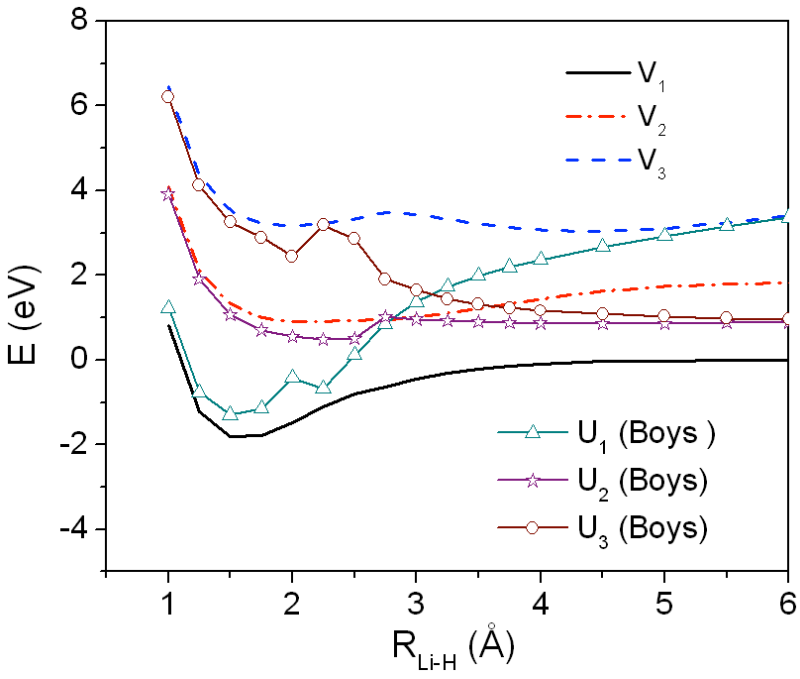

Figure 14: 3-state LiH potential curves with Boys localized diabatization [81].

The above analysis shows that there are two main deficiencies in Boys localized diabatization for LiH. The first is the incorrect dissociation of S and P. The second

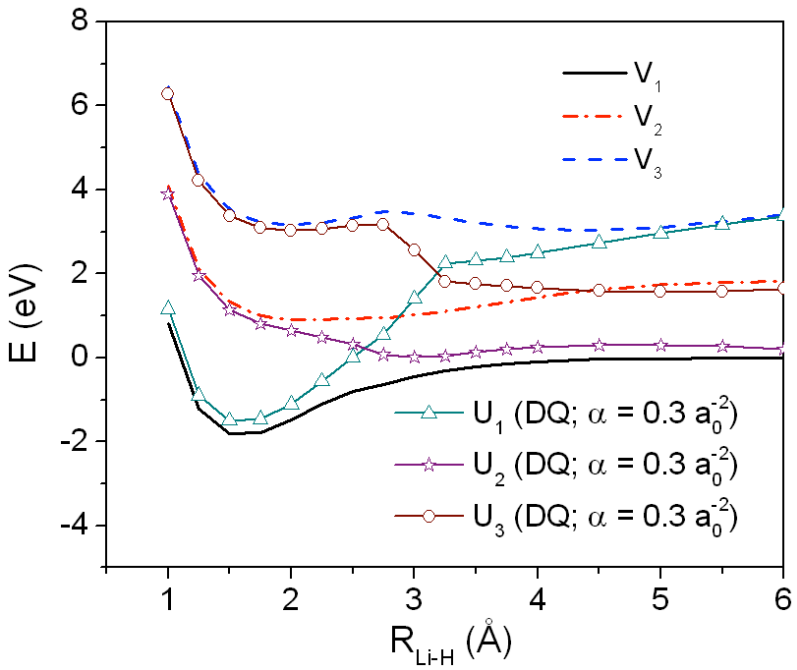

Figure 15: 3-state LiH potential curves with DQ diabatization, using an α value of 0.3. [81].

is the bump in at 2.0 Å. We conclude that the Boys localization, while suitable for two-state, two-center electron transfer problems and probably for some more general problems in special cases. The deficiencies of DQ for 3-state LiH will be elucidated in the discussion of 4-state LiH later in this section.

The squared diabatic couplings ($U_{jj'}$ where $j = 1$, 2, and 3 correspond respectively to the I, S, and P states of LiH) with (a) the threefold way (Figure 16), (b) Boys localized diabatization (Figure 17), and (c) the DQ method (Figure 18) are reported. There is no quantitative agreement between the three methods; however, there are similar trends. The Boys method does not yield well-behaved couplings, especially in the crossing regions, where the magnitudes are sporadic as shown in Figure 17. The large U_{12} and U_{23} couplings are due to the inability to separate states S and P at dissociation, which was shown in Figure 14. The results obtained with a value of α = 0.3 (Figure 18) with the threefold way (Figure 16) are similar. It is certainly not a general expectation that one can always expect the results to be good enough for

dynamics calculations, and in fact we expect that there will be cases where the more difficult fourfold way will still be required, but on the systems tested so far, the method has performed well. The disagreement in the couplings at small internuclear distances is not considered serious because couplings are mainly important for dynamics in regions close to where the two diabatic states cross; states S and P do not cross. One point to keep in mind here, though, is that variability in coupling in regions where the states are not strongly coupled is not completely unexpected. When the gap between states is large, the results are not sensitive to the precise magnitude of the coupling. This means that the inverse problem of determining the coupling is becoming ill-conditioned, i.e., the couplings are less well determined in the regions where they do not have a large effect.

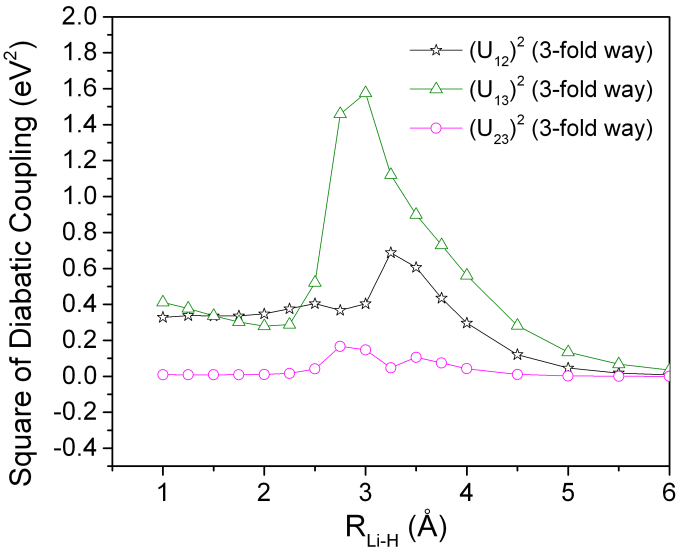

Figure 16: 3-state LiH squared diabatic couplings with 3-fold way diabatization [81].

In Figure 19, we report 4-state LiH diabats computed with the threefold way. The crossing of the R and P diabatic states between 2-3 Å, the crossing of the I and covalent S diabatic states between 3-3.5 Å, and the crossing of the I and covalent P diabatic states between 4.5-5 Å are all smooth. In addition, the diabats match the

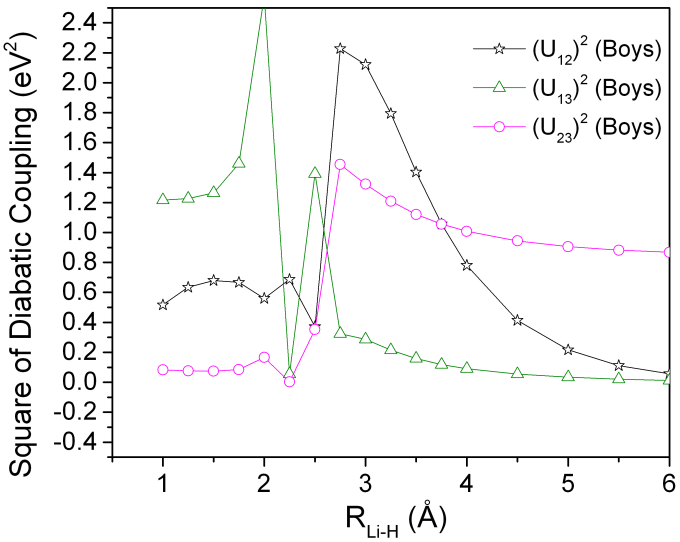

Figure 17: 3-state LiH squared diabatic couplings with Boys localized diabatization [81].

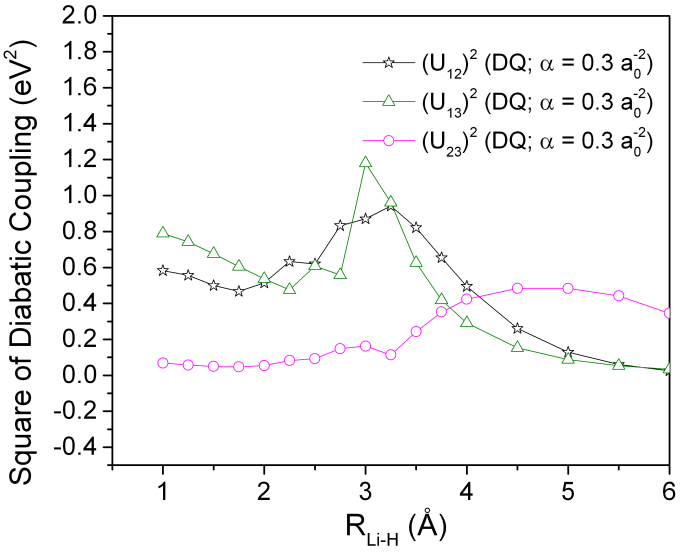

Figure 18: 3-state LiH squared diabatic couplings with DQ diabatization, using an α value of 0.3. [81].

adiabats away from crossings. We use the threefold way as reference again because it usually provides an accurate description of diabats.

Due to the poor behavior of Boys localized diabatization for 3-state LiH (see

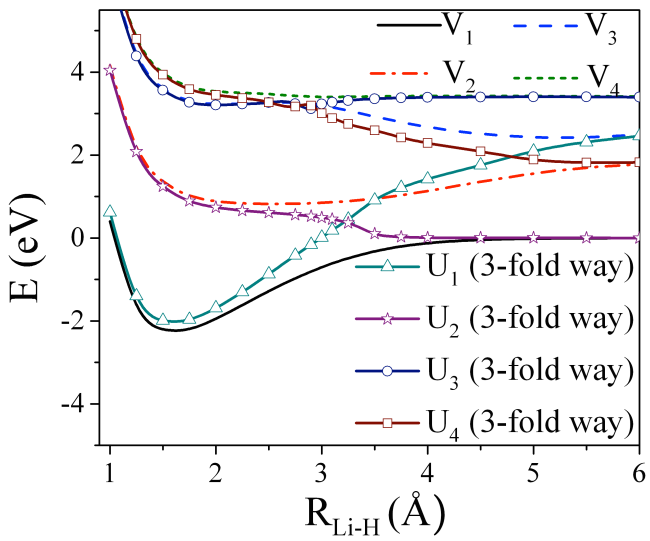

Figure 19: 4-state LiH potential curves with 3-fold way diabatization [95].

Figure 14), we do not apply it to 4-state LiH. We computed diabatic potential-energy curves for 4-state LiH with various values of α for DQ as shown in Figure 20. All three α values provide smooth crossings of the R and P diabatic states in the 2-3 Å range. This is not surprising since Rydberg states tend to have large values of quadrupole, which can be easily distinguished from the other states. In addition, the crossings of the I and P diabatic states between 4.5 and 5 Å are smooth for the three α values tested. The crossing between the I and S diabatic states between 2 and 3 Å does show some sensitivity to the α value, and the crossing appears much too abrupt with $\alpha = 1.0\ a_0^{-2}$. It is interesting to note that the crossings are shifted to slightly larger as α increases, in better agreement with the threefold way, and the I and P diabatic state crossings are more strongly coupled by the DQ method than by the threefold way. For the three values of α shown in Figure 20, the DQ method produces satisfactory results. It is clear now, that DQ diabatization had difficulties at near equilibrium due to the change of character of the third state. By including the 4th state, a constant value of α provides satisfactory results.

The squared diabatic couplings of 4-state LiH for the threefold way are reported

in Figures 21 and 22. The squared couplings between the covalent states ($(U_{23})^2$, $(U_{24})^2$, and $(U_{34})^2$) are very small. The coupling between the ionic I and covalent S diabatic states $(U_{12})^2$) in Figure 21 is constant until 3.75 Å, which is the region soon after the I and S diabatic state crossing in Figure 20.

The squared diabatic couplings with the DQ method can be found in Figure 23 for $\alpha = 0.5\ a_0^{-2}$, Figure 24 for $\alpha = 1.0\ a_0^{-2}$, and Figure 25 for $\alpha = 10.0\ a_0^{-2}$. There is little qualitative difference in the squared diabatic coupling between these figures, so we will only discuss Figure 25. The very large peak in $(U_{12})^2$ in Figure 25(a) correlates very well with the I and S state crossing in Figure 20. The peak in $(U_{14})^2$ in Figure 25(b) also occurs at the same location as the crossing of the I and P diabatic states in Figure 20.

The comparison of our three-state and four-state treatments of LiH illustrates an important general point. For general polyatomics there is no symmetry, and the first adiabatic state somewhere intersects the second, the second intersects the third, the third intersects the fourth, and so forth. On one side of that third state-fourth state intersection, the third adiabatic state may be dominated, for example, by the third diabat, and on the other side it is dominated by the fourth diabat. Thus an accurate global treatment of the three lowest adiabats requires four diabats.

The first two $^1\Sigma_1$ states of HCl provide a prototypical example of an ionic-covalent curve crossing [96]. This ionic-covalent curve crossing provides a case where Boys diabatization is expected to work well. The ionic diabatic state has a $3s^2_{\mathrm{Cl}}3p^6_{\mathrm{Cl}}$ valence configuration and the covalent state has the valence configuration $1s^1_{\mathrm{H}}3s^2_{\mathrm{Cl}}3p^5_{\mathrm{Cl}}$.

Figure 26 reports the adiabatic (V_i) and diabatic (U_i) potential energy curves obtained with (a) the threefold way and (b) Boys localization for the two lowest-energy $^1\Sigma^+$ states of HCl (U_1 corresponds to the ionic state and U_2 to the covalent state). The threefold way results in smooth diabats that agree well with the adiabats away from crossings as seen in Figure 26(a). Therefore, we use the threefold way result

as a reference. The Boys localized diabatization curve in Figure 26(b) is reasonable; however, the diabats at small R_{HCl} do not match the adiabats well.

In Figure 27, we show the DQ diabats with (a) $\alpha = 0.5\ a_0^{-2}$, (b) $\alpha = 1.0\ a_0^{-2}$, and (c) $\alpha = 10.0\ a_0^{-2}$ for the two lowest-energy $^1\Sigma^+$ states of HCl. The DQ method with any of these three values of α produces reasonable diabats. For all three values, the diabats agree with the adiabats at small R_{HCl} better than was observed in the Boys calculations (Figure 26(b)).

We can summarize what we learned from these tests as follows: for an ionic-covalent curve crossing, it was not previously clear if (i) addition of the quadrupole would deteriorate the results since we assumed that the Boys localized diabatization should already be satisfactory and (ii) if the diabatization would be significantly α-dependent. Inspection of Figure 26(b) and Figure 27 shows that addition of the quadrupole improves the matching between diabats and adiabats at small R_{HCl}. Figure 27(c) shows that good diabats are obtained even when the diabatization is dominated by the quadrupole, $\alpha = 10.0\ a_0^{-2}$. As for the α-dependence, there is essentially no difference between $\alpha = 0.5$, 1.0, and 10.0 a_0^{-2}.

Figure 28 shows the square of the diabatic couplings (U_{12}) with (a) the 3-fold way and (b) the Boys localization method, and Figure 29 shows these for the DQ method with $\alpha = 0.5\ a_0^{-2}$, 1.0 a_0^{-2}, and 10.0 a_0^{-2}. The threefold way coupling in Figure 28(a) is in qualitative agreement with the DQ results in Figure 29 for all three nonzero values of α, and the peak position corresponds to the crossing in Figure 27. The qualitative behavior of Boys localized diabatization in Figure 28(b) is similar to those of Figure 29; however, there is a larger coupling than the other methods at small R_{HCl} (e.g., 1.0 Å), which correlates with the larger adiabat-diabat separation in the potential curves at the same distance in Figure 26(b).

Photodissociation of phenol to phenoxyl radical and hydrogen atom is a nonadiabatic process in which the crossings of potential energy surfaces (PESs) of three states

[$^1\pi\pi$ (S_0), $^1\pi\pi^*$ (S_1), and $^1\pi\sigma^*$ (S_2)] along the O-H fission coordinate play important roles [97]. Figures 30 and 31 present results as functions of the O-H distance, $R_{\text{O-H}}$, with the C-C-O-H torsion angle equal to 30° and the other internal coordinates fixed at their values at the planar ground-state equilibrium geometry. The diabatic and adiabatic PESs (U_j and V_j, respectively, for j = 1-3) are shown in Figure 30, and the squares of the diabatic couplings ($U_{jj'}$) are in Figure 31. For O-H distances shorter than 1.44 Å, the three diabatic surfaces have the following character: U_1 is $^1\pi\pi^*$, U_2 is $^1\pi\pi^*$, and U_3 is $^1\pi\sigma^*$; however, at R_{O-H} = 1.44 Å, due to another crossing with a higher energy $^1\pi\sigma^*$ state. Figure 30 shows that the diabatic PESs obtained by the DQ method with $\alpha = 10\ a_0^{-2}$ agree very well with those obtained by the fourfold way. Figure 31 shows that the DQ method always overestimates the couplings compared to fourfold way, especially for $R_{\text{O-H}} < 1.50$ Å, where the DQ U_{12} and U_{13} couplings are significantly larger than the fourfold way ones, but we should keep in mind that the diabatic couplings are significant for the dynamics mainly when the surfaces are strongly interacting.

For $R_{\text{O-H}} < 1.50$ Å, the U_1 and U_2 surfaces are well separated, as are the U_1 and U_3 surfaces, and the overestimations of U_{12} and U_{13} couplings may have little influence on the dynamics simulations. The U_{13} couplings obtained by two methods agree well in the strong interaction region ($R_{\text{O-H}}$ = 1.70 - 2.20 Å) of the U_1 and U_3 surfaces. The U_{23} couplings obtained by DQ method are about twice as large as those in the fourfold way around the crossing region ($R_{\text{O-H}}$ = 1.10 - 1.30 Å) of the U_2 and U_3 curves, but they have similar trends, and the values are still reasonable. Therefore, the results presented here indicate that the DQ method with $\alpha = 10\ a_0^{-2}$ provides a suitable diabatization method for simulating the photodissociation of phenol.

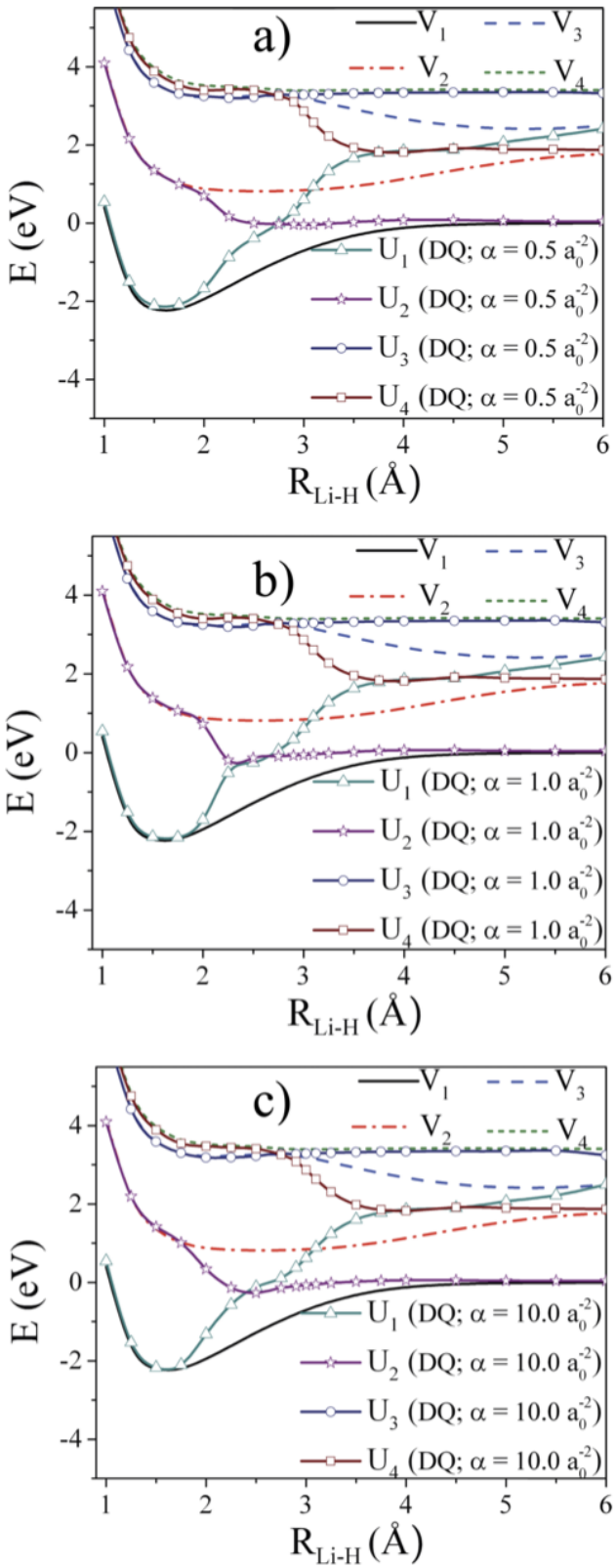

Figure 20: 4-state LiH potential curves with DQ diabatization with an α value of (a) 0.5 a_0^{-2}, (b) 1.0 a_0^{-2}, and (c) 10.0 a_0^{-2} [95].

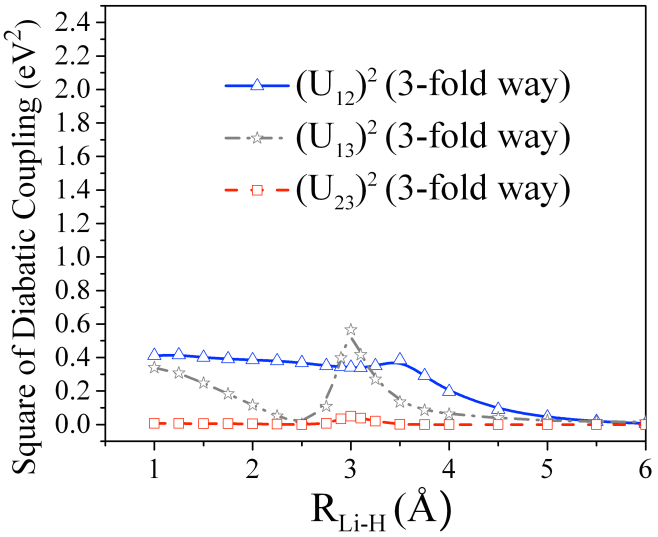

Figure 21: 4-state LiH squared diabatic couplings with 3-fold way diabatization [95].

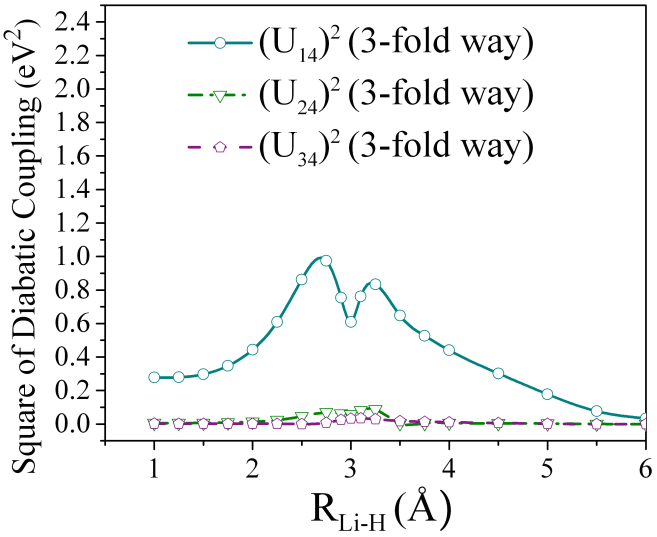

Figure 22: 4-state LiH squared diabatic couplings (cont.) with 3-fold way diabatization [95].

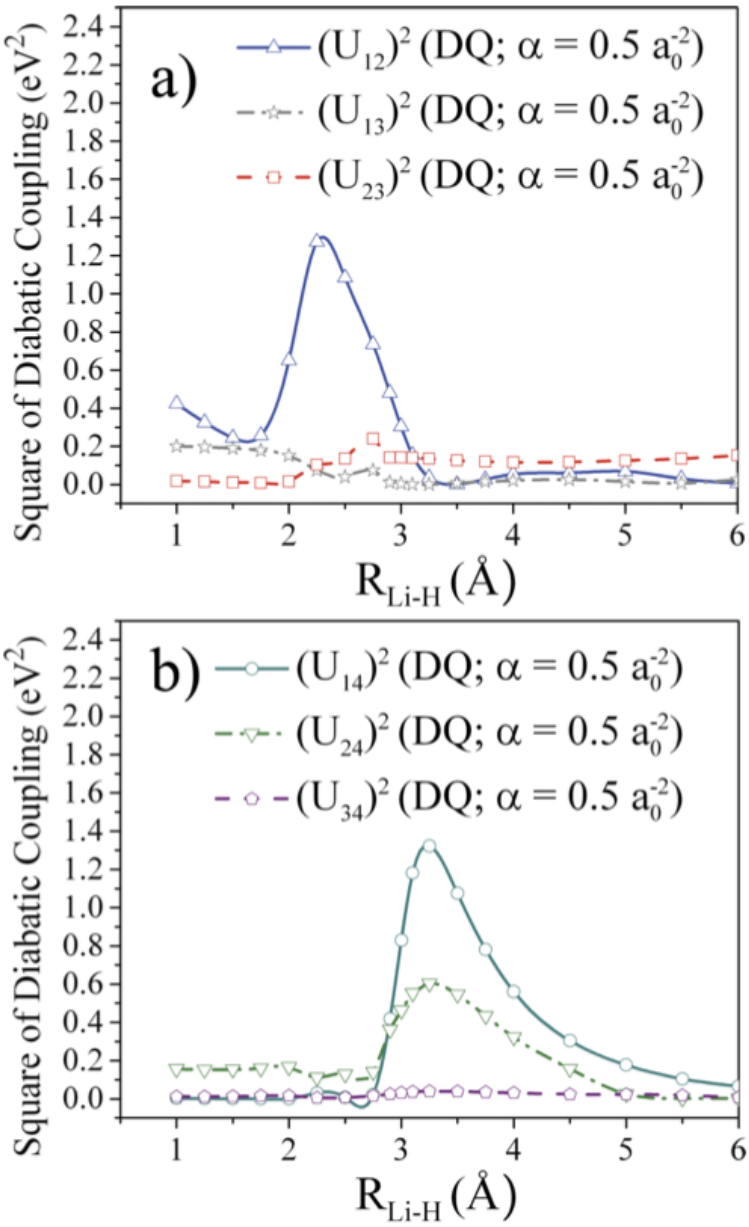

Figure 23: 4-state LiH squared diabatic couplings with an α value of 0.5 a_0^{-2} for DQ diabatization [95].

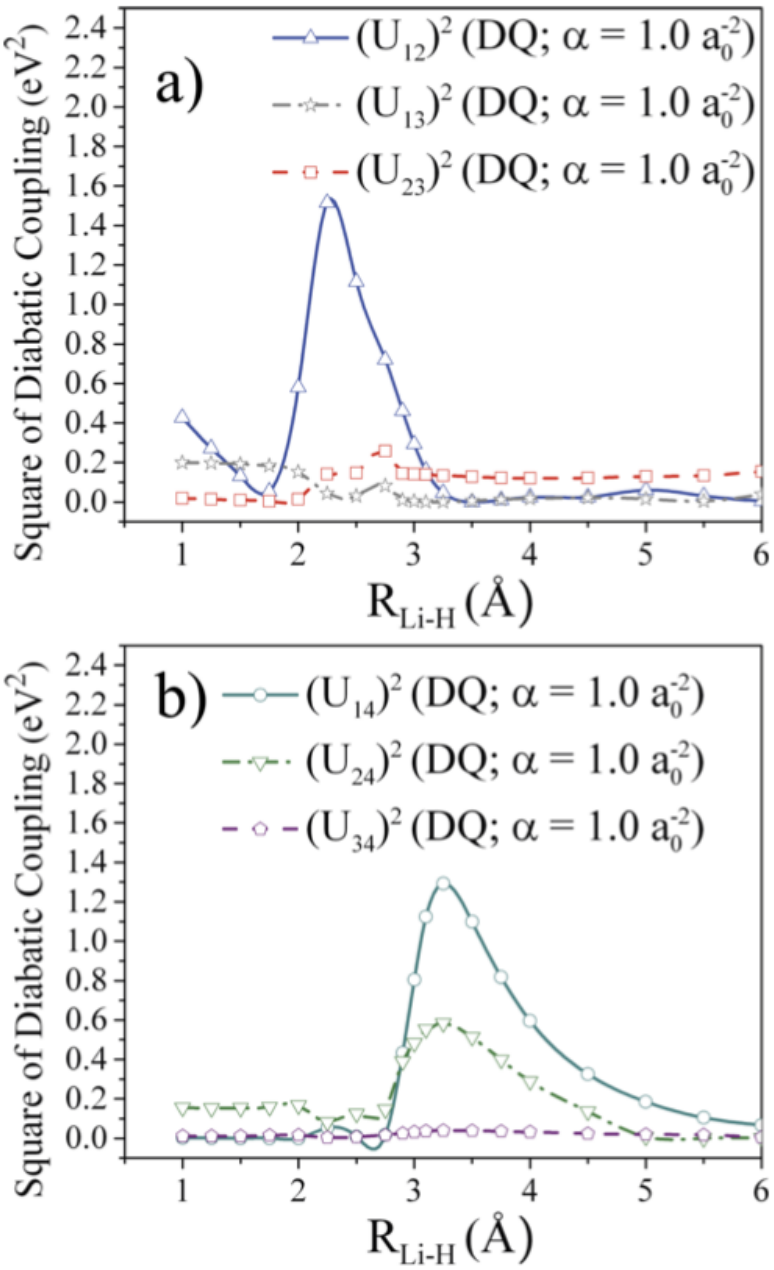

Figure 24: 4-state LiH squared diabatic couplings with an α value of 1.0 a_0^{-2} for DQ diabatization [95].

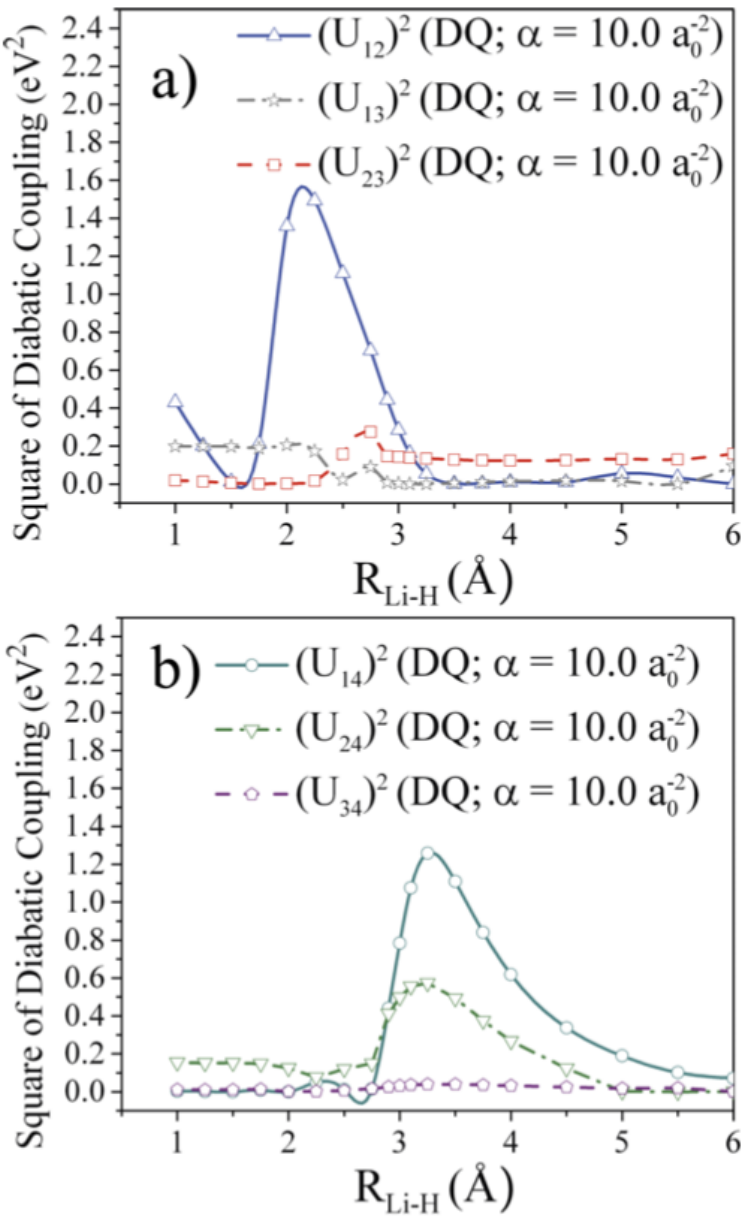

Figure 25: 4-state LiH squared diabatic couplings with an α value of 10.0 a_0^{-2} for DQ diabatization [95].

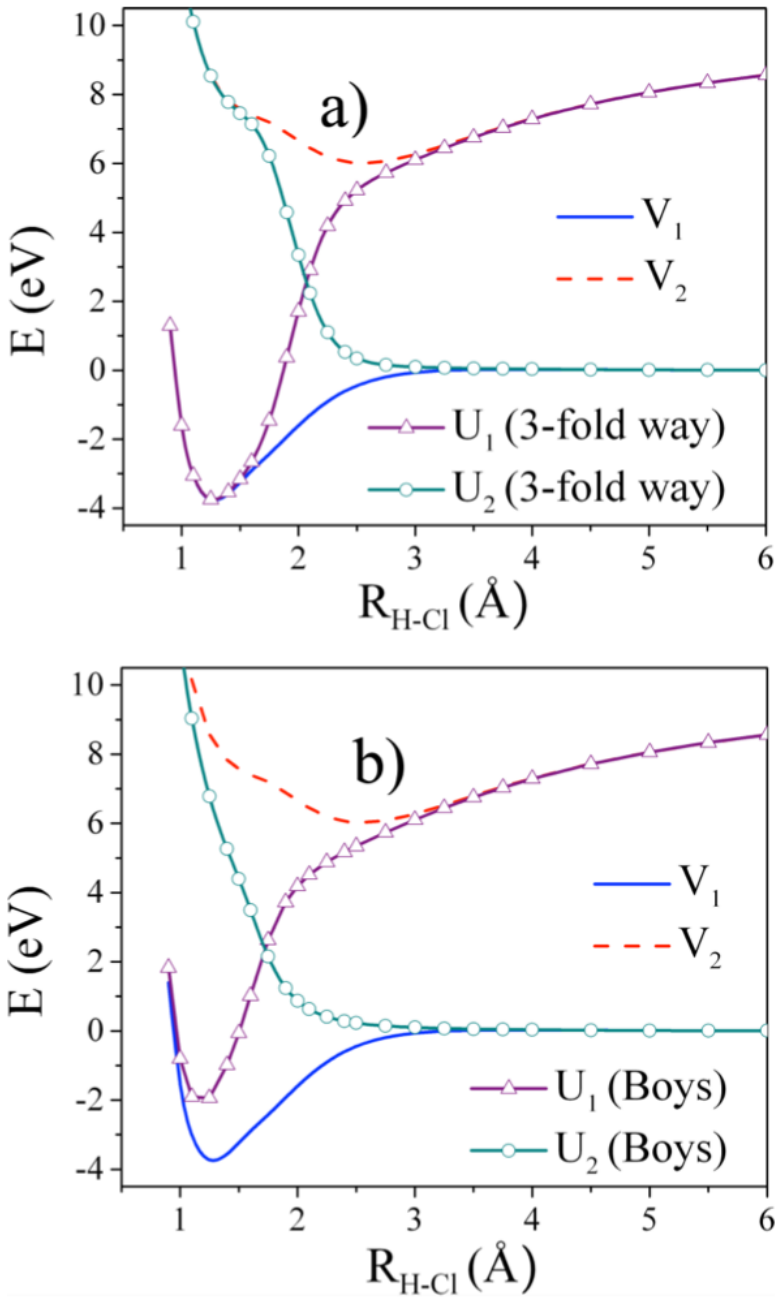

Figure 26: HCl potential curves with (a) 3-fold way diabatization and (b) Boys localized diabatization [95].

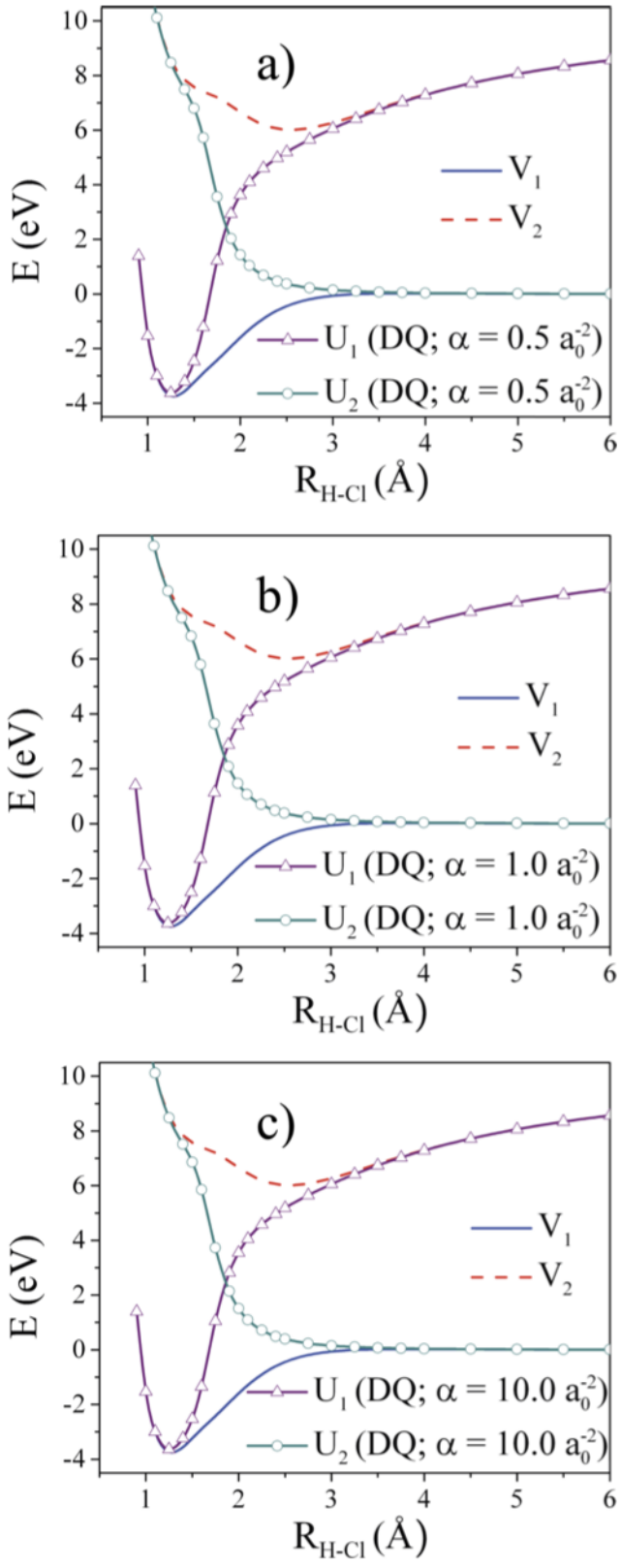

Figure 27: HCl potential curves with DQ diabatization for (a) $\alpha = 0.5\ a_0^{-2}$, (b) $\alpha = 1.0\ a_0^{-2}$, and (c) $\alpha = 10.0\ a_0^{-2}$ [95].

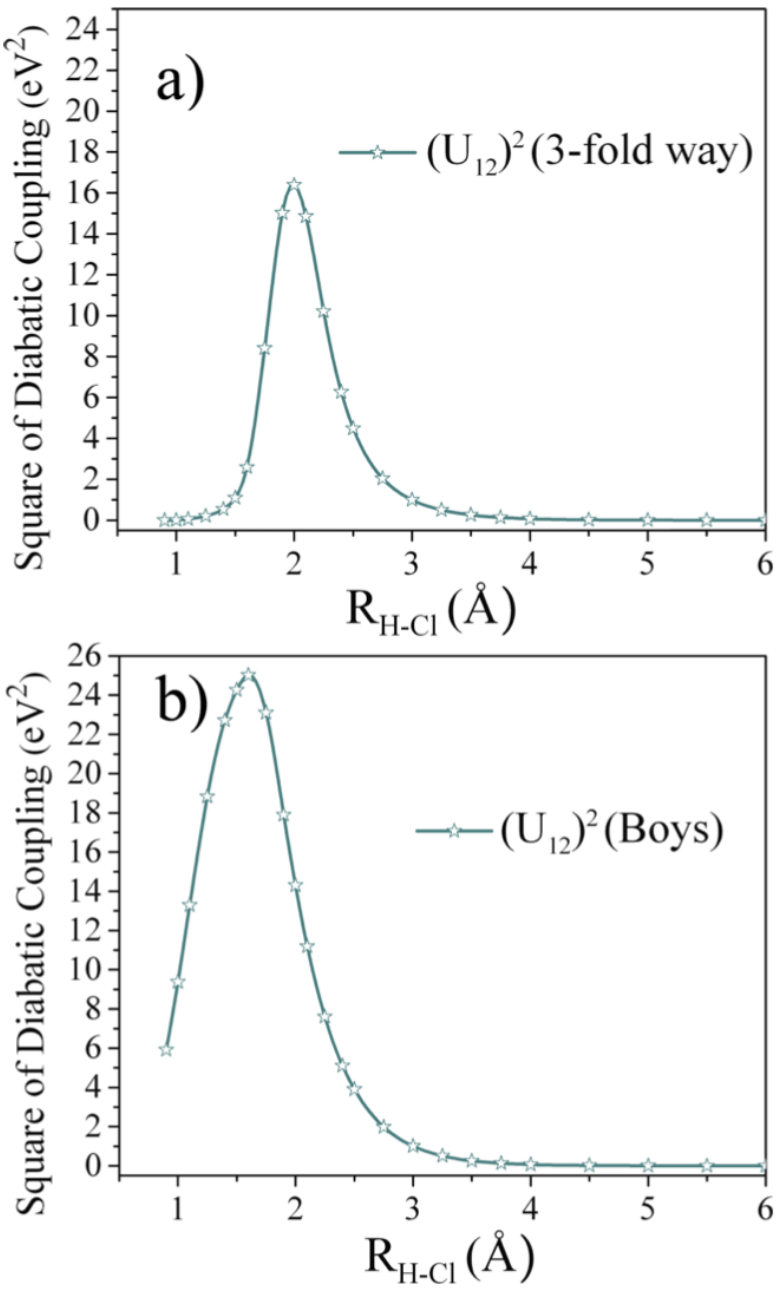

Figure 28: HCl squared diabatic couplings with (a) 3-fold way diabatization and (b) Boys localized diabatization [95].

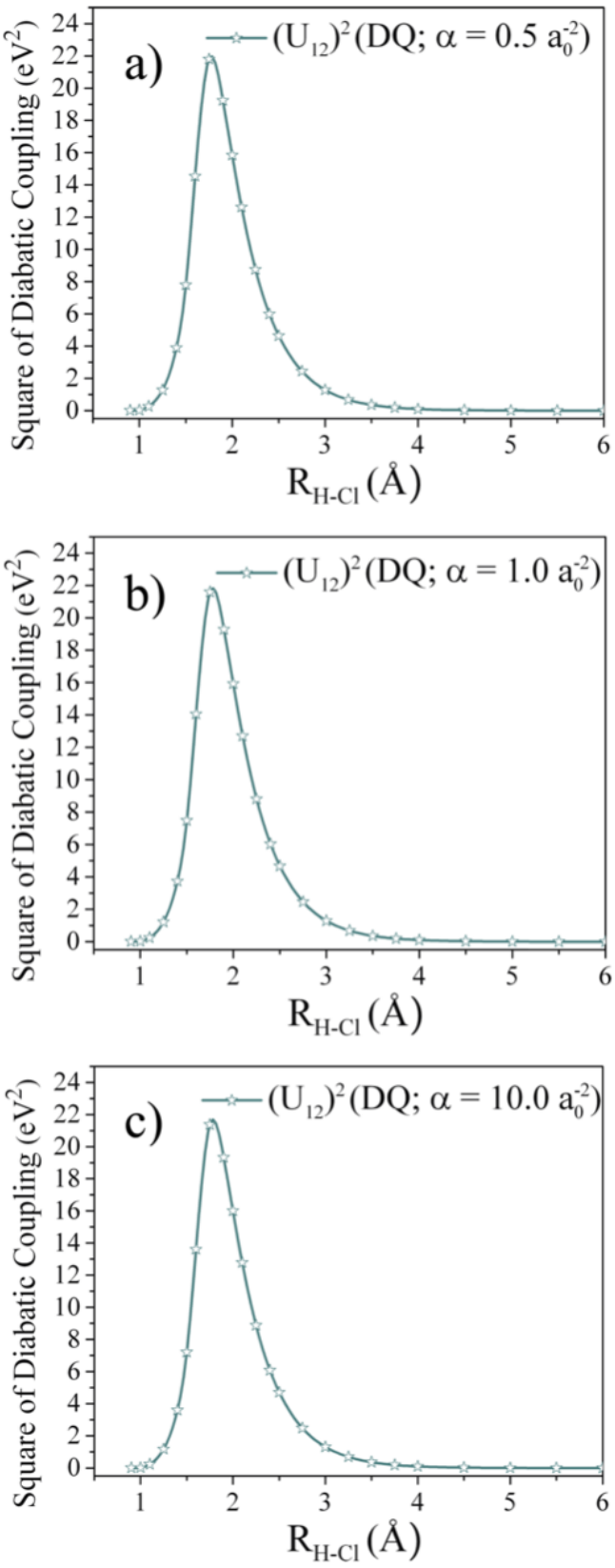

Figure 29: HCl squared diabatic couplings with DQ diabatization for (a) $\alpha = 0.5\ a_0^{-2}$, (b) $\alpha = 1.0\ a_0^{-2}$, and (c) $\alpha = 10.0\ a_0^{-2}$ [95].

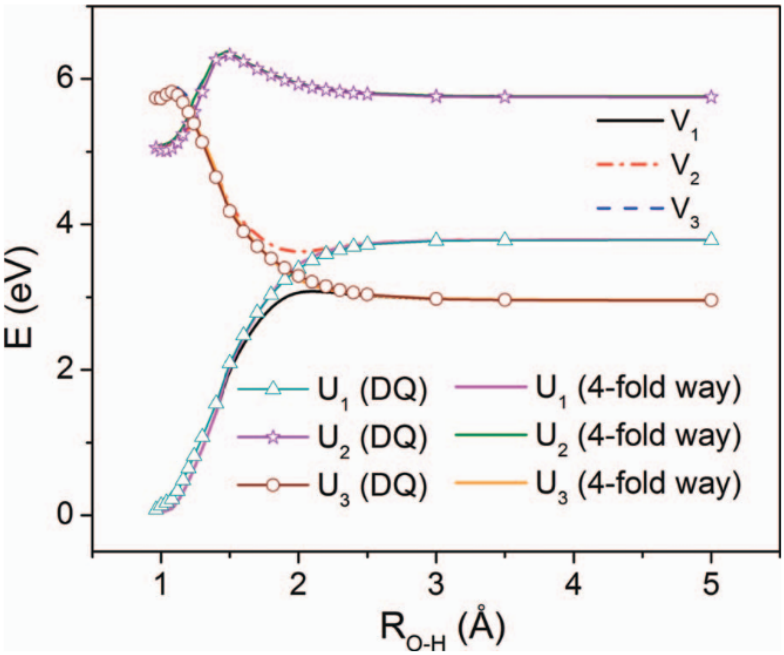

Figure 30: Phenol potential curves with 4-fold way diabatization and DQ with $\alpha = 10\ a_0^{-2}$ [81].

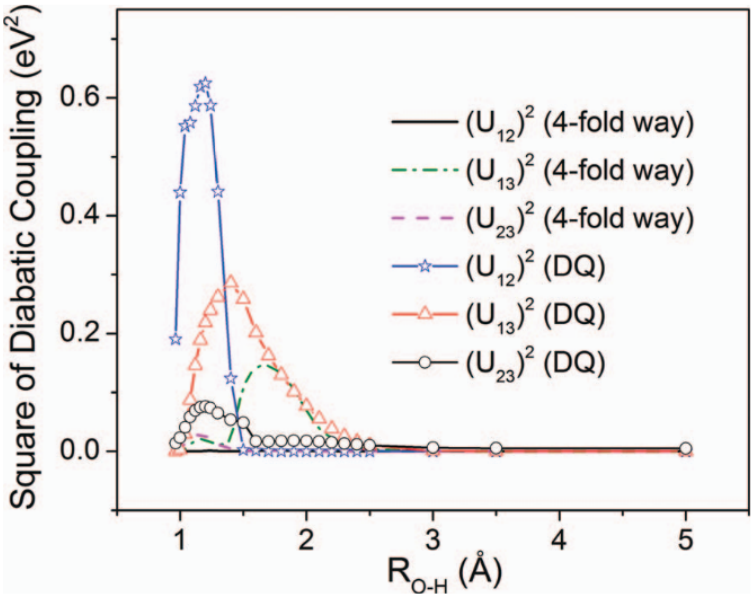

Figure 31: Phenol squared diabatic couplings with 4-fold way diabatization and DQ with $\alpha = 10\ a_0^{-2}$ [81].

5 Dipole-Quadrupole-Electrostatic Potential (DQΦ) Diabatization

In Section 5.1, the theory of dipole-quadrupole-electrostatic-potential (DQΦ) diabatization is introduced. DQΦ diabatization computational details and results are covered in Sections 5.2 and 5.3, respectively. In Section 5.4, a weighted form of DQΦ diabatization is introduced.

5.1 Dipole-Quadrupole-Electrostatic-Potential Diabatization Theory

Dipole-quadrupole (DQ) diabatization was extended to also include the electronic electrostatic potential (i.e., the electrostatic potential due to the electrons), and the method is referred to as dipole-quadrupole-electrostatic-potential (DQΦ) diabatization [95]. The function that is maximized in DQΦ diabatization is the DQ function in Equation 73 plus an additional summation for the electrostatic potential

$$f_{\mathrm{DQ\Phi}} = \sum_{A} \left(\left| \langle \Phi_A \left| \boldsymbol{\mu} \right| \Phi_A \rangle \right|^2 + \sum_{j}^{N^Q} \alpha_j \left| \left\langle \Phi_A \left| Q^j \right| \Phi_A \right\rangle \right|^2 + \sum_{k}^{N^\Phi} \beta_k \left| \left\langle \Phi_A \left| \Phi^k \right| \Phi_A \right\rangle \right|^2 \right) \tag{74}$$

where N^Φ is the number of origins for the electrostatic potential, k denotes a choice of origin for the electrostatic potential, and β_k is a parameter that weights the importance of the electrostatic potential in the diabatization. When k equals 1, we simply call the parameter β. When all β_k are zero, the method reduces to DQ diabatization. When all α_j are zero, the method is referred to as DΦ diabatization.

5.2 Computational Details

For the $(H_2)_2$ system, adiabatic potential energy curves for the first two $^1\Sigma^+$ excited states, were computed by SA(N)-CASSCF with equal weights for each state and with the TZP basis set [98] in Molpro 2012.1 [99, 100]. The active space was 4 electrons in 4 orbitals corresponding to the 1s orbital on each H.

For the Li + FH $\rightarrow$ LiF + H system, the change along a reaction coordinate, s, was defined by

$$\Delta s = \sqrt{\sum_{i=\mathrm{Li,F,H}} (\Delta x_i^2 + \Delta y_i^2 + \Delta z_i^2)} \tag{75}$$

where the summation is over the change in the mass-weighted Cartesian coordinates for the three atoms with the origin of s at the saddle point of the lower adiabatic curve. The reactant side was defined by stretching the LiF bond while optimizing the FH bond distance. The product side was defined by stretching the FH bond while optimizing the LiF bond distance. The bond angle was held at 120° for all calculations. The geometries were taken from previous calculations that were performed for the fourfold way diabatization method [101]. The adiabatic ground state (11A′) and first excited state (21A′) were calculated with SA(2)-CASSCF in Molpro 2012.1 [99, 100] with the 6-311G++(3df,3pd) basis set augmented by additional diffuse s and p functionals with exponents 0.0052(s) and 0.0097(p) for Li, 0.089(s), 0.083(p) and 0.000 01(s) for F, and 0.037(s), 0.012(s), and 0.055(p) for H. [85, 101–103] The active space was made up of 7 electrons distributed in eight orbitals for the 2s and 2p orbitals of Li, the 2p orbitals of F, and the 1s orbital of H.

We performed diabatization with Boys localized diabatization, the DQ method, and the DΦ method. Quadrupole and electrostatic potential origins were put on each atom, except in the case of the LiFH system where calculations were performed with only one quadrupole origin, which was on the Li atom. For all results shown in the paper, the α values were 10 a_0^{-2}, and the β values were 1 a_0^4. The $(H_2)_2$ and LiFH

calculations were performed by Kelsey Parker. The dipole and quadrupole matrices were computed with the TRANS and MATROP modules of Molpro version 2012.1 [99, 100]. The electrostatic potential matrices were computed with the MATROP module of Molpro version 2012.1. Diabatization was performed with DQΦpac [104].

5.3 Results

In this section, we report our findings for Boys localized, DQ, and DΦ diabatization for H_2 dimer, and we compare the results to previously calculated [85] fourfold way results. The two hydrogen molecules are collinear with the centers of mass of the molecules always separated by 10 a_0. One molecule is referred to as A and the other as B. Molecule A has a bond length of r - Δr, and B has a bond length of $r + \Delta r$ where r is 1.5 a_0 and Δr ranges from -0.2 to 0.2. The first two $^1\Sigma^+$ excited states of $(H_2)_2$ show an avoided crossing due to the symmetry of the reaction coordinate. The first adiabatic excited state corresponds to excitation of a σ MO to a σ^* MO on the compressed molecule. The second adiabatic excited state is a σ-to-σ^* excitation of the stretched molecule. The roles of the molecules A and B change over the Δr reaction coordinate, which results in the avoided crossing of the adiabatic states, which are labeled V_2 and V_3 in Figure 32.

Previously, the threefold way was successful for diabatization with DMOs localized on molecules A and B [85]. The threefold way results meet our criteria of good diabatic curves by being smooth and matching the adiabatic curves away from crossings. Figure 32 shows the results from Boys localized, DQ, and DΦ diabatization. For the DQ method, each H was used as an origin and all α_j values are 10 a_0^{-2}. For the DΦ method, each H was used as an origin and all β_k values are 1 a_0^4. Results from the Boys localized method are shown in Figure 32(a). The diabatic curves cross at zero as expected, but away from the avoided crossing, the diabatic curves diverge from the adiabatic curves. Addition of the quadrupole or electrostatic potential changes this

behavior, as shown in Figures 32(b) and 32(c), respectively. The diabatic curves now more closely resemble the adiabatic curves in regions further away from the avoided crossing. Both DQ and DΦ results show an improvement over using the dipole alone.

The squared diabatic couplings for the three methods are shown in Figure 33. The Boys results, shown in Figure 33(a), have a minimum at $\Delta r = 0$ and increase as the magnitude of Δr increases. The shape of the coupling curve agrees with the finding that the diabatic curves diverge from the adiabatic curves away from the avoided crossing. The DQ and DΦ plots, Figures 33(b) and 33(c), respectively, are approximately an order of magnitude smaller in scale. These plots show a peak at the avoided crossing of the adiabatic curves, $\Delta r = 0$. The curves decrease as the magnitude of Δr increases. The diabatic coupling calculated with the DΦ method continuously decreases while the DQ results show a slight increase as Δr approaches -0.2 and 0.2 a_0. Although Figures 33(b) and 33(c) look different, we should keep in mind that the diabatic coupling is mainly important in regions where it is comparable to the gap between the adiabatic states. For this problem, that occurs only very close to Δr equals zero. Very close to Δr equals zero, the figure shows that the two sets of diabatic couplings are comparable, both being about the square root of 0.008 eV^2.

The Boys localized diabatization method is not as satisfactory as DQ or DΦ for diabatization of the $(H_2)_2$ system. The addition of the electrostatic potential, like the addition of the quadrupole, shows an improvement in differentiating diabatic states in this case.

The LiFH system involves a reaction: $Li(^2S, ^2P) + FH \rightarrow LiF + H$. In the reactant region, the two lowest adiabatic potential energy surfaces ($11A'$, $21A'$) correspond to Li being in S and P states, respectively. In the products region, the ground state has a singly occupied H($1s$) orbital and the high energy first excited state shows electron donation from an in-plane lone pair on F to the H atom. Previous results of the fourfold way show diabatization was possible with this method by using a reference

orbital [85, 101] In order to obtain diabats that smoothly change from the reactant region to the product region, it was necessary to identify and choose appropriate reactant and product CSF groups as diabatic prototypes.

Figure 34(a) shows Boys localized results for LiFH. The $2^1A'$ curve is off-scale in the product region due to its very high energy. In the product region, the Boys localized diabatization results do differentiate between the diabatic states, but Boys diabatization fails in the reactant region, where it cannot differentiate the S and P states of the ground and first excited state of Li. These results are similar to what we saw for the diatomic hydrides where the addition of the quadrupole was found to improve the diabatization. Figure 34(b) shows the results from using the quadrupole with an origin on the Li atom and an α value of 10 a_0^{-2}. The reactant region now shows diabatic curves that approach the adiabatic curves, similar to fourfold way results.

Adding the electrostatic potential to the DQ method to give the DQ method shows a slight smoothing of the diabatic curves around $s = 0$ as shown in Figure 34(c). For these calculations, the quadrupole parameters are the same as for the previously described DQ calculations and the electrostatic potential parameters are: an origin on each atom and each β_j value set equal to 1 a_0^4. Taking out the quadrupole to give DΦ diabats was found to be unsuccessful in a similar way to the failure of the Boys localized calculations.

Figure 35 shows the square of the diabatic coupling for the three methods, a) Boys localized, b) DQ, and c) DQΦ. Boys localized results are shown in Figure 35(a). In the reactant region, the coupling is large. The DQ and DQΦ results are shown in Figure 35(b) and 35(c), respectively. The plots are essentially identical as the difference between the results for this system are slight. Near $s = 0.4$ amu$^{1/2}$a$_0$, the plots show a peak and as the magnitude of s increases, the square of the diabatic coupling decreases.

In summary, similarly to what was shown for the diatomic hydrides, the DQ method worked with an origin on Li and an α value of 10 a_0^{-2}. The addition of the electrostatic potential in the DQΦ method improved the smoothness. The diabatic curves are similar to the fourfold way curves [85], but the DQ method does not require a reference orbital or a prototype CSF list.

5.4 Energy Threshold Weighting

In addition a weighted version of DQΦ diabatization that is analogous to the weighted versions for the diabatization of Werner and Meyer [76] and Boys [105] and uses the same weighting function as in Ref. [105]. In weighted DQΦ [104] the off-diagonal elements of each adiabatic property are multiplied by a weighting function

$$W_{IJ} \left\langle \Psi_I \left| \hat{O} \right| \Psi_J \right\rangle \tag{76}$$

where W is a weighting function, $\hat{O}$ is a property operator, and Ψ is an adiabatic wavefunction. Then, $f_{\mathrm{DQ}\Phi}$ (Equation 74 is maximized as normal using the weighted adiabatic properties.

One choice of weighting function for weighted DQΦ is the one used in Ref. [105]

$$W_{IJ} = \frac{1}{4}\mathrm{erfc}\left(\frac{E_I - E_{\mathrm{thresh}}}{\alpha_{\mathrm{Weight}}}\right)\mathrm{erfc}\left(\frac{E_J - E_{\mathrm{thresh}}}{\alpha_{\mathrm{Weight}}}\right) \tag{77}$$

where E_I is the energy of adiabatic state I, E_{thresh} is an energy threshold parameter, and α_{Weight} is a parameter (a recommended value is 0.005 a.u.).

To illustrate the effectiveness of weighted DQΦ diabatization, Boys localized diabatization on 3-state LiH was revisited (from Section 4.5.2). Although the weighted method is not expected to fix the mixing of the covalent S and P states at dissociation, it can fix the unphysical mixing of the ionic I and covalent P state at equilibrium

(Figure 14). Using weighted Boys localized diabatization, as implemented in Reference [104], reasonable potential curves can be obtained near the equilibrium region with sufficient choice of parameters (E_{thresh}=-7.820 a_0 and α_{Weight}=0.005 a_0) as shown in Figure 36.

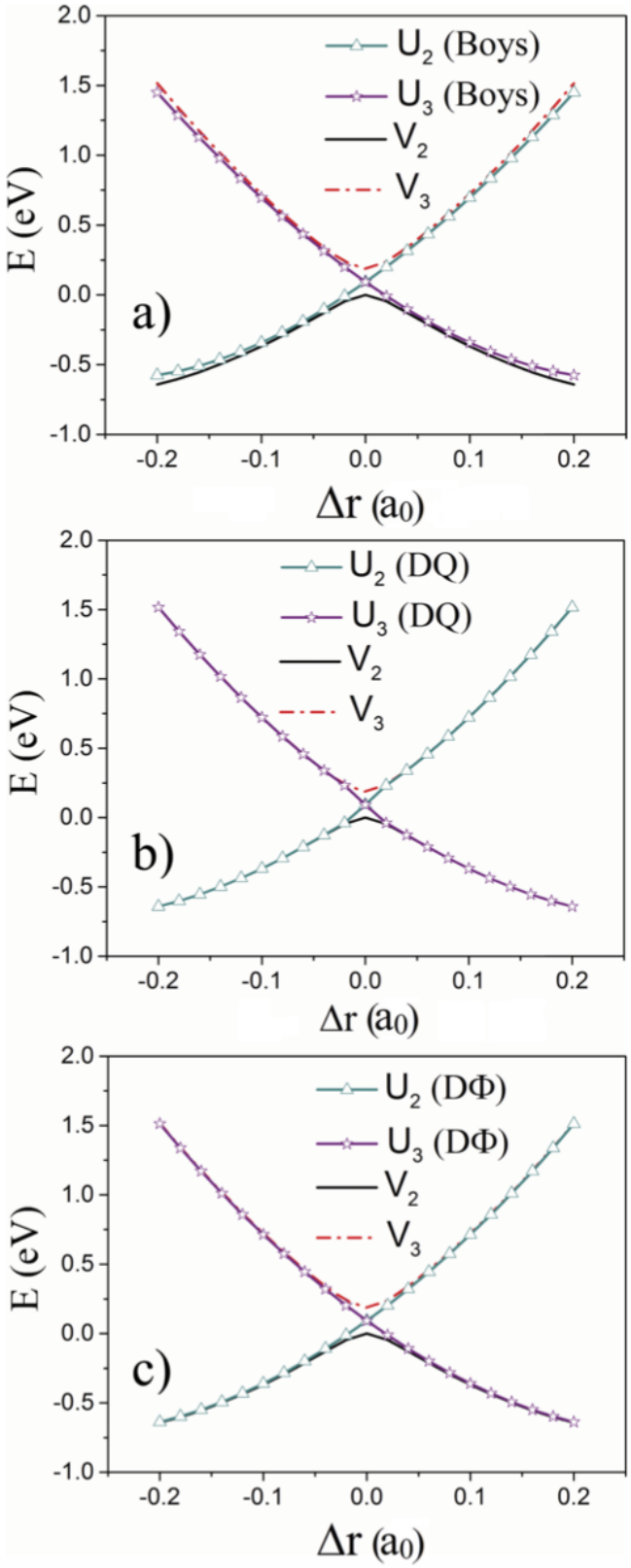

Figure 32: $(H_2)_2$ potential curves with (a) Boys localized diabatization, (b) DQ, and (c) DΦ [95].

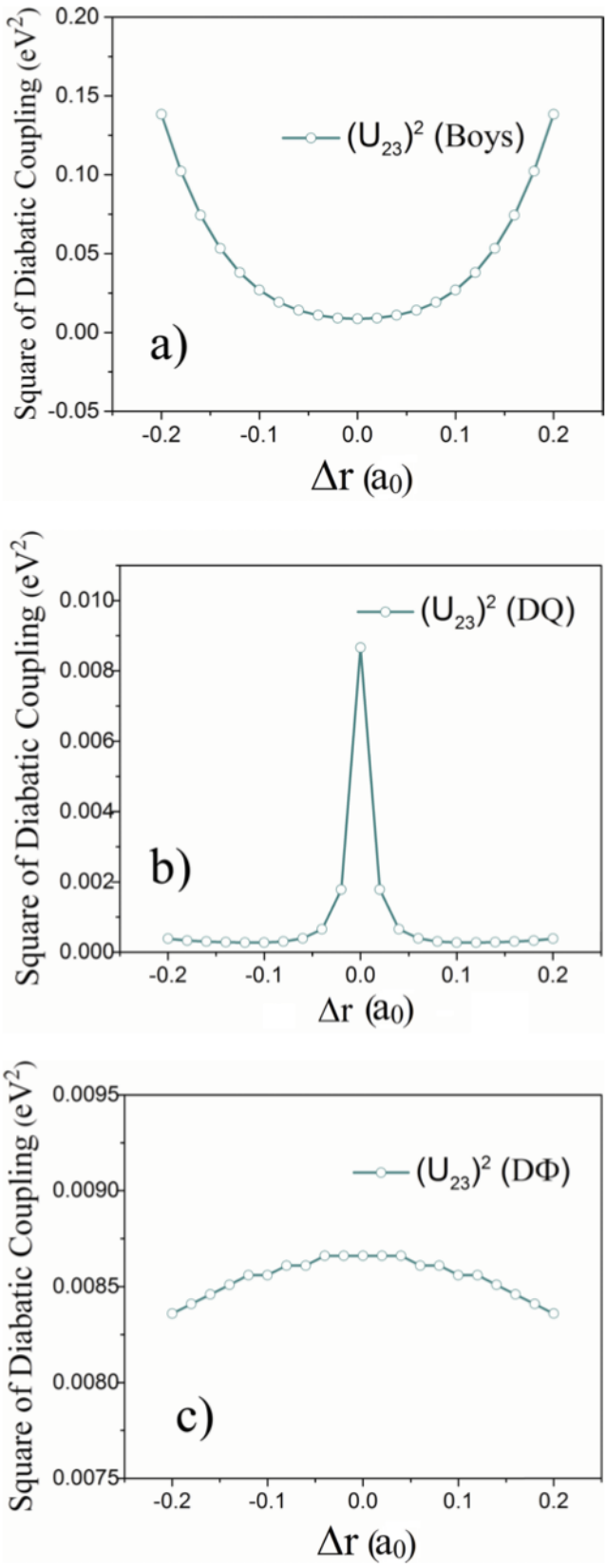

Figure 33: $(H_2)_2$ squared diabatic couplings with (a) Boys localized diabatization, (b) DQ, and (c) DΦ [95].

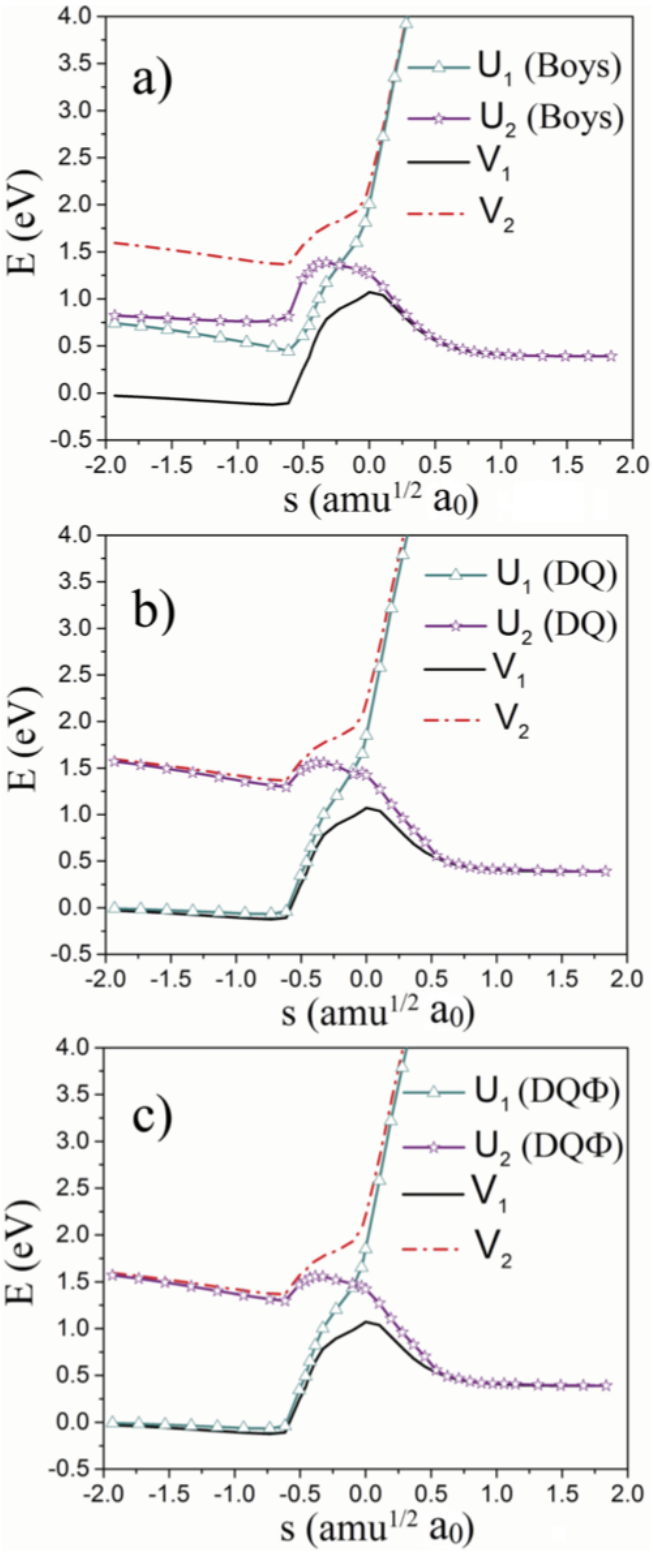

Figure 34: LiFH potential curves with a) Boys localized diabatization, b) DQ diabatization, and c) DQΦ diabatization [95].

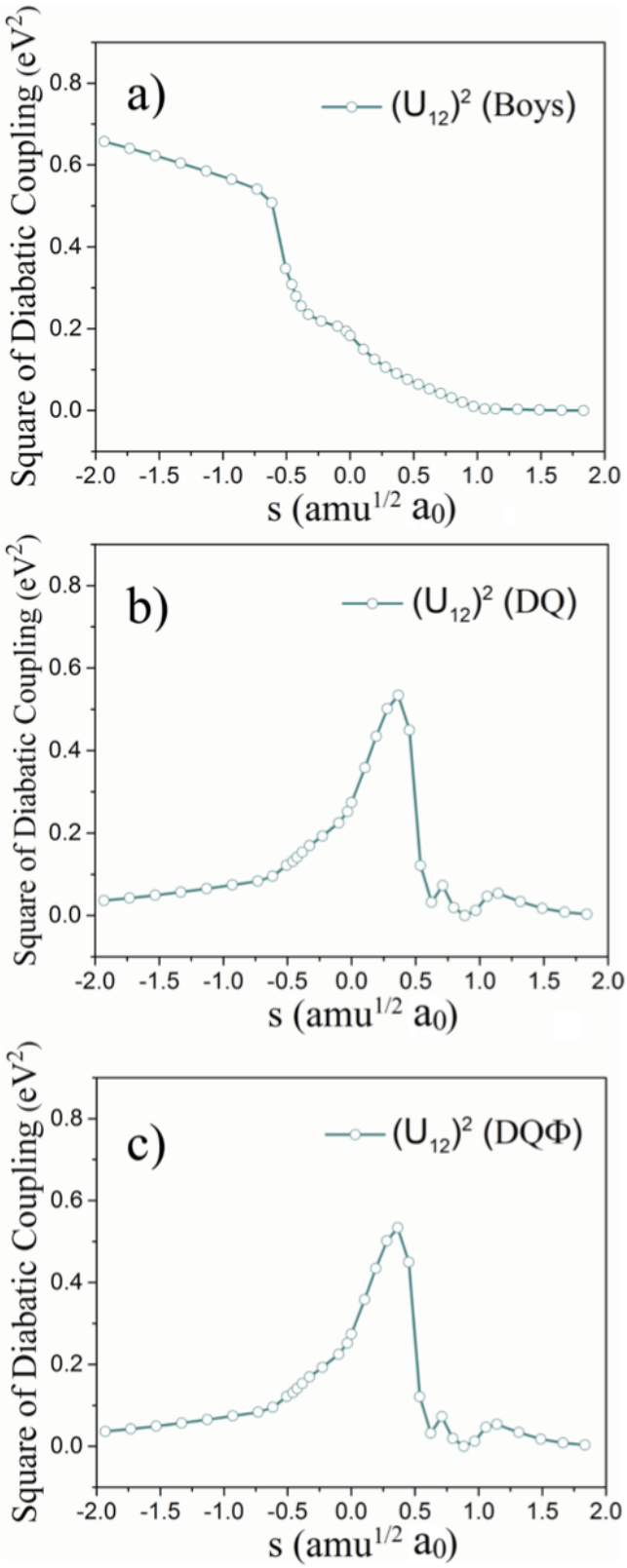

Figure 35: LiFH diabatic couplings with a) Boys localized diabatization, b) DQ diabatization, and c) DQΦ diabatization [95].

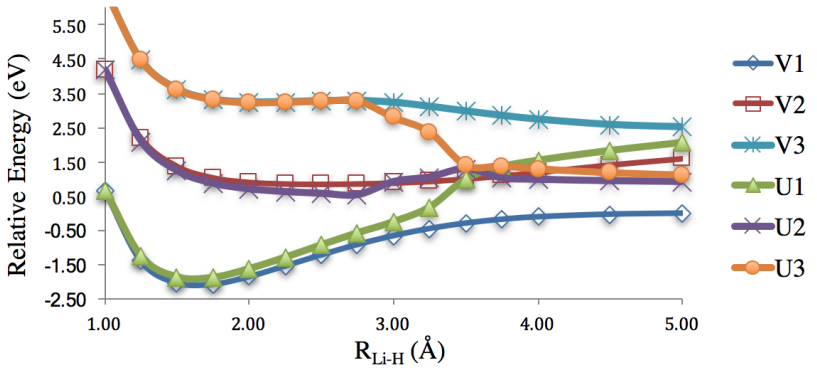

Figure 36: 3-state LiH potential curves with weighted Boys localized diabatization.

6 Conclusions

The benchmarking of multiconfiguration pair-density functional theory (MC-PDFT) on vertical excitations was presented in Section 2. We find that MC-PDFT exhibits quantitative accuracy, indicating its promise for future applications. The post-multiconfigurational-self-consistent-field (post-MCSCF) formalism exhibits serious deficiencies near potential surface crossings. New variational MC-PDFT methods were developed for better treatment of potential surfaces. The average energy formalism (Section 3.2) does not seem promising due to too much state mixing. The average operator formalism appears promising; however, more benchmarking is needed, especially on systems exhibiting conical intersections.

The dipole-quadrupole (DQ) and dipole-quadrupole-electrostatic-potential (DQΦ) diabatization methods were developed as covered in Sections 4 and 5. They appear to be a useful tool for diabatizing general chemical reactions.

References

[1] M. Olivucci, *Computational photochemistry*, vol. 16. Elsevier, 2005.

[2] R. S. Mulliken and W. B. Person, *Molecular complexes: a lecture and reprint volume*. Wiley-Interscience, 1969.

[3] W. Kohn, "Nobel lecture: Electronic structure of matter - wave functions and density functionals," *Rev Mod Phys*, vol. 71, no. 5, pp. 1253–1266, 1999.

[4] G. Li Manni, R. K. Carlson, S. Luo, D. Ma, J. Olsen, D. G. Truhlar, and L. Gagliardi, "Multiconfiguration pair-density functional theory," *J. Chem. Theory Comput.*, vol. 10, no. 9, pp. 3669–3680, 2014.

[5] R. K. Carlson, D. G. Truhlar, and L. Gagliardi, "Multiconfiguration pair-density functional theory: A fully translated gradient approximation and its performance for transition metal dimers and the spectroscopy of $Re_2Cl_8^{2-}$," *J. Chem. Theory Comput.*, vol. 11, no. 9, pp. 4077–4085, 2015.

[6] C. A. Mead, "The "noncrossing" rule for electronic potential energy surfaces: The role of time reversal invariance," *J. Chem. Phys.*, vol. 70, no. 5, pp. 2276–2283, 1979.

[7] H. Eyring and D. Henderson, *Theory of scattering: papers in honor of Henry Eyring*. Academic Press, 1981.

[8] D. J. Griffiths, *Introduction to Quantum Mechanics*. Pearson Prentice Hall, second ed., 2005.

[9] A. Szabo and N. S. Ostlund, *Modern Quantum Chemistry: Introduction to Advanced Electronic Structure Theory*. Dover Publications, Inc., third ed., 1996.

[10] T. Helgaker, P. Jørgensen, and J. Olsen, *Molecular Electronic-Structure Theory*. John Wiley and Sons, Ltd, 2000.

[11] C. J. Cramer, *Essentials of Computational Chemistry*. John Wiley and Sons, Ltd, second ed., 2004.

[12] B. O. Roos, P. R. Taylor, and P. E. M. Siegbahn, "A complete active space SCF method (CASSCF) using a density matrix formulated super-CI approach," *Chem. Phys.*, vol. 48, pp. 157–173, 1980.

[13] J. Olsen, B. O. Roos, P. Jørgensen, and H. J. A. Jensen, "Determinant based configuration interaction algorithms for complete and restricted configuration interaction spaces," *J. Chem. Phys.*, vol. 89, p. 2185, 1988.

[14] H.-J. Werner and W. Meyer, "A quadratically convergent MCSCF method for the simultaneous optimization of several states," *J. Chem. Phys.*, vol. 74, no. 10, pp. 5794–5801, 1981.

[15] K. Andersson, P.-Å. Malmqvist, B. O. Roos, A. J. Sadlej, and K. Wolinski, "Second-order perturbation theory with a CASSCF reference function," *J. Phys. Chem.*, vol. 94, pp. 5483–5488, 1990.

[16] K. Andersson, P.-Å. Malmqvist, and B. O. Roos, "Second-order perturbation theory with a complete active space self consistent field reference function," *J. Chem. Phys.*, vol. 96, p. 1218, 1992.

[17] G. Ghigo, B. O. Roos, and P.-Å. Malmqvist, "A modified definition of the zeroth-order Hamiltonian in multiconfigurational perturbation theory (CASPT2)," *Chem. Phys. Lett.*, vol. 396, no. 1, pp. 142–149, 2004.

[18] P.-Å. Malmqvist, K. Pierloot, A. R. M. Shahi, C. J. Cramer, and L. Gagliardi, "The restricted active space followed by second-order perturbation theory method: theory and application to the study of CuO_2 and Cu_2O_2 systems," *J. Chem. Phys.*, vol. 128, p. 204109, May 2008.

[19] J.-P. Malrieu, J.-L. Heully, and A. Zaitsevskii, "Multiconfigurational second-order perturbative methods: Overview and comparison of basic properties," *Theor. Chim. Acta.*, vol. 90, no. 2-3, pp. 167–187, 1995.

[20] J. Finley, P.-Å. Malmqvist, B. O. Roos, and L. Serrano-Andrés, "The multi-state CASPT2 method," *Chem. Phys. Lett.*, vol. 288, pp. 299 – 306, 1998.

[21] W. Koch and M. C. Holthausen, *A Chemist's Guide to Density Functional Theory*. WILEY-VCH, second ed., 2001.

[22] W. Kohn and L. J. Sham, "Self-consistent equations including exchange and correlation effects," *Phys Rev*, vol. 140, no. 4A, pp. 1133–1138, 1965.

[23] F. Aquilante, L. De Vico, N. Ferré, G. Ghigo, P.-Å. Malmqvist, P. Neogrády, T. B. Pedersen, M. Pitoňák, M. Reiher, B. O. Roos, L. Serrano-Andrés, M. Urban, V. Veryazov, and R. Lindh, "MOLCAS 7: The next generation," *J. Comput. Chem.*, vol. 31, no. 1, pp. 224–247, 2010.

[24] N. Forsberg and P.-Å. Malmqvist, "Multiconfiguration perturbation theory with imaginary level shift," *Chem. Phys. Lett.*, vol. 274, no. 1-3, pp. 196–204, 1997.

[25] M. J. Frisch, G. W. Trucks, H. B. Schlegel, G. E. Scuseria, M. A. Robb, J. R. Cheeseman, G. Scalmani, V. Barone, B. Mennucci, G. A. Petersson, H. Nakatsuji, M. Caricato, X. Li, H. P. Hratchian, A. F. Izmaylov, J. Bloino, G. Zheng, J. L. Sonnenberg, M. Hada, M. Ehara, K. Toyota, R. Fukuda, J. Hasegawa, M. Ishida, T. Nakajima, Y. Honda, O. Kitao, H. Nakai, T. Vreven, J. A. Montgomery, Jr., J. E. Peralta, F. Ogliaro, M. Bearpark, J. J. Heyd, E. Brothers, K. N. Kudin, V. N. Staroverov, R. Kobayashi, J. Normand, K. Raghavachari, A. Rendell, J. C. Burant, S. S. Iyengar, J. Tomasi, M. Cossi, N. Rega, J. M. Millam, M. Klene, J. E. Knox, J. B. Cross, V. Bakken, C. Adamo, J. Jaramillo, R. Gomperts, R. E. Stratmann, O. Yazyev, A. J. Austin, R. Cammi, C. Pomelli, J. W. Ochterski, R. L. Martin, K. Morokuma, V. G. Zakrzewski, G. A. Voth, P. Salvador, J. J. Dannenberg, S. Dapprich, A. D. Daniels, Ö. Farkas, J. B. Foresman, J. V. Ortiz, J. Cioslowski, and D. J. Fox, "Gaussian 09 Revision D.01." Gaussian Inc. Wallingford CT 2009.

[26] H. Koch and P. Jørgensen, "Coupled cluster response functions," *J. Chem. Phys.*, vol. 93, no. 5, pp. 3333–3344, 1990.

[27] J. F. Stanton and R. J. Bartlett, "The equation of motion coupled-cluster method. a systematic biorthogonal approach to molecular excitation energies, transition probabilities, and excited state properties," *J. Chem. Phys.*, vol. 98, no. 9, pp. 7029–7039, 1993.

[28] R. J. Bartlett, "Coupled-cluster theory and its equation-of-motion extensions," *Wiley Interdiscip. Rev.: Comput. Mol. Sci.*, vol. 2, no. 1, pp. 126–138, 2012.

[29] K. Kowalski and P. Piecuch, "New coupled-cluster methods with singles, doubles, and noniterative triples for high accuracy calculations of excited electronic states," *J. Chem. Phys.*, vol. 120, no. 4, pp. 1715–1738, 2004.

[30] P. Piecuch, J. R. Gour, and M. Włoch, "Left-eigenstate completely renormalized equation-of-motion coupled-cluster methods: Review of key concepts, extension to excited states of open-shell systems, and comparison with electron-attached and ionized approaches," *Int. J. Quantum Chem.*, vol. 109, no. 14, pp. 3268–3304, 2009.

[31] M. Gordon and M. Schmidt, "Theory and applications of computational chemistry; Dykstra, CE, Frenking, KS, Scuseria, GE, Eds," 2005.

[32] H. Nakatsuji and K. Hirao, "Cluster expansion of the wavefunction. symmetry-adapted-cluster expansion, its variational determination, and extension of open-shell orbital theory," *J. Chem. Phys.*, vol. 68, no. 5, pp. 2053–2065, 1978.

[33] H. Nakatsuji, "Cluster expansion of the wavefunction. calculation of electron correlations in ground and excited states by SAC and SAC CI theories," *Chemical Physics Letters*, vol. 67, no. 2-3, pp. 334–342, 1979.

[34] S. Ghosh, A. L. Sonnenberger, C. E. Hoyer, D. G. Truhlar, and L. Gagliardi, "Multiconfiguration pair-density functional theory outperforms Kohn–Sham density functional theory and multireference perturbation theory for ground-state and excited-state charge transfer," *J. Chem. Theory Comput.*, vol. 11, no. 8, pp. 3643–3649, 2015.

[35] E. Papajak, J. Zheng, X. Xu, H. R. Leverentz, and D. G. Truhlar, "Perspectives on basis sets beautiful: Seasonal plantings of diffuse basis functions," *Journal of Chemical Theory and Computation*, vol. 7, no. 10, pp. 3027–3034, 2011.

[36] J.-W. Song and K. Hirao, "What makes differences between intra-and intermolecular charge transfer excitations in conjugated long-chained polyene? EOM-CCSD and LC-BOP study," *Theor. Chem. Acc.*, vol. 133, no. 2, pp. 1–9, 2014.

[37] T. Yanai, D. P. Tew, and N. C. Handy, "A new hybrid exchange–correlation functional using the Coulomb-attenuating method (CAM-B3LYP)," *Chem. Phys. Lett.*, vol. 393, no. 1, pp. 51–57, 2004.

[38] R. Li, J. Zheng, and D. G. Truhlar, "Density functional approximations for charge transfer excitations with intermediate spatial overlap," *Phys. Chem. Chem. Phys.*, vol. 12, no. 39, pp. 12697–12701, 2010.

[39] D. Jacquemin, E. A. Perpete, G. E. Scuseria, I. Ciofini, and C. Adamo, "TD-DFT performance for the visible absorption spectra of organic dyes: conventional versus long-range hybrids," *J. Chem. Theory Comput.*, vol. 4, no. 1, pp. 123–135, 2008.

[40] R. A. Kendall, T. H. Dunning Jr, and R. J. Harrison, "Electron affinities of the first-row atoms revisited. systematic basis sets and wave functions," *J. Chem. Phys.*, vol. 96, no. 9, pp. 6796–6806, 1992.

[41] Y. Zhao, N. E. Schultz, and D. G. Truhlar, "Design of density functionals by combining the method of constraint satisfaction with parametrization for thermochemistry, thermochemical kinetics, and noncovalent interactions," *J. Chem. Theory Comput.*, vol. 2, pp. 364–382, 2006.

[42] W. J. Hehre, R. Ditchfield, and J. A. Pople, "Self—consistent molecular orbital methods. XII. further extensions of gaussian—type basis sets for use in molecular orbital studies of organic molecules," *J. Chem. Phys.*, vol. 56, no. 5, pp. 2257–2261, 1972.

[43] J. P. Perdew, K. Burke, and M. Ernzerhof, "Generalized gradient approximation made simple," *Phys. Rev. Lett.*, vol. 77, no. 18, p. 3865, 1996.

[44] C. Adamo and V. Barone, "Toward reliable density functional methods without adjustable parameters: The PBE0 model," *J. Chem. Phys.*, vol. 110, p. 6158, 1999.

[45] `http://physics.nist.gov/PhysRefData/ASD/Levels_form.html`.

[46] F. Weigend and R. Ahlrichs, "Balanced basis sets of split valence, triple zeta valence and quadruple zeta valence quality for H to Rn: Design and assessment of accuracy," *Phys. Chem. Chem. Phys.*, vol. 7, pp. 3297–305, Sep 2005.

[47] T. H. Dunning Jr, "Gaussian basis sets for use in correlated molecular calculations. i. the atoms boron through neon and hydrogen," *J. Chem. Phys.*, vol. 90, no. 2, pp. 1007–1023, 1989.

[48] D. E. Woon and T. H. Dunning Jr, "Gaussian basis sets for use in correlated molecular calculations. iii. the atoms aluminum through argon," *J. Chem. Phys.*, vol. 98, no. 2, pp. 1358–1371, 1993.

[49] D. E. Woon and T. H. Dunning Jr, "Gaussian basis sets for use in correlated molecular calculations. iv. calculation of static electrical response properties," *J. Chem. Phys.*, vol. 100, no. 4, pp. 2975–2988, 1994.

[50] C. E. Hoyer, L. Gagliardi, and D. G. Truhlar, "Multiconfiguration pair-density functional theory spectral calculations are stable to adding diffuse basis functions," *J. Phys. Chem. Lett.*, vol. 6, no. 21, pp. 4184–4188, 2015.

[51] M. Caricato, G. W. Trucks, M. J. Frisch, and K. B. Wiberg, "Electronic transition energies: a study of the performance of a large range of single reference density functional and wave function methods on valence and Rydberg states compared to experiment," *J. Chem. Theory Comput.*, vol. 6, no. 2, pp. 370–383, 2010.

[52] G. D. Purvis III and R. J. Bartlett, "A full coupled-cluster singles and doubles model: the inclusion of disconnected triples," *J. Chem. Phys.*, vol. 76, no. 4, pp. 1910–1918, 1982.

[53] C. E. Hoyer, S. Ghosh, D. G. Truhlar, and L. Gagliardi, "Multiconfiguration pair-density functional theory is as acccurate as CASPT2 for electronic excitation," *J. Phys. Chem. Lett.*, 2016.

[54] A. Dreuw, J. L. Weisman, and M. Head-Gordon, "Long-range charge-transfer excited states in time-dependent density functional theory require non-local exchange," *J. Chem. Phys.*, vol. 119, no. 6, pp. 2943–2946, 2003.

[55] Y. Tawada, T. Tsuneda, S. Yanagisawa, T. Yanai, and K. Hirao, "A long-range-corrected time-dependent density functional theory," *J. Chem. Phys.*, vol. 120, no. 18, pp. 8425–8433, 2004.

[56] Y. Zhao and D. G. Truhlar, "Density functional for spectroscopy: no long-range self-interaction error, good performance for Rydberg and charge-transfer states, and better performance on average than B3LYP for ground states," *J. Phys. Chem. A*, vol. 110, no. 49, pp. 13126–13130, 2006.

[57] S. L. Li and D. G. Truhlar, "Testing time-dependent density functional theory with depopulated molecular orbitals for predicting electronic excitation energies of valence, Rydberg, and charge-transfer states and potential energies near a conical intersection," *J. Chem. Phys.*, vol. 141, p. 104106, Sep 2014.

[58] I. C. Walker and M. H. Palmer, "The electronic states of the azines. IV. pyrazine, studied by VUV absorption, near-threshold electron energy-loss spectroscopy and ab initio multi-reference configuration interaction calculations," *Chem. Phys.*, vol. 153, no. 1-2, pp. 169–187, 1991.

[59] P. Weber and J. R. Reimers, "Ab initio and density functional calculations of the energies of the singlet and triplet valence excited states of pyrazine," *J. Phys. Chem. A*, vol. 103, no. 48, pp. 9821–9829, 1999.

[60] I. C. Walker, M. H. Palmer, and A. Hopkirk, "The electronic states of the azines. II. pyridine, studied by VUV absorption, near-threshold electron energy loss spectroscopy and ab initio multi-reference configuration interaction calculations," *Chem. Phys.*, vol. 141, no. 2, pp. 365–378, 1990.

[61] Z.-L. Cai and J. R. Reimers, "The low-lying excited states of pyridine," *J. Phys. Chem. A*, vol. 104, no. 36, pp. 8389–8408, 2000.

[62] F. F. da Silva, D. Almeida, G. Martins, A. Milosavljević, B. Marinković, S. V. Hoffmann, N. Mason, Y. Nunes, G. Garcia, and P. Limão-Vieira, "The electronic states of pyrimidine studied by VUV photoabsorption and electron energy-loss spectroscopy," *Phys. Chem. Chem. Phys.*, vol. 12, no. 25, pp. 6717–6731, 2010.

[63] D. Feller, K. A. Peterson, and E. R. Davidson, "A systematic approach to vertically excited states of ethylene using configuration interaction and coupled cluster techniques," *J. Chem. Phys.*, vol. 141, p. 104302, Sep 2014.

[64] M. A. Watson and G. K.-L. Chan, "Excited states of butadiene to chemical accuracy: Reconciling theory and experiment," *J. Chem. Theory Comput.*, vol. 8, no. 11, pp. 4013–4018, 2012.

[65] A. Hiraya and K. Shobatake, "Direct absorption spectra of jet-cooled benzene in 130–260 nm," *J. Chem. Phys.*, vol. 94, no. 12, pp. 7700–7706, 1991.

[66] M. Schreiber, M. R. Silva-Junior, S. P. Sauer, and W. Thiel, "Benchmarks for electronically excited states: CASPT2, CC2, CCSD, and CC3," *J. Chem. Phys.*, vol. 128, no. 13, p. 134110, 2008.

[67] R. Huebner, S. Meilczarek, and C. Kuyatt, "Electron energy-loss spectroscopy of naphthalene vapor," *Chem. Phys. Lett.*, vol. 16, no. 3, pp. 464–469, 1972.

[68] W. M. Flicker, O. A. Mosher, and A. Kuppermann, "Electron impact investigation of electronic excitations in furan, thiophene, and pyrrole," *J. Chem. Phys.*, vol. 64, no. 4, pp. 1315–1321, 1976.

[69] D. Leopold, R. Pendley, J. Roebber, R. Hemley, and V. Vaida, "Direct absorption spectroscopy of jet-cooled polyenes. ii. the $1\ ^1b_u^+ \leftarrow 1\ ^1a_g^-$ transitions of butadienes and hexatrienes," *J. Chem. Phys.*, vol. 81, no. 10, pp. 4218–4229, 1984.

[70] R. Mota, R. Parafita, A. Giuliani, M.-J. Hubin-Franskin, J. Lourenco, G. Garcia, S. Hoffmann, N. Mason, P. Ribeiro, M. Raposo, *et al.*, "Water VUV electronic state spectroscopy by synchrotron radiation," *Chem. Phys. Lett.*, vol. 416, no. 1, pp. 152–159, 2005.

[71] A. Chutjian, R. Hall, and S. Trajmar, "Electron-impact excitation of h_2o and d_2o at various scattering angles and impact energies in the energy-loss range 4.2–12 ev," *J. Chem. Phys.*, vol. 63, no. 2, pp. 892–898, 1975.

[72] S. I. Druzhinin, P. Mayer, D. Stalke, R. von Bülow, M. Noltemeyer, and K. A. Zachariasse, "Intramolecular charge transfer with 1-tert-butyl-6-cyano-1,2,3,4-tetrahydroquinoline (ntc6) and other aminobenzonitriles. a comparison of experimental vapor phase spectra and crystal structures with calculations," *J. Am. Chem. Soc.*, vol. 132, no. 22, pp. 7730–7744, 2010.

[73] T. Stein, L. Kronik, and R. Baer, "Reliable prediction of charge transfer excitations in molecular complexes using time-dependent density functional theory," *J. Am. Chem. Soc.*, vol. 131, no. 8, pp. 2818–2820, 2009.

[74] S. H. Vosko, L. Wilk, and M. Nusair, "Accurate spin-dependent electron liquid correlation energies for local spin density calculations: a critical analysis," *Can. J. Phys.*, vol. 58, no. 8, pp. 1200–1211, 1980.

[75] F. Aquilante, J. Autschbach, R. K. Carlson, L. F. Chibotaru, M. G. Delcey, L. De Vico, N. Ferré, L. M. Frutos, L. Gagliardi, M. Garavelli, *et al.*, "Molcas 8: new capabilities for multiconfigurational quantum chemical calculations across the periodic table," *J. Comput. Chem.*, vol. 37, no. 5, pp. 506–541, 2016.

[76] H.-J. Werner and W. Meyer, "MCSCF study of the avoided curve crossing of the two lowest $^1\Sigma^+$ states of LiF," *J. Chem. Phys.*, vol. 74, no. 10, pp. 5802–5807, 1981.

[77] R. J. Cave and M. D. Newton, "Generalization of the Mulliken-Hush treatment for the calculation of electron transfer matrix elements," *Chem. Phys. Lett.*, vol. 249, no. 1, pp. 15–19, 1996.

[78] J. M. Foster and S. F. Boys, "Canonical configurational interaction procedure," *Rev. Mod. Phys.*, vol. 32, no. 2, p. 300, 1960.

[79] C. Edmiston and K. Ruedenberg, "Localized atomic and molecular orbitals," *Rev. Mod. Phys.*, vol. 35, no. 3, p. 457, 1963.

[80] J. E. Subotnik, S. Yeganeh, R. J. Cave, and M. A. Ratner, "Constructing diabatic states from adiabatic states: extending generalized Mulliken-Hush to multiple charge centers with Boys localization," *J. Chem. Phys.*, vol. 129, p. 244101, Dec 2008.

[81] C. E. Hoyer, X. Xu, D. Ma, L. Gagliardi, and D. G. Truhlar, "Diabatization based on the dipole and quadrupole: The DQ method," *J. Chem. Phys.*, vol. 141, p. 114104, Sep 2014.

[82] J. E. Subotnik, J. Vura-Weis, A. J. Sodt, and M. A. Ratner, "Predicting accurate electronic excitation transfer rates via Marcus theory with Boys or Edmiston– Ruedenberg localized diabatization," *J. Phys. Chem. A*, vol. 114, no. 33, pp. 8665–8675, 2010.

[83] E. Alguire and J. E. Subotnik, "Diabatic couplings for charge recombination via Boys localization and spin-flip configuration interaction singles," *J. Chem. Phys.*, vol. 135, p. 044114, Jul 2011.

[84] Q. Ou and J. E. Subotnik, "Electronic relaxation in benzaldehyde evaluated via TD-DFT and localized diabatization: Intersystem crossings, conical intersections, and phosphorescence," *J. Phys. Chem. C*, vol. 117, no. 39, pp. 19839–19849, 2013.

[85] H. Nakamura and D. G. Truhlar, "The direct calculation of diabatic states based on configurational uniformity," *J. Chem. Phys.*, vol. 115, p. 10353, 2001.

[86] H. Nakamura and D. G. Truhlar, "Direct diabatization of electronic states by the fourfold way. ii. dynamical correlation and rearrangement processes," *J. Chem. Phys.*, vol. 117, p. 5576, 2002.

[87] H. Nakamura and D. G. Truhlar, "Extension of the fourfold way for calculation of global diabatic potential energy surfaces of complex, multiarrangement, non-Born–Oppenheimer systems: Application to HNCO (S, S)," *J. Chem. Phys.*, vol. 118, p. 6816, 2003.

[88] K. R. Yang, X. Xu, J. Zheng, and D. G. Truhlar, "Full-dimensional potentials and state couplings and multidimensional tunneling calculations for the photodissociation of phenol," *Chem. Sci.*, vol. 5, no. 12, pp. 4661–4680, 2014.

[89] G. J. Atchity and K. Ruedenberg, "Determination of diabatic states through enforcement of configurational uniformity," *Theor. Chem. Acc.*, vol. 97, no. 1-4, pp. 47–58, 1997.

[90] H. Nakano, "Quasidegenerate perturbation theory with multiconfigurational self-consistent-field reference functions," *J. Chem. Phys.*, vol. 99, no. 10, pp. 7983–7992, 1993.

[91] R. Valero and D. G. Truhlar, "Photochemistry in a dense manifold of electronic states: photodissociation of CH_2ClBr," *J. Chem. Phys.*, vol. 137, p. 22A539, Dec 2012.

[92] X. Xu, K. R. Yang, and D. G. Truhlar, "Diabatic molecular orbitals, potential energies, and potential energy surface couplings by the fourfold way for photodissociation of phenol," *J. Chem. Theory Comput.*, 2013.

[93] P. Å. Malmqvist, "Calculation of transition density matrices by nonunitary orbital transformations," *Int. J. Quantum Chem.*, vol. 30, no. 4, pp. 479–494, 1986.

[94] P.-Å. Malmqvist and B. O. Roos, "The CASSCF state interaction method," *Chem. Phys. Lett.*, vol. 155, no. 2, pp. 189–194, 1989.

[95] C. E. Hoyer, K. Parker, L. Gagliardi, and D. G. Truhlar, "The DQ and DQΦ electronic structure diabatization methods: Validation for general applications," *J. Chem. Phys.*, vol. 144, no. 19, p. 194101, 2016.

[96] L. Pauling, "The nature of the chemical bond—1992," *J. Chem. Educ.*, vol. 69, no. 7, p. 519, 1992.

[97] R. N. Dixon, T. A. Oliver, and M. N. Ashfold, "Tunnelling under a conical intersection: Application to the product vibrational state distributions in the UV photodissociation of phenols," *J. Chem. Phys.*, vol. 134, no. 19, p. 194303, 2011.

[98] T. H. Dunning Jr, "Gaussian basis functions for use in molecular calculations. iii. contraction of (10s6p) atomic basis sets for the first-row atoms," *J. Chem. Phys.*, vol. 55, no. 2, pp. 716–723, 1971.

[99] H.-J. Werner, P. J. Knowles, G. Knizia, F. R. Manby, M. Schütz, P. Celani, T. Korona, R. Lindh, A. Mitrushenkov, G. Rauhut, K. R. Shamasundar, T. B. Adler, R. D. Amos, A. Bernhardsson, A. Berning, D. L. Cooper, M. J. O. Deegan, A. J. Dobbyn, F. Eckert, E. Goll, C. Hampel, A. Hesselmann, G. Hetzer, T. Hrenar, G. Jansen, C. Köppl, Y. Liu, A. W. Lloyd, R. A. Mata, A. J. May, S. J. McNicholas, W. Meyer, M. E. Mura, A. Nicklass, D. P. O'Neill, P. Palmieri, D. Peng, K. Pflüger, R. Pitzer, M. Reiher, T. Shiozaki, H. Stoll, A. J. Stone, R. Tarroni, T. Thorsteinsson, and M. Wang, "Molpro, version 2012.1, a package of ab initio programs," 2012. see.

[100] H.-J. Werner, P. J. Knowles, G. Knizia, F. R. Manby, and M. Schütz, "Molpro a general purpose quantum chemistry program package," *WIREs Comput Mol Sci*, vol. 2, pp. 242–253, 2012.

[101] K. R. Yang, X. Xu, and D. G. Truhlar, "Direct diabatization of electronic states by the fourfold way: Including dynamical correlation by multi-configuration quasidegenerate perturbation theory with complete active space self-consistent-field diabatic molecular orbitals," *Chem. Phys. Lett.*, vol. 573, pp. 84–89, 2013.

[102] R. Krishnan, J. S. Binkley, R. Seeger, and J. A. Pople, "Self-consistent molecular orbital methods. xx. a basis set for correlated wave functions," *The Journal of Chemical Physics*, vol. 72, no. 1, pp. 650–654, 1980.

[103] M. J. Frisch, J. A. Pople, and J. S. Binkley, "Self-consistent molecular orbital methods 25. supplementary functions for gaussian basis sets," *The Journal of chemical physics*, vol. 80, no. 7, pp. 3265–3269, 1984.

[104] C. E. Hoyer, L. Gagliardi, and D. G. Truhlar *DQΦpac, Version 2.0*, available for free at http://comp.chem.umn.edu/dqphipac.

[105] K. Samanta, J. M. Beames, M. I. Lester, and J. E. Subotnik, "Quantum dynamical investigation of the simplest Criegee intermediate CH_2OO and its O-O photodissociation channels," *J. Chem. Phys.*, vol. 141, p. 134303, Oct 2014.

Appendix A: List of Acronyms

- AO = Atomic Orbital
- BO = Born-Oppenheimer
- CASSCF = Complete Active Space Self-Consistent Field
- CASPT2 = Second-Order Complete Active Space Perturbation Theory
- CCSD = Coupled Cluster with Single and Double Excitations
- (F)CI = (Full) Configuration Interaction
- CR = Completely Renormalized
- CSF = Configuration State Function
- DMABN = 4-(dimethylamino)benzonitrile
- DQΦ = Dipole-Quadrupole-Electrostatic-Potential diabatization
- EA = Electron Affinity
- EOM = Equation of Motion
- ES = Excited State
- (t)GGA = (translated) Generalized Gradient Approximation
- GS = Ground State
- HF = Hartree-Fock
- IE = Ionization Energy
- KS-DFT = Kohn-Sham Density Functional Theory

- (t)LSDA = (translated) Local Spin Density Approximation
- MC = Multiconfigurational
- MC-PDFT = Multiconfiguration Pair-Density Functional Theory
- MCSCF = Multiconfigurational Self-Consistent Field
- (D)MO = (Diabatic) Molecular Orbital
- MP2 = Second-Order Møller-Plesset Perturbation Theory
- MR = Multireference
- MRPT = Multireference Perturbation Theory
- MS = Multi-State
- MSE = Mean Signed Error
- MUE = Mean Unsigned Error
- (t)PBE = (translated) Perdew-Burke-Ernzerhof density functional
- PEC = Potential Energy Curve
- PES = Potential Energy Surface
- pNA = *p*-nitroaniline
- RASSCF = Restricted Active Space Self-Consistent Field
- RASPT2 = Second-Order Restricted Active Space Perturbation Theory
- SA = State-Averaged
- SAC = Symmetry Adapted Cluster
- SCF = Self-Consistent Field

- SD = Slater Determinant
- SI = State Interaction
- SR = Single-Reference
- SS = Single State
- TCNE = Tetracyanoethylene
- TD-KS-DFT = Time-Dependent Kohn-Sham Density Functional Theory
- WF(T) = Wave Function (Theory)